Fall 2020

Exploration and Evaluation of Novel Cathode Materials for Intermediate-to-Low Temperature Solid Oxide Fuel Cells

Chunyang Yang

EXPLORATION AND EVALUATION OF NOVEL CATHODE MATERIALS FOR INTERMEDIATE-TO-LOW TEMPERATURE SOLID OXIDE FUEL CELLS

by

Chunyang Yang

Bachelor of Engineering
University of Science and Technology Beijing, 2012

Master of Engineering
University of Science and Technology Beijing, 2015

Submitted in Partial Fulfillment of the Requirements

For the Degree of Doctor of Philosophy in

Mechanical Engineering

College of Engineering and Computing

University of South Carolina

2020

Accepted by:

Xingjian Xue, Major Professor

Jamil A. Khan, Committee Member

Guiren Wang, Committee Member

Guoan Wang, Committee Member

Cheryl L. Addy, Vice Provost and Dean of the Graduate School

ACKNOWLEDGEMENTS

I would like to express my deepest appreciation to my advisor Dr. Xingjian Xue. The completion of my dissertation cannot be done without the extraordinary guidance and unwavering support from Dr. Xue. His invaluable insight into research highly affects me as a researcher. Dr. Xue's tremendous help has prepared me to get to this place in my academic life. It has been a great pleasure to work with Dr. Xue over the past five years.

I am extremely grateful to Dr. Jamil A. Khan, Dr. Guiren Wang and Dr. Guoan Wang for serving as my committee members. I very much appreciate the valuable suggestions and encouragement.

My sincere thanks also go to my group members, Dr. Chunlei Ren, Yun Gan and Myongjin Lee. Whenever I encounter difficulties in my research, they are always there helping me and providing me insightful suggestions.

I would like to express my special thanks to my parents, my sister and my friends. They have provided me endless support and encouragement throughout this entire process. I'm deeply indebted to my boyfriend who gives me unconditional love and makes countless sacrifices to help me.

ABSTRACT

Solid oxide fuel cells (SOFCs) have attracted considerable attentions due to its high conversion efficiency, fuel flexibility, and clean nature. However, the high cost and poor long-term stability induced by the high operating temperature (> 800 ^{o}C) of the conventional SOFCs hinder the further application. Therefore, lowering operating temperature to intermediate temperature range (IT, 650-800 ^{o}C) or even low temperature range (LT, 400-650 ^{o}C) is of practical importance for realizing SOFCs' full commercial potential. Nevertheless, due to the large activation energy associated with oxygen reduction reaction (ORR), cathode polarization resistance becomes the dominate loss limiting SOFCs performance as operating temperature is reduced. This dissertation aims to develop cathode materials with excellent catalytic activity and stability for IT-SOFCs and LT-SOFCs.

The research focuses on altering the physical and chemical properties of cathode materials by various methods. Four cathode materials developed with different strategies are systematically investigated with respect to activity and stability. In Chapter 2, Yb doping in the B-site of $BaCo_{0.7}Fe_{0.3}O_{3-\delta}$ perovskite successfully stabilize the ORR-favored cubic structure. The lower electronegativity of Yb could induce a slightly lower valance of Co and/or Fe, facilitating oxygen vacancy generation and electrochemical kinetic process. $BaCo_{0.7}Fe_{0.2}Yb_{0.1}O_{3-\delta}$ is among the best as a cathode material for IT-SOFCs. In Chapter 3, systematic studies of partial substitution A-site Sr with Yb in $SrCoO_{3-\delta}$ are conducted as cathode for IT-SOFCs. The Yb doping in the A-site brings a

structural evolution and leads to less ordered oxygen vacancies, subsequently highly promotes the catalytic activity of $Sr_{0.90}Yb_{0.10}CoO_{3-\delta}$. Furthermore, $Sr_{0.90}Yb_{0.10}CoO_{3-\delta}$ also exhibits excellent thermal stability as well as CO_2 tolerance. Cathode materials for LT-SOFCs are investigated in Chapter 4 and 5. $Sm_xBa_{1-x}Co_{0.8}Fe_{0.2}O_{3-\delta}$ nanocomposites is prepared through a thermally induced self-assembled process. The intimate contacts between different phases and nanoparticles decorated on the cathode surface bring beneficial effect on the electrochemical performance, which are systematically studied and presented in Chapter 4. In Chapter 5, the introduction of A-site cation deficiency into $Ba_{1-x}Co_{0.6}Fe_{0.2}Zr_{0.1}Y_{0.1}O_{3-\delta}$ has effectively improved its kinetic property and stability as a cathode material for LT-SOFCs. This dissertation contributes to the research and development of high-performance cathode materials and provides valuable insight into methodology of altering electrochemical properties.

TABLE OF CONTENTS

LIST OF TABLES

LIST OF FIGURES

CHAPTER 1

INTRODUCTION

1.1 Introduction to the Background of Fuel Cells

Fuel cells can directly convert the chemical energy in fuels to electrical energy via electrochemical reactions.[1] In the conventional combustion-based heat engines, the chemical energy in fuels needs to convert to thermal energy first, and then to mechanical energy following by the final conversion to the electrical energy. The one step nature (from chemical to electrical energy) in fuel cells offers several unique advantages compared to the multi-step processes involved internal combustion-based energy generation technology. The reducing of the intermediate processes significantly increases the efficiency of fuel cells. Furthermore, the combustion-based energy generation technologies induce severe environmental problems and predominantly contributes to many global concerns, such as climate change, ozone layer depletion, acidic rains, and thus, the consistent reduction in the vegetation cover.[2] However, the emissions of undesirable products from fuel cell technology, such as NO_x, SO_x and other particular pollutants, are virtually zero.[3] Moreover, the combustion-based technologies highly depend on the fossil fuels which are finite in world supplies, while fuel cells use renewable source carriers (i.e., hydrogen). Therefore, fuel cells technology is a cleaner, more efficient and flexible energy conversion method.

Categorized according to electrolyte materials, there are five major types of fuel cells: Phosphoric acid fuel cell (PAFC), Polymer electrolyte membrane fuel cell (PEMFC), Alkaline fuel cell (AFC), Molten carbonate fuel cell (MCFC) and Solid oxide fuel cell (SOFC). Figure 1.1 shows the summary of fuel-cell type.[4] All these cells are operated based on the same underlying electrochemical principles, but differs in operating temperatures, catalyst materials, convert efficiencies, power outputs, fuel sources, etc.. Among all the fuel cells, the fuel sources of SOFCs is more flexible, from hydrogen to hydrocarbons to even carbon.[1] The excellent fuel flexibility nature makes SOFCs one of the most promising candidates for transformative technology. Besides the high efficiency, clean and fuel flexible nature, SOFCs also possess other advantages. All solid state components in SOFCs make it highly reliable, long-lasting and quiet. Due to its very few dynamic parts, the design, fabrication, operation and analysis of SOFCs are simpler than that of liquid or moving part containing system. On the other hand, by changing the number of cells-per-stack and/or stacks-per-system can control the power output of a SOFCs system from 1-W range for small device to megawatt range for power plant.[3]

Figure 1.2 is a schematic diagram showing a H_2-O_2 SOFCs.[5] SOFCs are consist of three major parts: two porous electrodes (cathode and anode) are separated by a gastight electrolyte. At the cathode, O_2 in the oxidant (e.g. air, O_2) is reduced to oxygen ions (O^{2-}) with the aid of electrons. The resulting O^{2-} can transport through the electrolyte lattice, which is an oxygen ion conducting material, to the anode side. At the anode, O^{2-} combines with the gaseous fuel (e.g. H_2, CH_4) in a so-called cold combustion process, yielding heat, H_2O and/or CO_2, and releasing electrons to the external circuit to the

cathode side where reduction of the O_2 proceeds. Therefore, electrical power can be obtained from SOFCs. These electrochemical reactions occur on the cathode and anode side are shown as follow:

$$\text{Cathode: } \frac{1}{2}O_2 + 2e^- = O^{2-} \tag{1-1}$$

$$\text{Anode: } H_2 + O^{2-} = H_2O + 2e^- \tag{1-2}$$

Another important part in SOFCs stacks is the interconnects which can provide both electrical contacts and gas channels, and combine individual cells in series. Figure 1.3 shows the schematic illustration of SOFC stack.The resulting stacks are arranged in series and parallel configurations to provide desired voltage and power outputs from portable power and transportation applications, to large-scale power generation, in both civilian and military sectors.[1] Figure 1.3 shows the schematic illustration of SOFC stack.

1.2 Basic Theoretical Features of SOFCs

The first important parameter of SOFCs is the cell voltage. The driving force for the operation of SOFCs is the different oxygen chemical potentials between the cathode and anode side, which can be described by the Nernst equation. For the H_2-O_2 SOFCs, the Nernst equation can be written as:

$$H_2 + \frac{1}{2}O_2 \leftrightarrow H_2O \tag{1-3}$$

$$E = E^T - \frac{RT}{2F} ln \frac{a_{H_2O}}{a_{H_2} a_{O_2}^{1/2}} \tag{1-4}$$

where E is the reversible cell voltage predicted by thermodynamics, E^T is the standard reversible voltage at temperature T, R is the gas constant, F is the Faraday constant, a_i is the activity of species i. In equation 1-4, E^T is a parameter related to temperature which can be calculated by equation 1-5:

$$E^T = -\frac{\Delta g^0_{rxn}}{nF} \tag{1-5}$$

with Δg^0_{rxn} the free-energy change for the reaction at temperature *T*, *n* the number of moles of electrons transferred. Therefore, for a high temperature H_2-O_2 SOFCs, the reversible cell voltage can be expressed as:

$$E = E^T - \frac{RT}{2F} ln \frac{p_{H_2O}}{p_{H_2} p_{O_2}^{1/2}} \tag{1-6}$$

However, thermodynamically predicted performance cannot represent the SOFCs performance in practical application. The actual cell voltage is smaller than this ideal potential because of several irreversible losses. The output of the SOFCs (V) can be expressed by:

$$V = E_{thermo} - \eta_{act} - \eta_{ohmic} - \eta_{conc} \tag{1-7}$$

where *V* is the operation voltage of SOFCs, E_{thermo} is thermodynamically predicted voltage, η_{act} is the activation losses due to reaction kinetics, η_{ohmic} is ohmic losses from ionic and electronic resistance, η_{conc} is the concentration losses due to mass transport. Due to various losses, the voltage-current relationship in realistic always deviates from the idea case.

1.2.1 Activation losses η_{act}

When the current density is small, the activation loss has an important impact on the cells output. The liberation of free electrons between an electrode and a chemical species distinguishes electrochemical reactions in the cell from simple chemical reaction. However, charge transfer reactions need an activation energy due to the deviation from the reactant states that are energetically stable to product states. Thus, activation polarization can be regarded as extra potential which is needed to overcome the

activation barrier of the electrochemical reactions. The voltage loss due to activation can be described by the Butler-Volmer equation,

$$j = j_0(e^{\alpha nF\eta/(RT)} - e^{-(1-\alpha)nF\eta/(RT)}) \quad (1\text{-}8)$$

where j_0 is the exchange current density for the reaction at equilibrium, α is the transfer coefficient. In reality, the Butler-Volmer equation is fundamentally applicable for most single step electrochemical reactions, and also for the more complex multistep reactions as a first approximation. It can be seen from equation 1-8 that a high j_0 is critical to achieving an excellent performance. When applied to SOFCs, the Tafel equation which is simplified from the Butler-Volmer equation is used more often when discuss the activation polarization. The Tafel equation is approximated when η_{act} is large, which is expressed as:

$$\eta_{act} = -\frac{RT}{\alpha nF}\ln j_0 + \frac{RT}{\alpha nF}\ln j \quad (1\text{-}9)$$

$$\eta_{act} = a + b\log j \quad (1\text{-}10)$$

where *b* is the Tafel slope.

For a basic H_2-O_2 SOFCs, the H_2 related electrochemical reactions occur at the anode side are extremely fast, while the O_2 related oxygen reduction reactions (ORRs) are relatively slow. The activation polarization mostly induces by the cathode side.

1.2.2 Ohmic losses η_{ohmic}

Ohmic polarization are caused by ionic and electronic resistance of the electrolyte and electrodes, as well as the connect resistances. The Ohmic losses along the cell are proportional to the current density:

$$\eta_{ohmic} = jASR_{ohmic} \quad (1\text{-}11)$$

where j is the current density, ASR_{ohmic} is the ohmic resistance of the cell. For SOFCs, the ohmic losses is mainly originated from the electrolyte resistance. Thus, in order to decrease the ohmic losses, developing electrolyte and electrode with high conductivity is of great importance for excellent performance of SOFCs. In another aspect, since resistance scales with thickness, the electrolyte should be made as thin as possible.

1.2.3 Concentration losses η_{conc}

When the current density j is large in SOFCs, the supply and removal of reactant are in great need in the whole system and play an important role on determining the cell performance. Poor mass transport leads to a degradation of cell performance. Diffusion driving by the different gradients in concentration dominates the mass transport in fuel cell electrode, while the convection due to transport of a species by the bulk motion of a fluid dominates in the SOFCs flow structure. The concentration loss can be generated as:

$$\eta_{conc} = c\ ln\frac{j_L}{j_L - j} \tag{1-12}$$

where c is a constant that depends on the geometry and mass transport properties of the SOFCs, j_L is the limiting current density when assuming the reactant concentration falls to zero at interfaces. Thus, careful design of the electrode microstructure and the structure of flow channels can effectively minimize the losses through the mass transport.

By combining all the polarization losses, the performance of SOFCs can be expressed as:

$$V = E_{thermo} - \{(a_A + b_A\ logj) - (a_C + b_C\ logj)\} - jASR_{ohmic} - c\ ln\frac{j_L}{j_L - j} \tag{1-13}$$

By subtracting out the losses from activation, conducting and concentrationfrom the ideal thermodynamically predicted voltage, the real voltage-current relationship of SOFCs can be obtained. This concept is illustrated in Figure 1.4.

1.3 Progress of Mixed Ionic and Electronic Conductor for SOFCs Cathode

One main issue that hinder the development and commercialization of SOFCs application is its high operating temperature. The high operating temperature results in high systems costs, high performance degradation rates, as well as slow start-up and shut-down cycles, which dramatically limiting applicability in portable power and transportation markets.[1] Thus, over the past decade, efforts have been devoted to lower the operating temperature down from high temperature range (over 800 ºC) to intermediate temperature range (IT, 650 to 800 ºC) or even low temperature range (LT, less than or equal to 650 ºC). One of the reasons to reduce operating temperature is to maximum theoretical efficiency.[1] Moreover, lowering operating temperature can further reduce system cost due to wider material choices, such as interconnects, sealing materials, etc.. Rapid start-up, shut-down and improved cell stability also become possible when the operating temperature is reduced.

Cathode polarization loss is a primary issue to consider when reducing operating temperature. Compared with the reactions involved hydrogen at the anode side, the relatively large activation energy associated with oxygen reduction makes the cathode polarization resistance the dominate loss as the operating temperature is reduced.

SOFCs cathode plays the role as catalyst of the oxygen reduction, transportation of the charged species to the electrolyte and distribution of the electrical current associated with ORRs. The oxygen reduction reaction in the cathode side can be separated into several single steps. The elementary steps include:[6] O_2 diffusion from gas phase to the cathode; O_2-adsorption on the cathode and triple phase boundary (TPB)($O_{2(g)} \rightarrow O_{2,ad}$); O-dissociation on the cathode and TPB ($O_{2,ad} \rightarrow 2O_{ad}$); Charge

transfer ($O_{ad} + 2e^- + V_O^{\cdot\cdot} \rightarrow O_o^{\times}$); O-ion diffusion on the electrode surface and in the bulk to the electrolyte. Thus, several criteria need to be considered when exploring new cathode material for SOFCs:[7, 8]

- To minimize the ohmic losses, a good cathode material for SOFCs should exhibit sufficient electronic conductivity;
- High catalytic activity towards oxygen reduction reaction;
- Appropriate thermal expansion coefficient that matches well with the electrolyte materials, typically in the range of 10-12.5×10^{-6} K^{-1}, which can avoid thermo-mechanical stresses;
- Cathode material should possess excellent structural stability in the process of fabrication and operation;
- Good chemical compatibility with other cell components such as the electrolyte and other stack materials;
- Appropriate porous morphology to minimize the losses of the mass transport;
- Cost effective.

Three main families of perovskite-type mixed ionic and electronic conductor (MIEC) has been proposed as potential cathode for IT-SOFCs and even for LT-SOFCs: the simple cubic-type perovskites (ABO_3), the layered perovskites ($AA'B_2O_6$), and the Ruddlesden-Popper phase ($A_{n+1}B_nO3_{n+1}$).

1.3.1 Perovskites ABO_3

A simple perovskite-type oxide possesses the general formula ABO_3, in which the charge of A and B cations are +6. Alkaline earth (Ca, Sr and Ba) and/or lanthanide (Ln = La, Pr, Sm, Nd, etc.) cations are randomly distributed on the A-site, while transition

metals (Fe, Co, Ni, Ti, etc.) are located on B site. Oxygen vacancy is the main ionic charger which is randomly distributed on the O-sublattice.

$La_{1-x}Sr_xMnO_{3-\delta}$ (LSM) is a conventional cathode material for HT-SOFCs because of their excellent structural stability, high electronic conductivity and appropriate thermal expansion coefficient (TEC).[9] However, LSM possesses poor ionic conductivity. When reducing the temperature of cell operation, the polarization loss of LSM increased dramatically due to a narrow TPB region.[10] To overcome this problem, MIEC can be used as new cathode materials. The mixed conductivity can extend the electrochemically active region from the electrode/electrolyte interface to the whole cathode material, which can effectively promote the ORR catalytic activity. Therefore, MIEC with simple perovskite structure have been extensively studied as new cathode materials for IT-SOFCs and LT-SOFCs, such as doped $SrCoO_3$, $LaCoO_3$, $BaCoO_3$ or $LaFeO_3$.

The $La_{1-x}Sr_xCo_{1-y}Fe_yO_{3-\delta}$ (LSCF) family has been widely investigated and applied to the cathode for IT-SOFCs. Because of the similar ionic radii of A-site La and Sr and B-site Co and Fe, a variety of composition with cubic symmetrical are stable, enabling a wide variation in properties. These compounds usually possess high electrical and ionic conductivity, e.g., 100-1000 S cm^{-1} for electrical conductivity and 0.001-0.1 S cm^{-1} for ionic conductivity at 600 ^oC.[11] Moreover, LSCF has an excellent chemical compatibility with ceria-based electrolytes. In the A-site of LSCF material, Sr substitution of La decreases the formation energy of oxygen vacancy, which can highly promotes oxygen diffusion and surface exchange properties, such as $La_{1-x}Sr_xFeO_{3-\delta}$[12, 13], $La_{1-x}Sr_xCoO_{3-\delta}$[14, 15]. Additionally, increasing the content of Sr generally increases the TEC of the material, while increasing Fe content decreases the TEC as well as the

electrical conductivity and tends to increasing the polarization loss.[16, 17] Among all the compositions, $La_{0.6}Sr_{0.4}Co_{0.2}Fe_{0.8}O_{3-\delta}$ is widely used because of its good transport properties with Co in the B-site and moderated TEC values ($13.8\times10\text{-}6\ K^{-1}$), which matches commonly used electrolyte.[18] An area specific resistance (ASR) of 0.82 Ω cm^2 is obtained at 600 °C when electrostatic spray deposition (ESD) was used to deposit $La_{0.6}Sr_{0.4}Co_{0.2}Fe_{0.8}O_{3-\delta}$ cathode film on dense $Ce_{0.9}Gd_{0.1}O_{2-\delta}$ electrolyte.[19] However, the biggest problem of LSCF cathode is the degradation of cathode performance due to Sr segregation.

Compared with LSCF family, $Ba_{1-x}Sr_xCo_{1-y}Fe_yO_{3-\delta}$ (BSCF) family with Ba and Sr in the A-site exhibits faster O-transport kinetics. The size mismatch of A-site and B-site cations leads to the lattice distortion. According to the tolerance factor, the structure of BSCF is near the borderline of cubic phase formation, which could lower the O-migration barrier and also the vacancy formation energy.[20] Therefore, BSCF shows high surface exchange and diffusion rates. The polarization resistance of $Ba_{0.5}Sr_{0.5}Co_{0.8}Fe_{0.2}O_{3-\delta}$ cathode is as low as 0.071 Ω cm^2 at 600 °C. The power density of the anode-supported cell consisting of NiO-SDC anode, SDC electrode and $Ba_{0.5}Sr_{0.5}Co_{0.8}Fe_{0.2}O_{3-\delta}$ cathode reach 1010 mW cm^{-2} at 600 °C.[21] However, BSCF lies at the borderline of the cubic symmetry phase in turn induces a structural problem, leading to a slow decomposition and the formation of a hexagonal perovskite phase.[22, 23]

Mixed ionic electronic conducting perovskite $SrCoO_{3-\delta}$ is a widely studied (electro)catalyst for ORRs but demonstrates different crystal structures at different temperatures. Different crystal structures significantly affects the ordering of oxygen vacancy and electrochemical kinetic properties as well as reliability of related devices.

For example, hexagonal phase turns out to be almost impermeable to oxygen gas. Therefore, it is of great importance to stabilize crystal structure of $SrCoO_{3-\delta}$ in a wide temperature range that favors ORRs. A-site and B-site doping are used to tune the crystal as well as the catalytic kinetic properties of $SrCoO_{3-\delta}$ related materials. A site of the $SrCoO_{3-\delta}$ can be doped with various elements, such as Sm[24], Pr[25], Y[26], etc.. For example, Sm doped $Sm_{1-x}Sr_xCoO_{3-\delta}$ (SSC) has been widely studied because of its high electrical conductivity. The electrical conductivity of $Sm_{0.5}Sr_{0.5}CoO_{3-\delta}$ reaches up to 10^3 S cm^{-1} in the temperature range of 800-1100 ^oC.[24, 27] However, Cobalt containg material always possess high TEC values. The TEC of SSC shows a value greater than 20 $\times 10^{-6}$ K^{-1}, which could produce excessive stresses between the electrode and electrolyte interfaces during thermal cycles. B-site doping, such as Nb[28-30], Sc[30], Ti[31], Sb[32], Mo[33]and Ta[34], are also used to achieving desired electrochemical properties. For example, the polarization resistance of $SrCo_{0.8}Nb_{0.1}Ta_{0.1}O_{3-\delta}$ is 0.11 Ω cm^2 at 650 ^oC. Moreover, A-site deficiency of $SrCo_{0.8}Nb_{0.1}Ta_{0.1}O_{3-\delta}$ enables faster oxygen reduction kinetics as well as better tolerance towards CO_2-containing atmosphere. [35]

1.3.2 Layered double perovskite $AA'B_2O_{6-\delta}$.

Layered double perovskite ($AA'B_2O_{6-\delta}$) also attracts lots of attention as cathode material for SOFCs, where A is low radii lanthanide metal, A' is normally high radii alkaline earth (e.g. Ba), and B is transition metals (e.g. Co). The mostly studied compositions correspond to $LnBaCo_2O_{5+\delta}$. The difference of the ionic radii between Ln^{3+} and Ba^{2+} induces the alternative ordering layers: $AO\text{-}BO_2\text{-}A'O\text{-}BO_2$. The key features that makes them attractive for application as cathode materials are the high electrical conductivity as well as high rates of oxygen surface and diffusion kinetics.[36] However,

different from the randomly distributed oxygen vacancy in simple perovskite, the oxygen vacancy locates on LnO layer. In $LnBaCo_2O_{5+\delta}$, Ln^{3+} trends to decrease its coordination number, resulting in the oxygen vacancy mainly on the LnO layer as well as the two-dimensional transportation.[37] [38-40] The ionic radii difference of A-site and B-site elements highly affects structural features, including cation ordering, degree of structural distortion and oxygen nonstoichiometry in the materials, and thus influences their electrochemical properties. As the Ln^{3+} ionic size decreases from La to Y, the oxygen content decreases from ~5.8 to 5.2, which induces the decrease of the electrical conductivity. On another aspect, the mobility of oxygen vacancy appears to increase with increasing of the ionic from Y to La, since the larger elements increase the nominal oxidation state of cobalt ions and hence the oxygen transport.[41] Thus, $PrBaCo_2O_{5+\delta}$ exhibits great oxygen transport properties and oxygen surface exchange kinetics.[42] Polarization resistance as low as 0.4 Ω cm^2 was achieved at 600 ^oC in air when $PrBaCo_2O_{5+\delta}$ was employed as cathode material for symmetrical cell. A thin film SDC electrolyte fuel cell with $PrBaCo_2O_{5+\delta}$ cathode delivered an attractive peak power densities of 620 mW cm^{-2} at 600 ^oC.[42] Promising results have also achieved with other $LnBaCo_2O_{5+\delta}$, such as $SmBaCo_2O_{5+\delta}$ with a polarization resistance of 0.098 Ω cm^2 at 750 ^oC. And the maximum power densities of a single cell with $SmBaCo_2O_{5+\delta}$ cathode on SDC electrolyte reached 641 mW cm^{-2} at 800 ^oC.[43] Moreover, phase stability is another advantage of layered perovskite over the simple cobalt-barium perovskite without A-site layering, since the Ba-rich hexagonal phase segregation has not been reported for these compounds.

1.3.3 Ruddlesden-Popper phase $A_{n+1}B_nO_{3n+1}$

The general formula of Ruddlesden-Popper (RP) phase material is $A_{n+1}B_nO_{3n+1}$ (A = La, Sr, Pr and B = Cu, Ni, Co), which is consisted of ABO_3 perovskite layers sandwiched between two AO rock-salt layers. RP phase material shows a diverse defect chemistry with a high concentration of oxygen interstitials that offer the rapid oxygen transport kinetic. The most widely studies systems are the n = 1 phases, which possess the K_2NiF_4 structure.[44, 45] Despite promising cathode electrochemical properties, their TEC closely match those of commonly used electrolyte materials (13.7×10^{-6} K^{-1}).

Most of the works have focused on compounds with Ni in the B-site which is considered as an advantage to avoid the special recycling of Co.[46] Some of the compounds, e.g., $La_2NiO_{4+\delta}$ and $Pr_2NiO_{4+\delta}$, are of great interest for the fine-tuning of their electrochemical properties. For $La_2NiO_{4+\delta}$, significant excess oxygen (δ) are incorporated into the rock-salt layer to decrease the structural stresses between the La-O and Ni-O bonding.[47] At the same time, holes are also created due to charge balance in the lattice and thus cause partial oxidation of Ni^{2+} to Ni^{3+} in $LaNiO_3$ layers.[48] Therefore, both the interstitial migration in the rock-salt layer and the vacancy migration in the perovskite layer are responsible for the oxygen migration. However, the interstitial mechanism dominates the oxygen ionic transport.[49] Therefore, the more overstoichiometry and better mobility of oxygen ions are expected to improve the properties of oxygen ionic transport as well as the electrical and electrochemical properties of materials. Doping in La-site with alkaline earths (e.g. Sr, Ca) and other rare earths (Nd and Pr), or doping in the Ni-site with other transition metals (Cu or Co) could lead to dramatic changes of the structural and electrochemical properties. Aliovalent Sr^{2+}

is used to substitute La^{3+} on the A-site to form $La_{2-x}Sr_xNiO_{4+\delta}$, which has higher oxygen diffusivity than that of LSCF at lower temperatures. In addition, $La_{2-x}Sr_xNiO_{4+\delta}$ shows better stability in terms of thermal behavior at high temperatures.[49] B-site doped $LaNi_{1-x}Cu_xO_{4+\delta}$ was also evaluated as cathode material for SOFCs. The TEC of this material is in the range of 10.8-13.0×10^{-6} K^{-1}. For x = 0.4 sample, the electrical conductivity reaches 87 S cm^{-1} at 580 ºC.[50] However, RP nickelates may have phase stability issues. Specifically, Pr_2NiO_4 is metastable below ~1000 ºC, decomposing to $Pr_4Ni_3O_{10}$ and Pr_6O_{11} over time.[51, 52]

1.4 Objectives

SOFCs have the potential to be the fuel cell technology which can reach mass market. Technical challenges of demonstrating commercially meaningful levels of cell, stack and systems durability, still need to be addressed under realistic operating conditions. The cost needs to be reduced to be competitive with other incumbent technologies in the market. Lowering the temperature to intermediate temperature range and even low temperature range is a significant step for the commercialization. Advances in chemistry and processing of materials are allowing the lowering of the operating temperature. However, reducing the operating temperature makes the ORRs at the cathode side more pronounced, resulting in dramatic increase of interfacial polarization resistances. Thus, more fundamental studies are needed to improve the understanding of material properties as cathode material for SOFCs.

In this work, several different methods are employed to tune the properties of the parent material to achieve desired properties. The B-site doping in $BaCoO_{3-\delta}$, A-site doping in $SrCoO_{3-\delta}$, fabrication of nanocomposite material and introduction of A-site

cation deficiency are conducted in this research. The mechanisms underlying the performance are discussed to give an insight into the new cathode material for IT-SOFCs and LT-SOFCs.

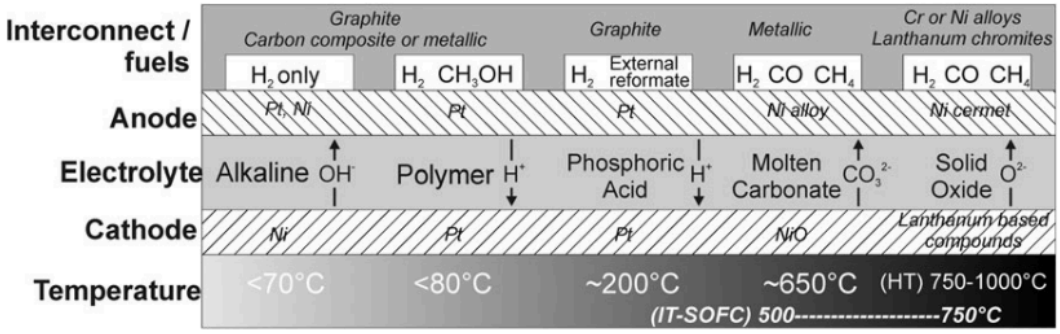

Figure 1.1 Summary of fuel cells type.

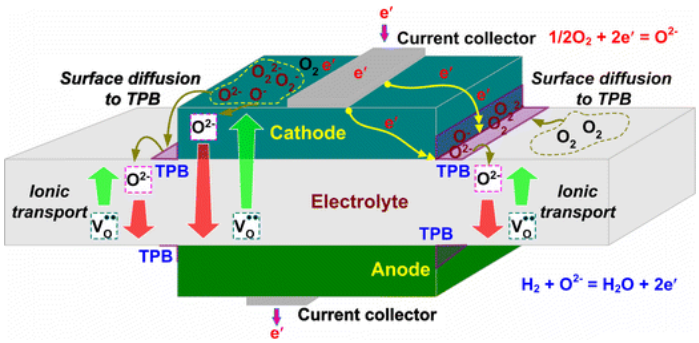

Figure 1.2 Principle of solid oxide fuel cells.

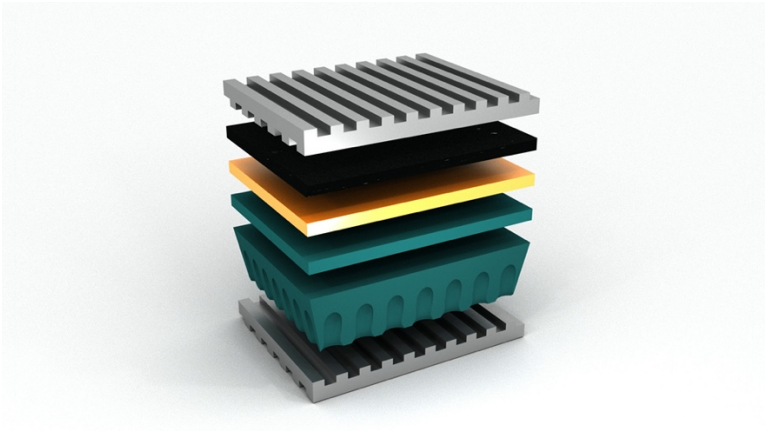

Figure 1.3 Schematic illustration of SOFC stack.

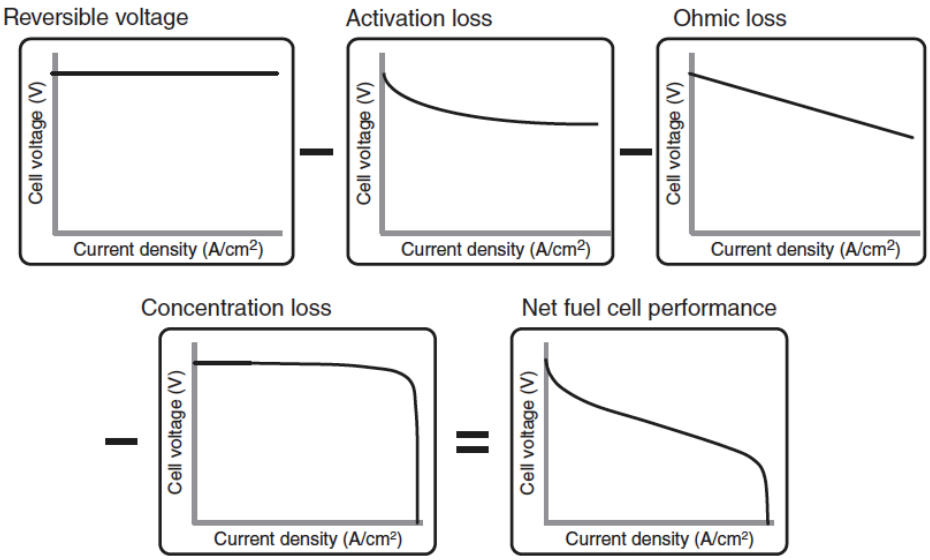

Figure 1.4 Summary of major factors that contribute to the performance of the cell.

CHAPTER 2

Yb DOPING EFFECTS ON STRUCTURE AND PERFORMANCE OF $BaCo_{0.7}Fe_{0.3-x}Yb_xO_{3-\delta}$ PEROVSKITE

2.1 Introduction

In the past few years, a class of $ABO_{3-\delta}$ type mixed conducting materials has been extensively studied as cathode materials for SOFCs. To enhance electrochemical kinetic properties at intermediate temperatures, alkaline-earth metal elements are usually used in A-site while transition metal elements are generally utilized in B-site. In this respect, the $BaCoO_{3-\delta}$ and $SrCoO_{3-\delta}$ have been widely employed as parent compositions for cathode material development of IT-SOFCs.[53-55] While Co-containing perovskites may improve catalytic activity, the easily reducible nature of transition metal ion of Co also results in instability of such parent compositions. Therefore, less easily reducible transition metals of Fe and Nd are employed to partially substitute Co in B-sites so that proper stability-activity tradeoff can be obtained.[53] In this context, cubic perovskite-phase $BaCo_{1-x}Fe_xO_{3-\delta}$ has attracted great interest as cathode materials for IT-SOFCs. Assuming that O-sites are fully occupied in $BaCo_{1-x}Fe_xO_3$, the valence state of Co or Fe would be 4^+ according to the principle of charge neutrality. Oxygen vacancies created in practical crystal structure of $BaCo_{1-x}Fe_xO_{3-\delta}$ would change the valence state of Co or Fe from 4^+ to 3^+ or 2^+.[56] The variable valances and spin states of Co/Fe, to a large degree, are related to the catalytic property, enabling high performance oxygen reduction reaction

of $BaCo_{1-x}Fe_xO_{3-\delta}$ cathode materials. On the other hand, Ba has a large ionic size (r^{XII} = 1.61 Å) and low valance state (2^+) while ionic radii of Co/Fe are relatively small. The combination of large Ba ions with low valance at A-sites and small Co/Fe ions with high valance at B-sites would create sufficient lattice free volume and oxygen vacancies in $BaCo_{1-x}Fe_xO_{3-\delta}$ grains. These will facilitate oxygen ion migration in the perovskite lattice.[57, 58] Unfortunately, the large ionic radius mismatch between Ba and Co/Fe favors the formation of a low symmetric hexagonal phase instead of a simple cubic phase for $BaCo_{1-x}Fe_xO_{3-\delta}$ at low temperatures. With increasing temperatures, phase structural transitions take place from hexagonal to tetragonal and then to cubic. Such phase structural transitions would cause volume change of bulk crystal structure. Study results have shown that the volume variation of bulk $BaCo_{1-x}Fe_xO_{3-\delta}$ may reach up to 10% when the phase structure changes between hexagonal and cubic. If $BaCo_{1-x}Fe_xO_{3-\delta}$ is used as cathode material for SOFCs, such volume variations will directly affect structural reliability of SOFC devices, such as delamination at cathode/electrolyte interface and component fractures. It is also realized that the formation energy of oxygen vacancies in hexagonal phase is much larger than that in the cubic phase.[56] Therefore, it would be very significant if the cubic structure of $BaCo_{1-x}Fe_xO_{3-\delta}$ can be remained from room temperature to IT-SOFC operating temperatures. It is noteworthy that a phase structure at high temperatures usually demonstrates higher symmetry than its low temperature counterpart. Given the fact that the cubic lattices have the highest degree of symmetry among various Bravais lattices, if $BaCo_{1-x}Fe_xO_{3-\delta}$ can be stabilized to a cubic phase at room temperature, it would remain the cubic structure at elevated temperatures.

High valence elements at B-site are able to increase electrostatic repulsion between BO_6 octahedrons in ABO_3. Therefore, the doping of high valence elements at B-site could prevent the connections of BO_6 octahedrons from sharing faces but corners, favoring the formation of cubic perovskite [59]. Based on this understanding, Nb^{5+} [60, 61], Zr^{4+} [62], and Ti^{4+} [63] have been used as the B-site dopants for $BaCo_{1-x}Fe_xO_{3-\delta}$. However, relatively high content of high valence element is required in order to obtain cubic phase. For example, up to 20% amount in the Co/Fe site is required when Ti^{4+} is employed as the B-site dopant.[63] This could significantly deteriorate the catalytic property of $BaCo_{1-x}Fe_xO_{3-\delta}$ at intermediate temperatures. Therefore, it is very important to be able to stabilize the cubic structure of $BaCo_{1-x}Fe_xO_{3-\delta}$ while obtaining high electrochemical kinetic properties. Theoretically, Goldschmidt tolerance factor is able to describe the distortion degree of a perovskite structure from the standard cubic one. To form a cubic perovskite structure, the corresponding Goldschmidt tolerance factor should be close to 1. [64] For the concerned $BaCo_{1-x}Fe_xO_{3-\delta}$, its Goldschmidt tolerance factor is larger than 1. Two doping strategies could be used to tune the Goldschmidt tolerance factor of $BaCo_{1-x}Fe_xO_{3-\delta}$ to 1 and therefore stabilize its cubic structure. One is to dope ions with the size being smaller than Ba at A-site such as Sr^{2+}, La^{2+}. In this context, $Ba_{0.5}Sr_{0.5}Co_{0.8}Fe_{0.2}O_{3-\delta}$ [53] and $La_{0.3}Ba_{0.7}Co_{0.6}Fe_{0.4}O_{3-\delta}$ [65] have been studied. Another strategy is to dope elements with the size being larger than those of Co/Fe into the B-site, such as Y^{3+}.[59, 66]

The effective ionic radius of Yb^{3+} is 0.868 Å in six coordination with oxygen, which is larger than those of Co^{4+} (0.53 Å) and Fe^{4+} (0.585 Å). Therefore, Yb could be used as the B-site dopant to stabilize the cubic structure of $BaCo_{1-x}Fe_xO_{3-\delta}$ down to room

temperature. Meanwhile, Yb has charge states of 3/2, it would also create oxygen vacancies as an acceptor dopant through charge compensation mechanism, enhancing electrochemical kinetics as a cathode material. On the other hand, the electronegativity of Yb, i.e., the power of Yb atom to attract electrons to itself, is 1.1, which is lower than that of Co (1.7) and Fe (1.8). And the elements with lower electronegativity doped in the Co-site of ABO_3 would induce a slightly lower valance of Co/Fe. This would facilitate the formation of oxygen vacancies, enhancing bulk diffusivity and surface exchange process.[34] Meanwhile, lower electronegativity would make it easier for charge carriers to migrate, improving electrical conductivity. Combining above understanding, it seems that suitable Yb doping at B-site of $BaCo_{1-x}Fe_xO_{3-\delta}$ could not only stabilize its cubic structure but also enhance its electrochemical kinetic properties.

In this chapter, a new series material $BaCo_{0.7}Fe_{0.3-x}Yb_xO_{3-\delta}$ (x = 0, 0.05, 0.1 and 0.15; here simply denoted as BCF, BCFYb5, BCFYb10 and BCFYb15, respectively) were systematically studied, including synthesis, crystal structure, sintering ability, and electrical conductivity. The polarization resistance (R_p) of BCFYb electrodes was measured under different oxygen partial pressures at intermediate temperature range of 600-750 ^oC. The Yb doping level that minimized R_p was determined. The rate limiting steps for oxygen reduction reaction were analyzed and identified based on the measured area specific resistances (ASRs). A short-term (~120 h) stability of BCFYb10 lattice structure was examined using a symmetrical cell. The performance of BCFYb10 as cathode material was also evaluated using an NiO-cermet anode-supported microtubular cell.

2.2 Experimental

2.2.1 Material synthesis

All the chemicals utilized in the experiments were purchased from Alfa Aesar and used as-purchased unless otherwise specified. $BaCo_{0.7}Fe_{0.3-x}Yb_xO_{3-\delta}$ (x = 0, 0.05, 0.10 and 0.15) powders were synthesized using citric acid-nitrate combustion method. Specifically, stoichiometric amounts of Yb_2O_3 (99.99%), $Ba(NO_3)_2$ (99.95%), $Co(NO_3)_2 \cdot 6H_2O$ (99+%, Acros Organics) and $Fe(NO_3)_3 \cdot 9H_2O$ (98.0-101.0%) were dissolved in a dilute nitric acid solution under the condition of magnetic stirring to form a transparent solution. Citric acid (99.0-102.0%, BDH) and ethylenediaminetetraacetic acid (EDTA) (99.4-100.6%, BDH) as complexants were added into the transparent solution with the molar ratio of citric acid:EDTA:metal ions = 1.5:1:1. Ammonia was then added until the pH of the solution reached 8. After being mixed homogenously with magnetic stirring, the solution was evaporated at 80 ^oC to form a viscous gel. The gel was then heated on an electrical burner until it combusted to form a bouffant precursor. The precursor was then ground, followed by calcinating at 1000 ^oC in air for 6 h to form powders of BCFYb phase.

The synthesized BCFYb10 powder and $Ce_{0.8}Sm_{0.2}O_{1.9}$ powder (SDC, tape cast grade, Fuel Cell Material, USA) were mixed in a weight ratio of 50:50 and pressed into a pellet at about 250 MPa, followed by sintering at 1150 ^oC in air for 5 h. The as-sintered pellet was then crushed and ground to fine powders for further examination of chemical compatibility.

2.2.2 Bulk sample preparation and electrical conductivity measurement

The synthesized BCFYb powder was mixed with an organic binder of polyvinyl butyral (PVB) in a weight ratio of BCFYb:PVB = 100:2. The mixed powder was uni-axially pressed at about 325 MPa to form a rectangular bar (~35 mm×7 mm×2 mm) and pellet (diameter ~15 mm) using a stainless-steel die and a hydraulic equipment. The green BCFYb5, BCFYb10 and BCFYb15 bars and pellets were then sintered at 1190, 1220 and 1260 ^{o}C in air for 6 h, respectively, to obtain samples with relative density above 95%. The surface of the sintered sample bars was mechanically polished using sand-papers, which were subsequently washed by ethanol in an ultrasonic cleaner. Four silver wires were attached onto the surface of the sample bar at well-aligned four different locations using silver paste (Heraeus 2807). The sample bar with silver wire assembly was sealed in an alumina test chamber. The temperature of the chamber was controlled by a high temperature tube furnace. Air was supplied to the test chamber. The conductivity of the sample bar was automatically recorded using a digital multimeter (Agilent 34401A) in combination with a computer system. The overall electrical conductivity of the sample bar was monitored on-line but not recorded until it reached an equilibrium at a given operating temperature. The overall electrical conductivity of the sample bar was obtained in the temperature range of 150-750 ^{o}C.

Symmetrical cell and single cell preparation

The SDC powders with the binder of PVB (2% wt.) were mixed and ground in ethanol. After drying, the mixed powders were iso-statically cold-pressed at 200 MPa to form an electrolyte substrate with a diameter of ~15 mm. The green electrolyte substrate was then sintered at 1450 ^{o}C in air for 5 h to form a dense SDC electrolyte. The surface

of sintered SDC electrolyte substrate was mechanically polished using sand-papers, which was subsequently washed by anhydrous ethanol in an ultrasonic cleaner. The resulting thickness of SDC electrolyte substrates was about 400 μm. α-terpineol (94% wt.) was mixed with ethyl-cellulose (6% wt.) to form a solution. The synthesized fine electrode material (BCFYb5, BCFYb10, BCFYb15) powders were mixed homogeneously with the α-terpineol solution in a weight ratio of 2:1 to form electrode inks. The electrode ink was then screen-printed onto the either side of dense SDC electrolyte substrate. After drying and aging, symmetrical cells with the configuration of BCFYb5|SDC|BCFYb5, BCFYb10|SDC|BCFYb10 and BCFYb15|SDC|BCFYb15 were then sintered at 1050, 1100 and 1150 ºC in air for 2 h, respectively. Silver wire was attached onto the either side of the symmetrical cells using silver paste (Heraeus 2807) as current collector and external wires for further electrochemical measurements.

An anode-supported microtubular cell NiO-SDC|SDC|BCFYb10 was fabricated to evaluate BCFYb10 performance as a cathode material. The microtubular NiO-SDC electrode substrate was first prepared. Briefly, commercial NiO (Fine grade, Fuel Cell Material, USA) was mixed with SDC powder in a weight ratio of 6:4. The powder mixture was then ball-milled in ethanol for 2 h to form a uniform mixture and subsequently dried at 80 °C overnight. Polyethersulfone (PESf, Veradel 3000P, Solvay Specialty Polymers, USA; 3.5 wt.%) and polyvinylpyrrolidone (PVP, K30, CP, Sinopharm Chemical Reagent Co., China; 0.5 wt.%) were dissolved in N-methyl-2-pyrrolidone (NMP, HPLC grade, Sigma Aldrich, USA; 21.0 wt.%) and ball-milled for 2 h to form an organic mixture. The NiO-SDC powder mixture (75.0 wt.%) prepared above was added into the organic mixture and ball-milled for 48 h to form a homogeneous

extrusion slurry. The as-prepared slurry was de-aired for 10 min and then loaded into an in-house build spinneret extrusion system to obtain green microtubular anode electrode substrate. The extrusion system and related extrusion process were detailed elsewhere.[67] The green anode substrate was first sintered at 600 °C for 2 h in air to remove the organic content, and subsequently sintered at 1100 °C for another 3 h in air to achieve sufficient mechanical strength for subsequent coating of functional layers. The NiO+SDC functional layer was dip-coated onto the pre-sintered anode substrate, and then sintered at 800 ^{o}C in air for 2h. Then the SDC electrolyte layer was dip-coated, followed by sintering at 1450 ^{o}C in air for 6 h to densify the electrolyte layer and form a half-cell. The compositions and preparation process of NiO-SDC and SDC slurries were detailed elsewhere. [67] The BCFYb10 cathode ink prepared above was then brush-painted onto the surface of SDC electrolyte, followed by calcinating at 1100 ^{o}C in air for 2 h to form a single cell NiO-SDC/SDC/BCFYb10. The active cathode area was ~0.25 cm^2. Silver paste was painted onto the cathode as a current collector. Silver wire was wound around the cathode and at either end of the anode substrate to serve as current collector and external circuit.

2.2.3 Characterization and electrochemical measurements

Phase purity of the prepared powder materials was characterized and identified using X-ray diffraction technique (XRD, D/MAX-3C) with Cu Kα radiation (λ = 1.5406 Å) at room temperature with a step size of 0.02^{o} in the range of 10^{o} ≤ 2θ ≤ 90^{o}. Rietveld refinements were performed on the collected XRD patterns of BCFYb5, BCFYb10 and BCFYb15, respectively, using GSAS-II software.[68] Microstructures of the prepared

samples and cells were characterized using a scanning electron microscopy (SEM, Zeiss Ultra Plus FESEM, Germany).

The symmetrical cell prepared above was sealed in an alumina test chamber. The temperature of the chamber was controlled by a high temperature tube furnace. To obtain gas mixture with different oxygen partial pressures, oxygen and nitrogen were supplied to a three-way valve through two different routes, whereby gas mixture was obtained. The gas mixture from the three-way valve was subsequently supplied to the alumina test chamber. The flow rates of oxygen and nitrogen were controlled by flow meters (APEX). The overall flow rate of gas mixture was controlled at 60 ml min^{-1}. By tuning the flow rate of oxygen and nitrogen, oxygen partial pressures of 1, 0.5, 0.21 and 0.05 atm were obtained in the alumina test chamber respectively. The electrochemical impedance spectra (EIS) of the symmetrical cell were obtained in different oxygen partial pressures at intermediate temperatures of 600 to 750 ^{o}C under open circuit voltage conditions. The Zahner IM6E electrochemical workstation was used for EIS measurement with a voltage perturbation of 10 mV over the sweeping frequency range from 0.1 Hz to 10^6 Hz.

The fabricated microtubular single cell NiO-SDC|SDC|BCFYb10 was tested from 600 to 700 ^{o}C with humidified hydrogen as fuel and static air as oxidant. Ceramic paste (Aremco products, inc. USA) was used to seal and attach two alumina tubes to either end of the anode substrate. The temperature of the cell was controlled by a tube furnace (MTI, USA). Nitrogen gas was first supplied to the anode of the cell at room temperature. The cell was then heated up from room temperature to 700 ^{o}C at the rate of 3 ^{o}C per minute. Once the temperature of the cell reached 700 ^{o}C, the gas supplied to the anode was switched from nitrogen to humidified hydrogen (~3% H_2O). The flow rate of

hydrogen was controlled at 30 mL min^{-1} using a precision flowmeter (APEX). The anode reduction under this condition was lasted for 2 h before electrochemical testing. The voltage-current (V-I) curves were measured using a Solartron 1260/1287 electrochemical workstation controlled by CorrWare software.

2.3 Results and Discussion

Figure 2.1a shows the XRD patterns of the synthesized BCF, BCFYb5, BCFYb10 and BCFYb15 powders. The peaks of BCF sample demonstrate a mixture of hexagonal $BaCoO_{2.6}$ phase (PDF#-71-2453) and Fe_3O_4 impurity. The impurity phase Fe_3O_4 generated during synthesis process could be attributed to the large ionic size mismatch between Ba and Co/Fe. The peaks of all Yb-doped samples exhibit a single perovskite phase with cubic symmetry (*Pm-3m* space group, PDF#-75-0227). The peaks are very narrow, indicating that the powder materials were well-crystallized. No other phases could be detected, implying that Yb was totally dissolved into the lattice. Clearly, even very small amount of Yb-doping at B-site effectively stabilized the cubic structure of $BaCo_{0.7}Fe_{0.3}O_{3-\delta}$ to room temperature and the formation of hexagonal phase was prohibited. Since Yb has larger effective ionic radius than Fe, partial substitution of Fe with Yb is expected to increase lattice parameters. Figure 2.1b displays the XRD patterns in the range of 30-32^o, where the highest intensity of the peaks was obtained for the samples. It is obvious to see that the peak was shifted to the lower angles with increasing Yb content, indicating the expansion of lattice volume. To further examine the variation details of lattice parameters at different Yb doping levels, Reitveld refinement was performed on the experimental XRD patterns by using the GSAS-II program, where the cubic structure with Pm-3m space group was used as an initial model. Figure 2.2 shows

an example of the refinement for BCFYb10 sample. A good agreement was observed between the experimental XRD profile and the calculated results. The lattice parameters of BCFYb5, BCFYb10 and BCFYb15 samples obtained from the Reitveld refinement are summarized in Table 2.1. It can be seen that partial substitution of Fe by Yb increased lattice parameter and cell volume, and the more the Yb content was doped the larger the parameters were increased. These results are consistent with the peak shifts of XRD patterns in Figure 2.1b.

Figure 2.3 shows the XRD patterns of as-prepared BCFYb10 powder, the commercial SDC powder and their mixture obtained after solid state reaction treatment. It can be seen that the main peaks of the mixed powders correspond to BCFYb10 phase and SDC phase. Very small peaks at 24^o and 30^o are also observable, which could be assigned to Fe_2O_3 (PDF#85-0987) and Fe_3O_4 (PDF#89-0591), respectively. However, the amount of such secondary phases is very small, suggesting a good chemical compatibility between BCFYb10 and SDC below 1150 ^{o}C.

The sintering ability of the synthesized BCFYb5, BCFYb10 and BCFYb15 were systematically studied. The pellets were first prepared using powders with dry-pressuring technique as mentioned above. The green BCFYb5, BCFYb10 and BCFYb15 pellets were then sintered at the same temperature of 1190 ^{o}C in air for 6 h. Figure 2.4 shows the SEM images of the surfaces and cross-sections of the sintered pellets. As one can see, with increasing Yb content, the pellets became harder to densify and average grain size decreased. Compared with BCFYb10 and BCFYb15 pellets, the BCFYb5 pellet demonstrated very clear grain boundaries. The densities of sintered pellets were further quantitatively determined. In particular, the actual densities of the pellets were measured

using water displacement of Archimedes principle while the theoretical ones were determined by combining the weight formula and the lattice volume obtained from the Rietveld refinement. The relative densities of the pellets were then calculated using the ratio of actual density vs. theoretical one. Results indicate that relative densities of BCFYb5, BCFYb10 and BCFYb15 pellets reached 95.72%, 93.58% and 89.21% respectively, which are consistent with qualitative observations of the sintered sample SEM images. Both qualitative observation and quantitative results seem suggest that Yb dopant inhibited both grain growth and densification of the bulk.

The green pellets were also sintered in air at different temperatures. The minimum temperature that can densify the pellets was identified. Figure 2.5 shows the surface and cross section SEM images of BCFYb5, BCFYb10 and BCFYb15 pellets sintered in air for 6 h at the temperature of 1190, 1220 and 1260 ^{o}C respectively. Clearly, dense pellets were obtained. With increasing Yb content, the sintering temperature to densify the corresponding pellets were slightly increased because Yb dopant is a sintering inhibitor as demonstrated above. The surface images indicate that average grain size of the pellets was also increased with increasing both Yb content and sintering temperature. In this situation, the sintering temperature could outperform the inhibiting effect of Yb dopant. Besides, all the samples exhibited a trans-granular fracture feature, indicating good grain-boundary contact and strong grain-boundary strength. The identified sintering conditions were used to prepare dense sample bars for electrical conductivity measurement.

The electrical conductivity of the sample bars was measured using four terminal dc method in air at temperature range of 150-750 ^{o}C. For a given operating temperature, the electrical conductivity of the sample was monitored but not recorded until it reached

an equilibrium state. Figure 2.6a shows the electrical conductivity of BCFYb5, BCFYb10 and BCFYb15 at different temperatures. It is clear to see that the electrical conductivity of BCFYb10 is higher than those of BCFYb15 and BCFYb5. The electrical conductivity increased with increasing temperatures for the three materials due to the nature of thermally activated charge transport process. It is also noticed that the electrical conductivities of these three materials are in the same order of magnitude as those of $BaCo_{0.7}Fe_{0.22}Nb_{0.08}O_{3-\delta}$ [69], $BaCo_{0.7}Fe_{0.22}Y_{0.08}O_{3-\delta}$ [66] and $BaCo_{0.6}Fe_{0.3}Sn_{0.1}O_{3-\delta}$ [70]. It seems that the variation of the conductivity vs temperature demonstrated two distinct regions. In the temperature range of 150-450 ^{o}C, the conductivity increased exponentially with increasing temperatures. Beyond 450 ^{o}C, the conductivity increased in a little bit low rate relative to the operating temperature. Doped BCF materials typically possess mixed electronic and ionic conductivity due to the co-presence of electron holes and oxygen vacancies [59, 70, 71]. Increasing temperatures will lead to the loss of lattice oxygen, which in turn causes partial annihilation of electronic holes. Such an effect led to an observable change of conductivity around 450 ^{o}C. To clearly show the correlations between conductivity and temperature, Arrhenius plot was obtained and shown in Figure 2.6b. A linear increase of electrical conductivity can be observed in the temperature range of 150-400 ^{o}C for three materials. In the temperature range of 400-750 ^{o}C, electrical conductivity of the three samples still increased linearly but with different slopes from those in the low temperature range. In perovskite oxides, charge carriers are conducted through the route of strongly overlapped B-O-B bond with B representing Co, Fe and/or Yb. The fundamental conducting mechanism is achieved via small polaron hopping through Zerner double exchange process of B^{n+}-O^{2-}-$B^{(n+1)+} \rightarrow B^{(n+1)+}$-$O^{-}$-$B^{(n+1)+} \rightarrow B^{(n+1)+}$-

O^{2-}-B^{n+}. As observed, with increasing Yb doping content from 0.05 to 0.1, the electrical conductivity increased. Since the electronegativity of Yb is smaller than that of Co and Fe, i.e., the ability of Yb to attract electrons is weaker than that of Co and Fe, this makes it easier for electrons to transfer through B-O-B route, leading to the increased electrical conductivity. With further increasing Yb doping level from 0.1 to 0.15, more oxygen vacancies were generated. The presence of oxygen vacancies would block electron transfer in the lattice. In this case, the blocking effect of oxygen vacancies could outperform the low electronegativity of Yb, resulting in the decrease of electrical conductivity. These understanding are consistent with activation energy (Ea) of the materials. Using curve-fitting technique, as shown in Figure 2.6b, it was found that for the Yb doping level of 0.05, the Ea was 0.325 eV in the low temperature range of 150-400 ^{o}C and 0.256 eV in the high temperature range of 400-750 ^{o}C. For the Yb doping level of 0.1 and 0.15, the corresponding Ea was 0.317eV and 0.188 eV as well as 0.330 eV and 0.246 eV respectively. Obviously, the materials demonstrated different electronic transport properties in low and intermediate temperature regions. And BCFYb10 demonstrated the smallest Ea values in both low and intermediate temperature ranges and therefore the highest mobility of charge carrier.

Polarization resistance (R_p) is an important parameter for the evaluation of electrode materials. For ASR measurement, a symmetrical cell needs to be prepared, where identical porous electrode is bonded on either side of a dense electrolyte layer. The sintering temperature is a critical process parameter for electrode fabrication. Low sintering temperature may obtain good surface catalytic property of electrode, but might not be able to well bond the electrode onto the electrolyte. High sintering temperature on

the other hand can produce strong bonding strength at cathode/electrolyte interface, however, it might also severely deactivate surface catalytic property and decrease porosity of electrode. Therefore, suitable sintering temperature is needed to obtain sufficient bonding strength without sacrificing porosity and surface catalytic property of electrode. Here the sintering temperature for symmetrical cell fabrication was systematically studied with the fabrication of BCFYb10|SDC|BCFYb10 as an example. Three sintering temperatures of 1050, 1100 and 1150 ^{o}C were applied to sinter BCFYb10 electrode of the symmetrical cells in air for 2 h. The EIS of the symmetrical cell fabricated at different sintering temperatures was then measured in air under open circuit voltage conditions in the temperature range of 600 - 750 ^{o}C. The results are shown in Figure 2.7a. With increasing the sintering temperature from 1050 to 1100 ^{o}C, ohmic resistance of the cell decreased; further increasing the sintering temperature to 1150 ^{o}C induced a slight increase of ohmic resistance. Meanwhile, the polarization resistance of electrodes sintered at 1100 ^{o}C demonstrated the smallest value. These results imply that the sintering temperature of 1100 ^{o}C could lead to good bonding at electrode/electrolyte interfaces as well as inter-particle bonding in the electrodes while retaining appropriate electrode porosity and surface catalytic property. Figure 2.7b shows the R_p of BCFYb10 electrode sintered at the three different temperatures when measured in the temperature range of 600-750 ^{o}C. As expected, the BCFYb10 electrode sintered at 1100 ^{o}C demonstrated the lowest R_p values at different measuring temperatures. Figure 2.8 shows the cross-sectional SEM images of BCFYb10 symmetrical cells sintered at 1050, 1100, and 1150 ^{o}C in air for 2h respectively. While no delamination could be observed at electrode/electrolyte interfaces, inter-particles in the electrode sintered at 1050 ^{o}C seem

not well bonded. The electrodes sintered at both 1100 and 1150 ^{o}C demonstrated very good inter-particle bonding, the porosity of the former seems higher than that of the latter, further confirming that the sintering temperature of 1100 ^{o}C is a suitable choice. Figure 2.9 shows cross-sectional SEM images of BCFYb5, BCFYb10 and BCFYb15 symmetrical cells sintered in air at 1100 ^{o}C for 2 h. It can be seen that all three electrodes adhered to the SDC electrode well. The inter-particles were also well bonded and porous microstructures were appropriately remained after sintering. However, Yb doping effect on microstructures of electrodes seemed not obvious.

With the fabricated symmetrical cells, EIS was measured in air at intermediate temperatures of 600-750 ^{o}C. Figure 2.10a shows typical EIS profiles of BCFYb5, BCFYb10 and BCFYb15 symmetrical cells measured in air at 650 ^{o}C. To determine appropriate configuration of equivalent circuit for EIS data fitting, the distribution of relaxation times (DRTs) were obtained from EIS data using DRTtools[72, 73] and shown in Figure 2.10b. Two peaks can be observed in DRTs, indicating two distinguishable processes involved in cathodic reactions. The equivalent circuit configuration in Figure 2.10a (the insert figure) is therefore used to fit the measured EIS curves so that polarization resistance as well as pseudo-capacitance associated with each process can be obtained. In the insert figure in Figure 2.10a, L represents an inductance, R_O is total ohmic resistance induced by SDC electrolyte and BCFYb electrodes as well as silver wire, R_i and QPE_i ($i = h, l$) represent resistance and pseudo-capacitance of high (h) and low (l) frequency processes, respectively. It is found that ohmic resistances of three symmetrical cells are very similar. However, due to thickness variations of electrolyte pellets, a slight difference of ohmic resistances also exists. The representative

inductances obtained using both EIS data in Figure 2.10a and equivalent circuit fitting technique are 2.4399×10^{-6}, 2.482×10^{-6}, and 2.0863×10^{-6} H for BCFYb5, BCFYb10 and BCFYb15 electrodes, respectively, which are in the same order of magnitudes. The values of R_h and R_l are corrected by electrode area and divided by two due to the symmetrical configuration of the cell. The polarization resistance (R_p) of the electrode is then obtained by the summation of R_h and R_l. The Arrhenius plots of corresponding polarization resistances are presented in Figure 2.11. The activation energy (E_a) was also obtained from the Arrhenius plots and shown in the same figure. The R_p of three electrodes decreased with increasing operating temperatures, indicating that the cathodic processes are thermally activated. With increasing Yb content from 0.05 to 0.1, the R_p decreased in the entire intermediate temperature range of the measurement. Further increasing Yb content from 0.1 to 0.15 actually increased R_p. The BCFYb10 electrode demonstrated the lowest R_p. This is consistent with the above electrical conductivity results. The E_a value of BCFYb10 was 1.364 eV, which is lower than 1.52 eV of BCFYb5 and 1.401 eV of BCFYb15. The BCFYb10 electrode yielded the ASRs of 0.039, 0.074, 0.161, 0.568 Ω cm^2 at 750, 700, 650 and 600, respectively. As mentioned above, the electronegativity of Yb is lower than that of Co and Fe. When Yb is used as B-site dopant, it would decrease the global electronegativity of BCFYb, which in turn reduces energy barrier for the migration of charge carriers (e.g., electrons) and improves electrical conductivity. On the other hand, doped elements with lower electronegativity at B-site would also slightly reduce the valance of Co and/or Fe, enhancing the formation of oxygen vacancies. While oxygen vacancies improve bulk diffusivity and surface exchange process, they can also block the route of Zerner double exchange process for

electron migrations. Since polarization resistance of electrode reflects synergistic effects of electrical conductivity and bulk diffusivity as well as surface exchange process, this is the reason that polarization resistance and activation energy of BCFYb electrode demonstrates a nonlinear dependence on Yb doping levels and BCFYb10 showed the minimum values. Table 2 shows ASR comparison of BCFYb10 electrode with the state-of-the-art cathodes in open literature. It can be seen that the performance of BCFYb10 electrode is comparable to the best of cathode materials.

The polarization resistance of cathode electrode is induced by the overall processes of electrochemical oxygen reduction reaction (ORR) and strongly dependent on the electrode materials and microstructures as well as operating conditions. For mixed conducting BCFYb10 electrode, these processes may include molecular oxygen adsorption process onto porous electrode surface (i.e., $O_{2,g} \leftrightarrow O_{2,ad}$), dissociation of adsorbed oxygen into atomic oxygen (i.e., $O_{2,ad} \leftrightarrow 2O_{ad}$), and charge transfer reaction (i.e., $O_{ad} + 2e^- + V_O^{\cdot\cdot} \leftrightarrow O_O^{\times}$) for oxygen anion formation and incorporation into oxygen vacancy. From Figure 2.10, it can be seen that EIS curve is consisted of two arcs and the corresponding DRT is composed of two distinguishable peaks, indicating that two processes dominate polarization resistance of electrode (or become rate-limiting). Since oxygen is associated with the overall processes of electrochemical ORR, oxygen partial pressures applied on the electrode would directly affect every single process of electrochemical ORR. Therefore, oxygen partial pressures have intrinsic relationships with polarization resistance contributed by each individual process. Such relationships could be used to link each of EIS arcs or DRT peaks to a specific process, enabling the identification of rate-limiting steps involved in ORRs. Theoretically, the relationship

between polarization resistance induced by each individual process and the applied oxygen partial pressure can be described as, [74]

$$\frac{1}{R_i} \propto P_{O_2}^{m} \tag{2-1}$$

where R_i is the polarization resistance induced by a process involved in ORRs, P_{O_2} is the applied oxygen partial pressure, m is the reaction order. The value of reaction order m is a quantitative indicator, linking to specific individual cathodic process. In particular, the m values of 1, 0.5 and 0.25 correspond to the molecular oxygen adsorption process onto electrode surface, the dissociation of adsorbed oxygen into atomic oxygen, and the charge transfer reaction process, respectively. Obviously, in order to identify rate-limiting steps in ORRs, it is critical to determine the value of reaction order m. For this purpose, the polarization resistance of BCFYb10 electrode was measured using symmetrical cell under different oxygen partial pressures in the temperature range of 600-750 ^{o}C. The polarization resistances associated with high frequency arc (R_h) and low frequency arc (R_l) were obtained using the curve fitting technique as mentioned above. The correlations between the measured R_h and R_l and the applied oxygen partial pressure at different temperatures are shown in Figure 2.12a and b respectively. It can be seen from Figure 2.12a that the values of reaction order m obtained from curve-fitting are close to 0.5 at different temperatures, suggesting that the high frequency arc is primarily contributed by the process of surface molecular oxygen dissociation. The reaction order m values determined from Figure 2.12b are about 0.25 at different temperatures, indicating that the low frequency arc is mainly attributed to the charge transfer process. To further identify specific frequency ranges linked to the individual processes, the corresponding

capacitances and angular relaxation frequencies are calculated using Equations (2) and (3), [75]

$$C_i = \frac{(R_i Q_i)^{(1/n_i)}}{R_i} \quad (2\text{-}2)$$

$$f_i = \frac{(R_i Q_i)^{-(1/n_i)}}{2\pi} \quad (2\text{-}3)$$

where C is capacitance (F cm^{-2}), f is frequency (Hz), pseudo-capacitance Q and polarization resistance R as well as n are obtained through the curve-fitting technique using the measured EIS data and the equivalent electrical circuit of insert figure in Figure 2.10a. The subscript i indicates different arcs in the measured EIS curve. Using EIS data of symmetrical cell measured at different oxygen partial pressures in the temperature range of 600-750 ^oC, the Q_i, R_i, and n_i associated with different arcs were obtained. The frequency and capacitance associated with each arc were determined using Equations (2) and (3). In particular, the frequencies and capacitances associated with high frequency arc are located in the range of 10^3-10^2 Hz and 10^{-2}-10^{-3} F cm^{-2}, respectively. Those associated with low frequency arc are located in the range of 10^0-10^1 Hz and around 10^{-2} F cm^{-2} respectively. Combining with reaction order m analysis performed above, it is clear that surface oxygen dissociation process is primarily confined within the frequency range of 10^3-10^2 Hz while charge transfer process is mainly located in the frequency range of 10^0-10^1 Hz. The capacitances of both oxygen dissociation process and charge transfer process reached the maximum value of 10^{-2} F cm^{-2}. The capacitance is in general closely related and proportional to electrochemically active area of electrode. Since BCFYb10 is a mixed conductor, oxygen vacancies and therefore triple phase boundary sites for electrochemical reactions may extend to the entire surface of porous electrode. The porous BCFYb10 electrode surface is the host sites for both surface oxygen dissociation

and charge transfer. Therefore, the capacitance associated with surface oxygen dissociation process is roughly the same as that associated with charge transfer process for BCFYb10 porous electrodes. The Arrhenius plots of polarization resistance associated with high frequency arc (R_h) and low frequency arc (R_l) were obtained under different oxygen partial pressures and shown in Figure 2.13a and b respectively. The activation energy (E_a) of R_h obtained from Figure 2.13a is in the range of 1.04-1.06 eV at oxygen partial pressures of 0.05-1.0 atm, whereas the E_a of R_l from Figure 2.13b is in the range of 0.089-0.092 eV. Although both surface oxygen dissociation and charge transfer process contributed to the polarization resistance of BCFYb10 electrode, the activation energy analysis seems indicate that oxygen dissociation process is the dominant rate-limiting step in the BCFYb10 cathodic process.

To further evaluate lattice structural stability of BCFYb10 as an electrode material, a short-term durability test (~124 h) was carried out at 700 ºC in air using the corresponding symmetrical cell BCFYb10 | SDC | BCFYb10. The EIS was measured intermittently during the test. The time history of polarization resistance of the electrode was extracted using EIS data at different time. Shown in Figure 2.14a are three EIS curves obtained at the beginning, the middle and the end of the test. It can be seen that ohmic resistance of the cell showed a slight decrease after the short-term durability test, probably because thermal aging of the cell facilitates to further improve various bonding at electrode/electrolyte interfaces and/or among inter-particles in the electrodes, favoring the reduction of ohmic resistance. Figure 2.14b shows the time history of polarization resistance. One can see that the polarization resistance remained a relatively constant value, suggesting that the properties of BCFYb10 electrode are relatively stable. The

result further implies very good stability of BCFYb10 lattice structure during the durability test.

The BCFYb10 as a cathode material was further evaluated using an anode-supported microtubular single cell with the configuration of NiO-SDC | SDC | BCFYb10. Figure 2.15 shows the microstructures of the fabricated microtubular single cell. Radially well-aligned microchannels are embedded in the NiO-SDC anode substrate and open at the inner surface, facilitating facile fuel/gas diffusion. The thickness of dense SDC electrolyte layer is about 20 μm. The porous BCFYb10 cathode and NiO-SDC functional layer are about 25 μm. The humidified hydrogen (~3% H_2O) with the flow rate of 30 ml min^{-1} was supplied to the anode electrode. The BCFYb10 cathode was exposed to the ambient air. As shown in Figure 2.16, the peak power densities of the cell reached 1107, 852 and 480 mW cm^{-2} at 700, 650 and 600 ^oC, respectively, suggesting that BCFYb10 is a promising cathode material for IT-SOFCs. The cross-sectional SEM view of the post-test electrode/electrolyte interfaces are depicted in Figure 2.15d, indicating intimate contacts at the interfaces of electrode/electrolyte and stable microstructures.

2.4 Conclusion

The effects of Yb-doping on crystal structure, sintering-ability, electrical conductivity, and electrochemical performance of $BaCo_{0.7}Fe_{0.3-x}Yb_xO_{3-\delta}$ (x = 0.05, 0.10 and 0.15) have been systematically evaluated. Yb-doping was able to effectively stabilize crystal structure with highly cubic symmetry down to room temperature and improve electrical conductivity. $BaCo_{0.7}Fe_{0.2}Yb_{0.1}O_{3-\delta}$ exhibited the highest electrical conductivity due to the competing effects on the migration of charge carriers between the low electronegativity of Yb and the hindrance of oxygen vacancies. A good chemical

compatibility was obtained between SDC electrolyte and $BaCo_{0.7}Fe_{0.2}Yb_{0.1}O_{3-\delta}$. Yb dopant plays a role of sintering inhibitor, therefore with increasing Yb content, the sintering temperature to densify the corresponding bulk was slightly increased. The $BaCo_{0.7}Fe_{0.2}Yb_{0.1}O_{3-\delta}$ cathode demonstrated the polarization resistances of 0.039, 0.074, 0.161, 0.568 Ω cm^2 at 750, 700, 650 and 600, respectively, the smallest among three Yb doping levels. Surface molecular oxygen dissociation and charge transfer reaction processes were two rate-limiting steps for ORRs associated with $BaCo_{0.7}Fe_{0.2}Yb_{0.1}O_{3-\delta}$ cathode. And the oxygen dissociation process was the dominant rate-limiting step in $BaCo_{0.7}Fe_{0.2}Yb_{0.1}O_{3-\delta}$ cathodic process. The $BaCo_{0.7}Fe_{0.2}Yb_{0.1}O_{3-\delta}$ as a cathode material demonstrated very good stability of lattice structure in a short-term durability test. The peak power densities of the anode-supported microtubular cell NiO-SDC/SDC/$BaCo_{0.7}Fe_{0.2}Yb_{0.1}O_{3-\delta}$ reached 1107, 852 and 480 mW cm^{-2} at 700, 650 and 600 ^oC, respectively, suggesting that $BaCo_{0.7}Fe_{0.2}Yb_{0.1}O_{3-\delta}$ is a promising cathode material for IT-SOFCs.

Table 2.1 Structural parameters obtained from the Rietveld refinement of XRD data for $BaCo_{0.7}Fe_{0.3-x}Yb_xO_{3-\delta}$.

	x=0.05	x=0.10	x=0.15
a (Å)	4.1042(7)	4.1153(5)	4.1367(7)
V(Å^3)	69.136(56)	69.698(00)	70.791(99)
GOF (χ^2)	4.59	4.93	4.92
R_F (%)	3.15	2.57	2.56
R_{wp} (%)	3.59	3.77	3.82

Table 2.2 Polarization resistance comparison of typical IT-SOFC cathode materials in literature and the prepared $BaCo_{0.7}Fe_{0.2}Yb_{0.1}O_{3-\delta}$ in this work.

Composition	Temperature/ ºC	R_p/ Ω cm^2	reference
$La_{0.3}Ba_{0.7}Co_{0.6}Fe_{0.4}O_{3-\delta}$	700	~0.12	[65]
$BaCo_{0.7}Fe_{0.2}Nb_{0.1}O_{3-\delta}$	700	0.12	[71]
$Ba_{0.9}Co_{0.7}Fe_{0.2}Nb_{0.1}O_{3-\delta}$	700	0.07	[76]
$SrCo_{0.9}Nb_{0.1}O_{3-\delta}$	700	0.083	[29]
$Sm_{0.5}Sr_{0.5}CoO_{3-\delta}$	700	2.09	[77]
$La_{0.6}Sr_{0.4}Fe_{0.8}Co_{0.2}O_{3-\delta}$	700	0.14	[78]
	600	0.84	
$La_2NiO_{4+\delta}$	700	0.42	[78]
	600	2.0	
$PrBaCo_2O_{5+\delta}$	700	0.0813	[42]
	600	0.86	
$PrBaCo_{1.6}Fe_{0.4}O_{5+\delta}$	700	0.13	[79]
$SmBaCo_2O_{5+\delta}$	700	0.14	[80]
$BaCo_{0.7}Fe_{0.2}Yb_{0.1}O_{3-\delta}$	700	0.074	This work
	600	0.568	

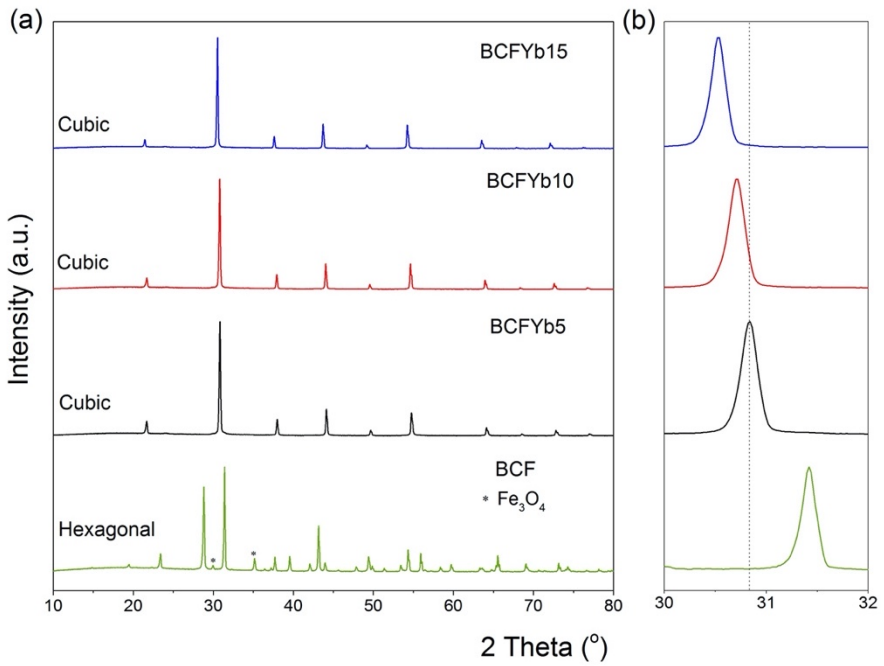

Figure 2.1 XRD patterns of BCF, BCFYb5, BCFYb10 and BCFYb15 calcinated at 1000 °C for 6 h in air (a); details of the selected 2θ range of 30-32° (b).

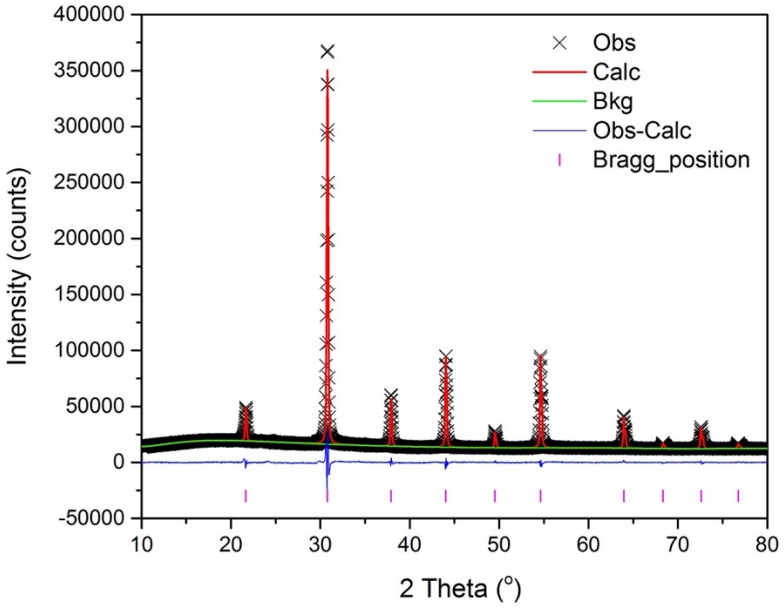

Figure 2.2 XRD pattern and Rietveld refinement result of sample BCFYb10.

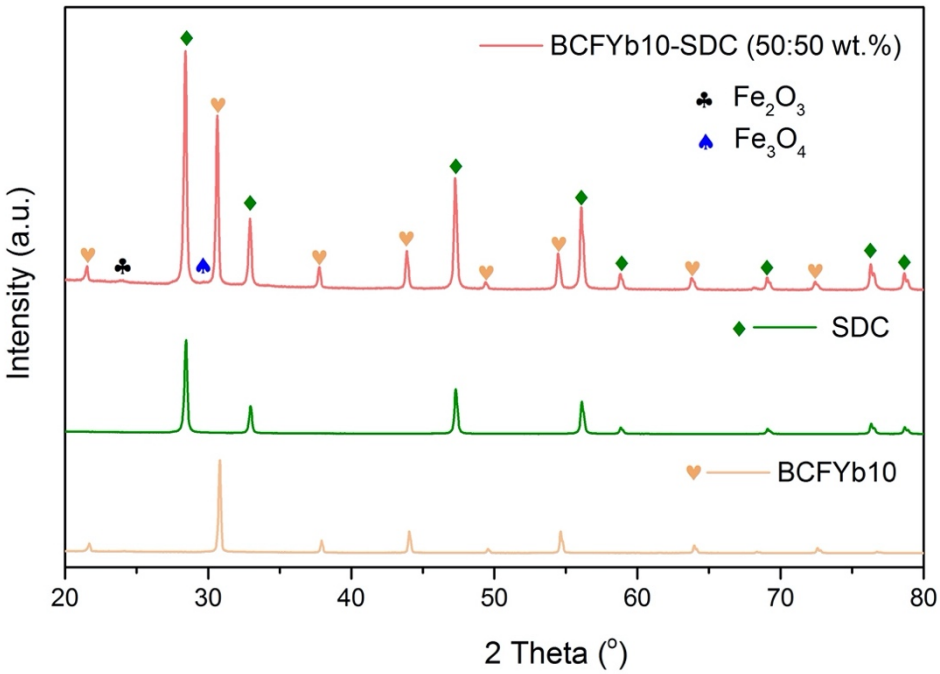

Figure 2.3 XRD patterns of BCFYb10 calcinated at 1000 ºC in air for 6 h, SDC and BCFYb-SDC mixtures after calcination at 1150 ºC in air for 5 h.

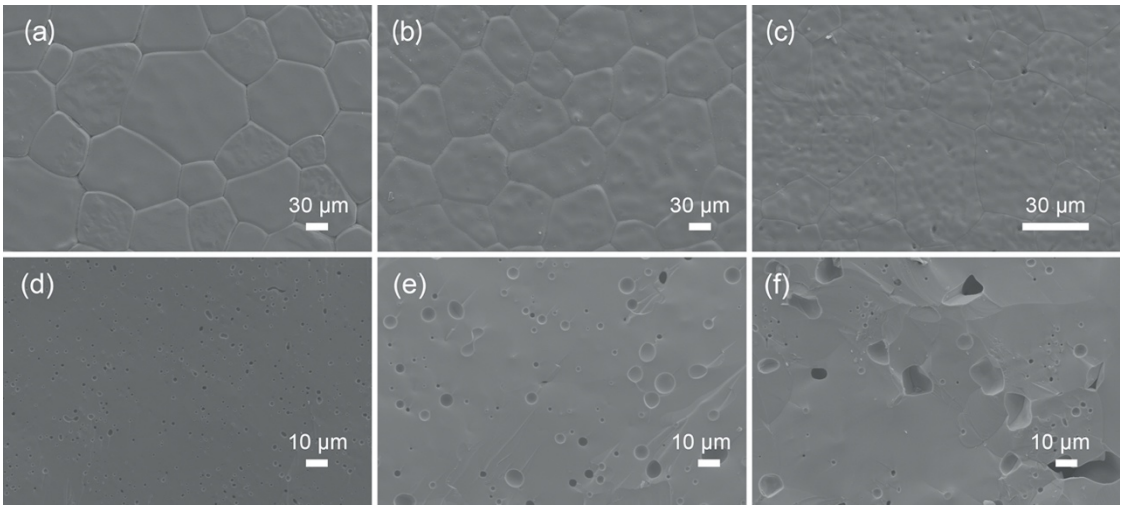

Figure 2.4 Surface (a, b and c) and cross-section (d, e and f) SEM images of bulk BCFYb5 (a, d), BCFYb10 (b, e) and BCFYb15 (c, f) sintered at 1190 ºC in air for 6 h.

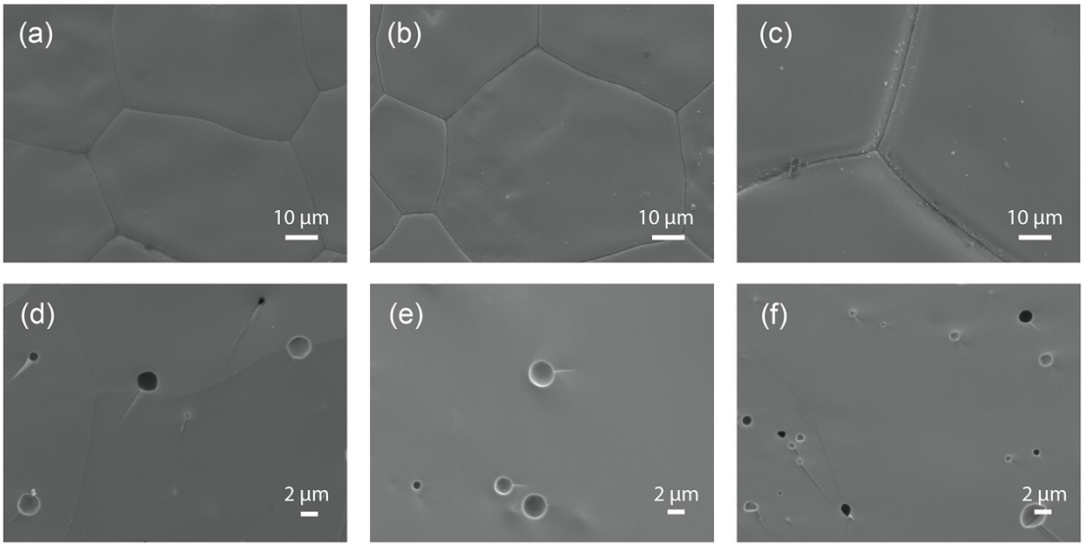

Figure 2.5 Surface (a, b and c) and cross-section (d, e and f) SEM images of bulk BCFYb5 (a, d) sintered at 1190 ºC in air for 6 h, bulk BCFYb10 (b, e) sintered at 1220 ºC in air for 6 h and bulk BCFYb15 (c, f) sintered at 1260 ºC in air for 6 h.

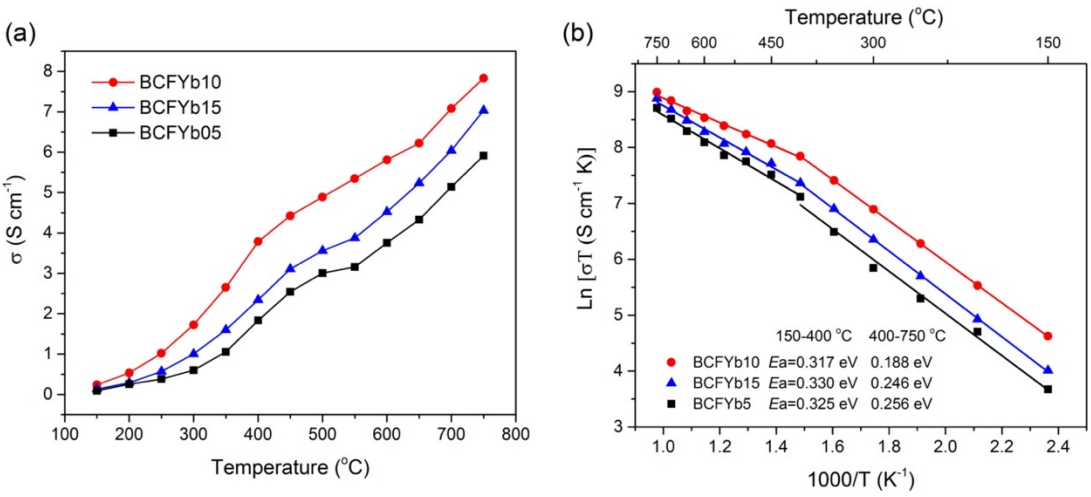

Figure 2.6 Temperature dependence of electrical conductivity of bulk BCFYb5, BCFYb10 and BCFYb15 in air (a) and corresponding Arrhenius plot (b).

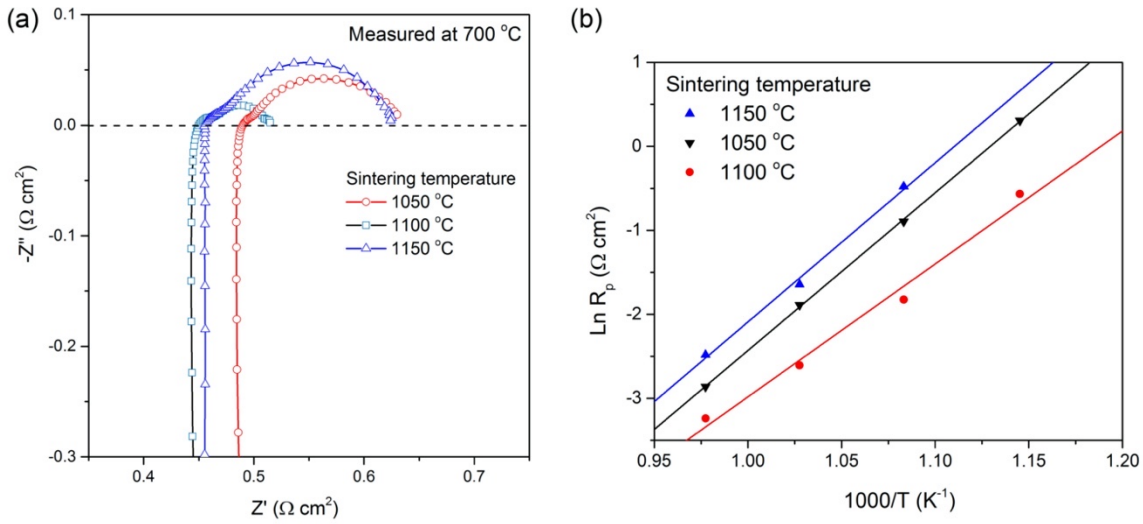

Figure 2.7 EIS of BCFYb10 electrode of symmetrical cells sintered at temperatures of 1050, 1100 and 1150 °C respectively and measured at 700 °C in air (a) and the corresponding Arrhenius plots of polarization resistance measured at 600-750 °C (b).

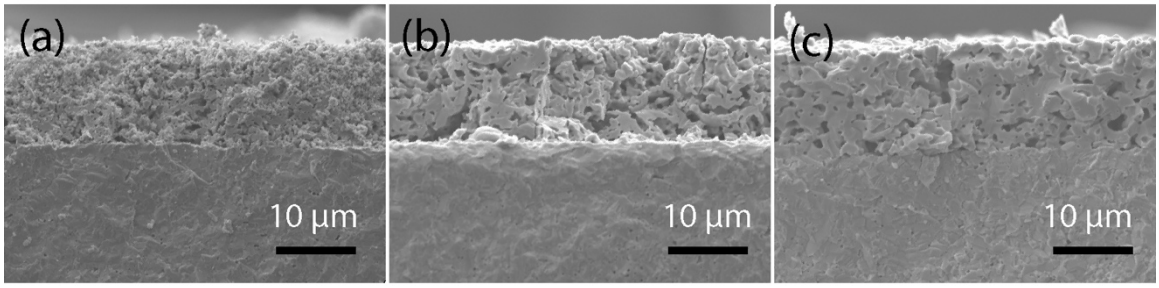

Figure 2.8 Cross-sectional SEM micrographs of symmetrical cells BCFYb10|SDC|BCFYb10 sintered at 1050 ºC (a), 1100 ºC (b) and 1150 ºC (c) in air for 2 h.

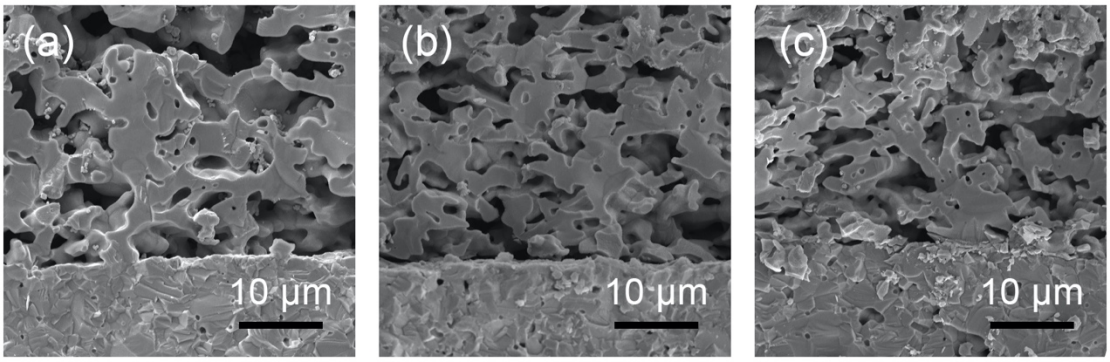

Figure 2.9 Cross-sectional SEM micrographs of symmetrical cells sintered at 1100 °C in air for 2 h: BCFYb5 (a), BCFYb10 (b) and BCFYb15 (c) cathode on SDC electrolyte.

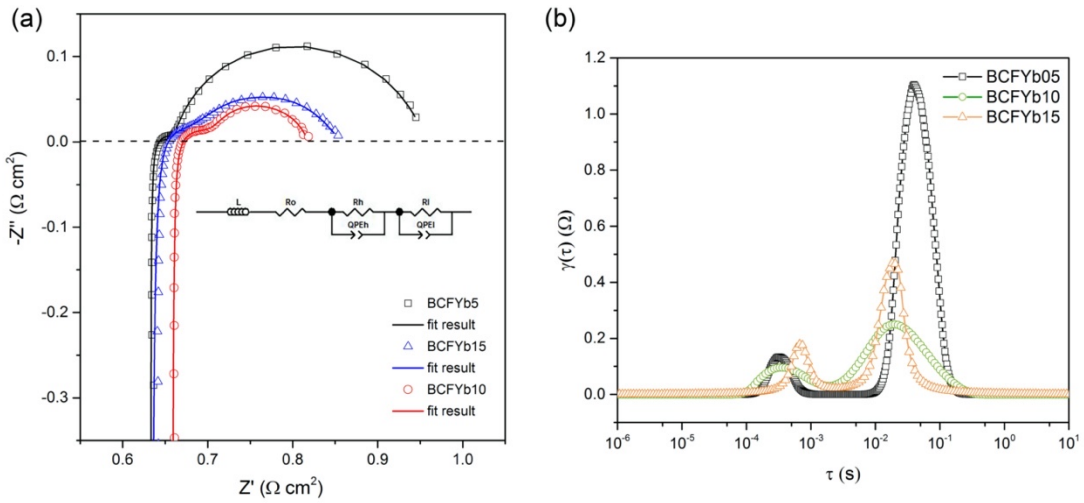

Figure 2.10 Typical electrochemical impedance spectra of BCFYb5, BCFYb10 and BCFYb15 electrode in symmetrical cells at 650 ºC in air and equivalent circuit curve fitting results (a) and the corresponding DRT plots (b).

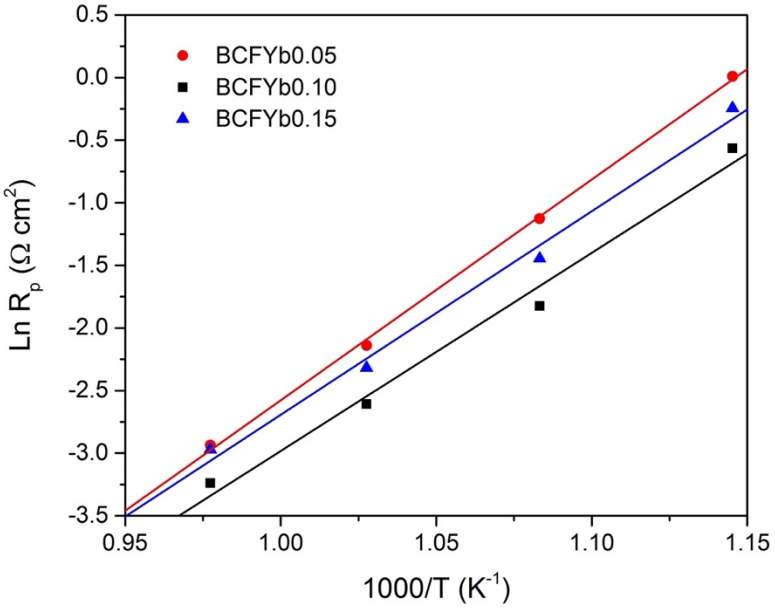

Figure 2.11 Polarization resistance versus temperature reciprocal of BCFYb electrode measured in air.

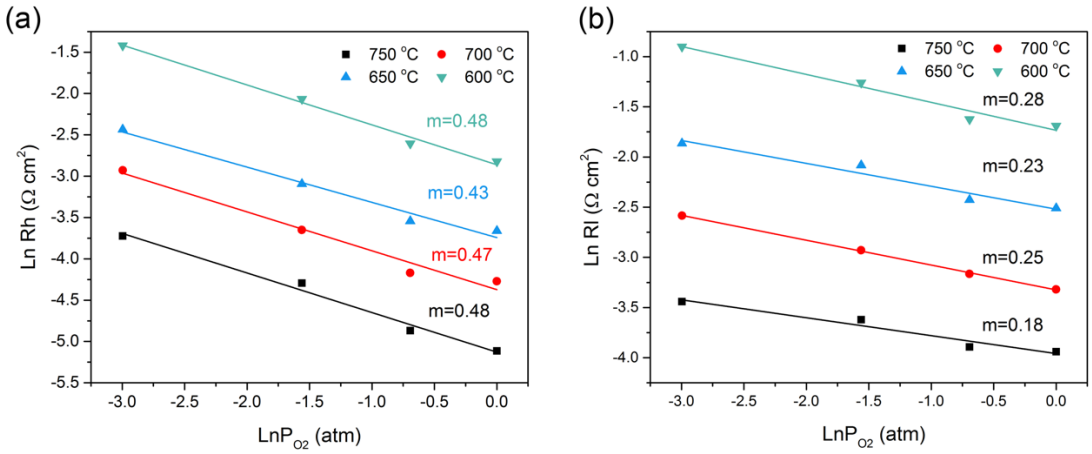

Figure 2.12 Correlations between polarization resistance and applied oxygen partial pressure at different temperatures, and the corresponding reaction orders. (a) polarization resistance associated with high frequency arc, (b) polarization associated with low frequency arc.

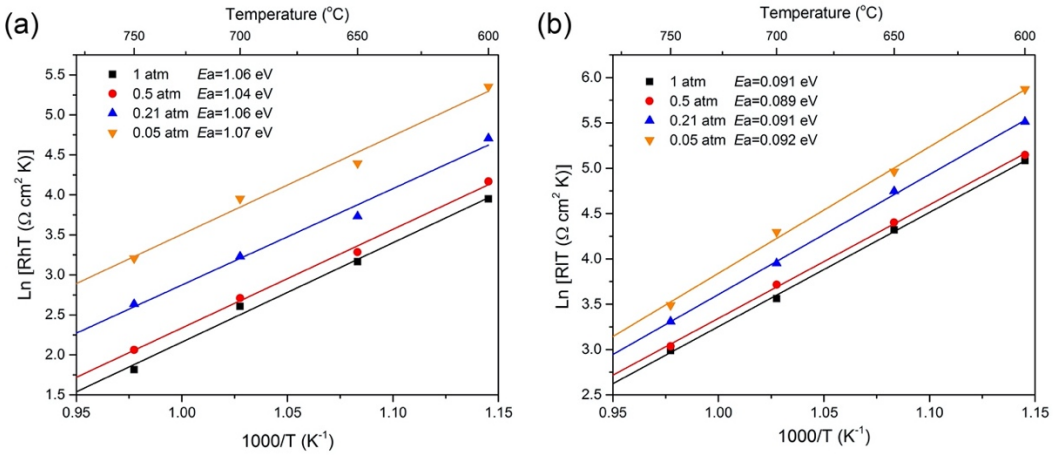

Figure 2.13 Arrhenius plot of BCFYb10 electrode polarization resistance under different oxygen partial pressures and related activation energy. (a) polarization resistance associated with high frequency arc, (b) polarization associated with low frequency arc.

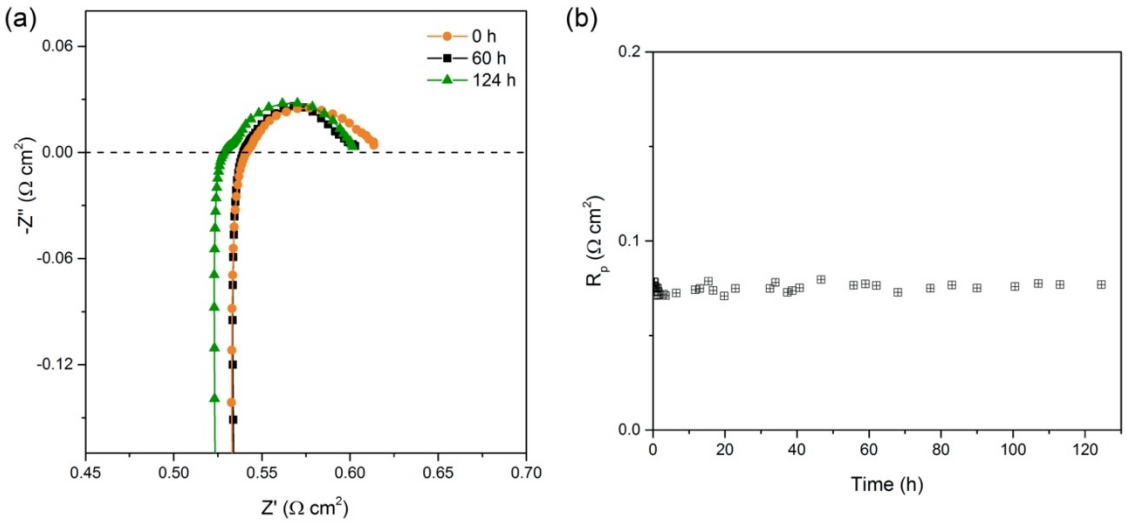

Figure 2.14 Electrochemical impedance spectra of BCFYb10 electrode measured at 700 ºC in air at different time during durability test (a) and time history of polarization resistances of BCFYb10 cathode at 700 ºC in air (b).

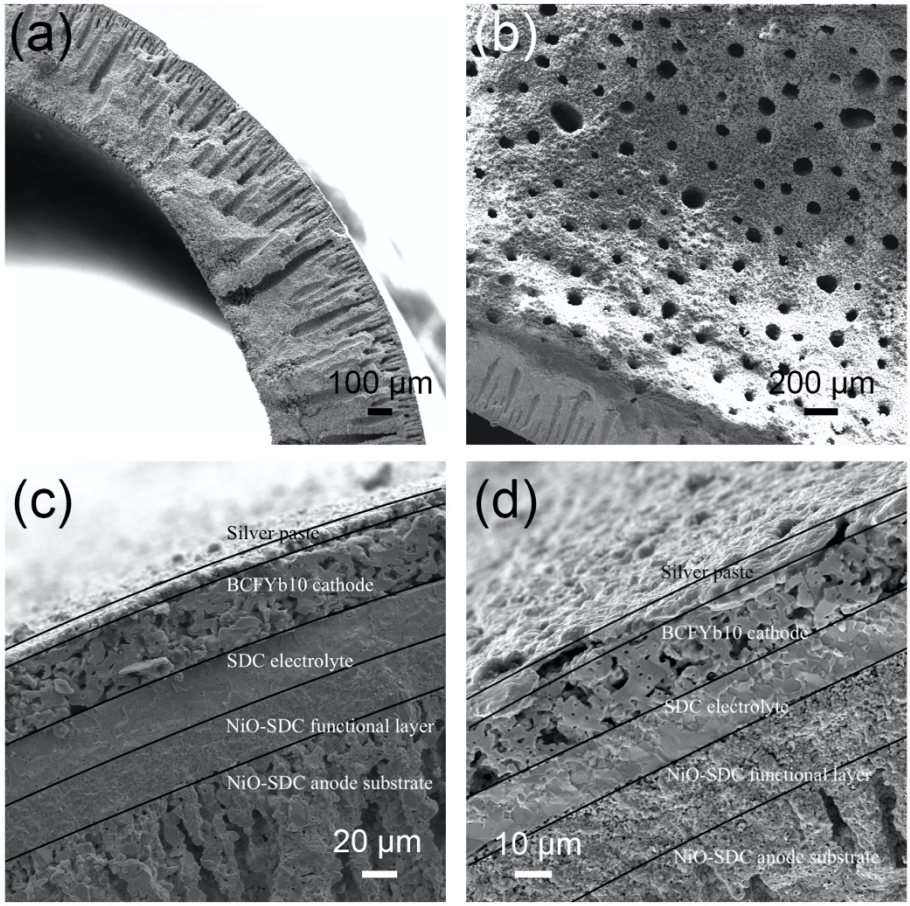

Figure 2.15 SEM images of anode-supported NiO-SDC|SDC|BCFYb10 microtubular cell (a) cross section and (b) inner surface of NiO-SDC substrate after sintered at 1100 ºC in air for 3 h; (c) cross-sectional image of the fabricated signal cell before the test, and (d) after the test.

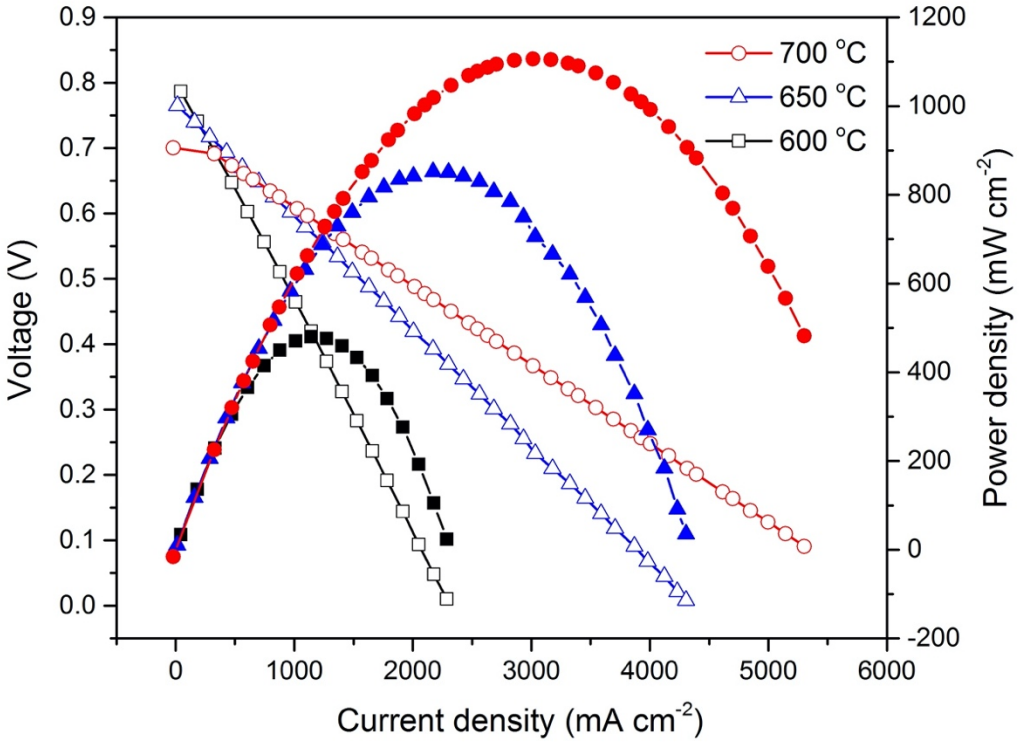

Figure 2.16 Electrochemical performance of anode-supported NiO-SDC|SDC|BCFYb10 microtubular cell measured at intermediate temperatures.

CHAPTER 3

STRUCTURAL EVOLUTIONS, ELECTROCHEMICAL KINETIC PROPERTIES, AND STABILITY OF A-SITE DOPED PEROVSKITE $Sr_{1-x}Yb_xCoO_{3-\delta}$

3.1 Introduction

Solid oxide fuel cells (SOFCs) convert chemical energy in fuels into electrical energy in a highly efficient and environment friendly manner, and have been widely studied.[81] In order to obtain high electrochemical performance, early stage SOFCs are usually operated at high temperatures (above 800 ^{o}C). This operating temperature may increase system and operating cost, limit material selections, and cause material and microstructure degradation.[1] To overcome these issues, it is suggested that the operating temperature of SOFCs be reduced to intermediate range (600-800 ^{o}C).[81, 82] Nevertheless, lowering the operating temperature would increase resistance losses of charge transport and surface exchange kinetic processes, especially polarization losses induced by the cathodic electrode process.[83] Thus, it is very important to develop cathode materials suitable for intermediate temperature SOFCs (IT-SOFCs).

Perovskite-type mixed ionic and electronic conducting (MIEC) materials have high flexibility to tune their physical properties such as oxygen vacancies, structural symmetry, lattice free volumes, metal-oxygen bonding energies. These properties are strongly dependent on crystal structure and significantly affect electrochemical kinetic

properties and stability of the materials.[57, 84] Strontium cobaltite ($SrCoO_{3-\delta}$) is a typical perovskite MIEC showing high electrical conductivity and electrocatalytic property as a cathode material for SOFCs and has been widely used as a parent compound to derive other high performance MIEC cathodes.[85] Depending on annealing temperature and oxygen partial pressure during synthesis/fabrication process, $SrCoO_{3-\delta}$ may adopt a variety of crystal structures, e.g., orthorhombic, tetragonal and cubic. For example, $SrCoO_{3-\delta}$ forms an oxygen vacancy-ordered orthorhombic brownmillerite phase below 653 ^{o}C, and will transfer to a 2-H type hexagonal phase between 653 and 920 ^{o}C, eventually changes to a cubic or tetragonal perovskite phase above 920 ^{o}C. However, the high temperature phase will transit reversibly to a hexagonal phase as temperature drops from a high (> 920 ^{o}C) to intermediate temperature range.[86] These phase variations directly affect oxygen vacancy features and the electrochemical properties of $SrCoO_{3-\delta}$. For example, the vacancy ordered state at low temperatures transforms to a disordered state above 900 ^{o}C; the resulting hexagonal phase is almost impermeable to oxygen gas.[87] Interestingly, the high temperature phase of $SrCoO_{3-\delta}$, a cubic phase, demonstrates the best electrochemical kinetic properties among all the phases.[85] [88] Therefore, it is important to stabilize the cubic phase of $SrCoO_{3-\delta}$ in a wide temperature range (from high to room temperature) to prevent phase transition reversibly upon temperature decrease.

The Goldschmidt tolerance factor is able to describe the distortion degree of a perovskite structure from the standard cubic one. To form a cubic perovskite structure, the corresponding Goldschmidt tolerance factor should be close to 1. Given ionic radii of $r(Sr^{2+})(XII) = 1.44$ Å, $r(Co^{4+})(VI) = 0.53$ Å, $r(O^{2-})(VI) = 1.40$ Å,[89] the theoretical

Goldschmidt tolerance factor of an ideal stoichiometric perovskite $SrCoO_3$ is 1.04. To tune the tolerance factor closer to 1, two doping strategies can be utilized. One is B-site doping using the elements with ionic radius being greater than $r(Co^{4+})$(VI), such as Nb, Sc, Ti, Sb, Mo and Ta.[28-31, 33, 34, 90] However, a relatively high content of such elements, e.g., up to 20 mol% amount B-site doping, is required in order to stabilize cubic phase. This could deteriorate oxygen reduction reaction properties of the material, which are strongly dependent on valance and spin state of the B-site elements. Another strategy is to dope the element with smaller size than $r(Sr^{2+})$(XII) on A-site, which is much less studied in the literature. The radii of lanthanides in 12-fold coordinates decrease with an increase in atomic number, e.g., $r(La^{3+})$(XII) = 1.36 Å, $r(Ce^{3+})$(XII) = 1.34 Å, $r(Nd^{3+})$(XII) = 1.27 Å and $r(Sm^{3+})$(XII) = 1.24 Å. Even though exact radius of Yb^{3+}(XII) is not available in the radius chart, it is anticipated that Yb^{3+} in 12-fold coordinates would be smaller than that of Sm^{3+}.[89] This is consistent with those reported in other references, i.e., 1.22[91], 1.07[92] and 1.01[93] Å for Yb^{3+} in 12-fold coordinates. Therefore, a partial substitution of Sr by Yb on the A-site is expected to be able to tune the tolerance factor closer to 1, potentially stabilizing the cubic perovskite structure of $SrCoO_{3-\delta}$.

It has been recognized that Sr in $SrCoO_{3-\delta}$ can be demixed and segregated onto the surface of bulk cathode, leading to deterioration of electrode performance.[94, 95] Under practical operating conditions, an oxygen/air atmosphere surrounding the SOFCs cathode could contain a small amount of CO_2. When exposed to a CO_2-containing atmosphere, surface Sr could react with CO_2 to form carbonates on the oxide surface, blocking oxygen surface exchange.[96, 97] For instance, polarization resistances of

$Ba_{0.5}Sr_{0.5}Co_{0.8}Fe_{0.2}O_{3-\delta}$ and $SrSc_{0.175}Nb_{0.025}Co_{0.8}O_{3-\delta}$ cathode increase about 25 and 35 times, respectively, when exposed to 5% CO_2-containing air for 15 min compared to CO_2-free air at 600 ^oC.[98] After switching back to pure air, polarization resistances still remain over 2 times higher than the original ones due to the formation of surface (Ba, Sr)CO_3 compound.[98] In theory, the average bonding energy (ABE) can be used to evaluate stability of a material in different atmospheres. Taking $Sr_{1-x}Yb_xCoO_{3-\delta}$ as an example, with Co element on the B-site, calculations of Sr-O and Yb-O bonding energy in such ABO_3 perovskites are sufficient for their ABE comparison. Simple calculations indicate that the ABE of Yb-O, -119.45 kJ mol^{-1} is more negative than that of Sr-O, i.e., -83.80 kJ mol^{-1}.[59] Therefore, it is reasonable to expect that partial substitution of Sr on the A-site by Yb may lead to less oxygen loss and better thermal stability at elevated temperatures, and could also improve stability in CO_2 containing atmospheres. In addition, Yb possesses a higher electronegativity value (~1.1) than Sr (1.0)[99], meaning that Yb has a stronger power to attract electrons than Sr. Therefore, partial substitution of Sr with Yb on the A-site can decrease the basicity of the material and thus increase resistance against acidic gases.

In this chapter, a new series of $Sr_{1-x}Yb_xCoO_{3-\delta}$ (x = 0.05, 0.10 and 0.15) was synthesized and characterized including crystal structure evolution with Yb doping levels, oxygen reduction reaction kinetics and associated rate limiting steps, thermal stability, and stability in CO_2-containing atmosphere at elevated temperatures.

3.2 Experimental

3.2.1 Powder synthesis

$Sr_{1-x}Yb_xCoO_{3-\delta}$ (x = 0, 0.05, 0.10 and 0.15, simply denoted as SYbC0, SYbC5, SYbC10 and SYbC15, respectively) powders were synthesized by a combined ethylenediaminetetraacetic acid (EDTA)-citrate acid complexing sol-gel process. Specifically, stoichiometric amounts of $Sr(NO_3)_2$ (Alfa Aesar, 99.0%), Yb_2O_3 (Alfa Aesar, 99.99%) and $Co(NO_3)_2 \cdot 6H_2O$ (Alfa Aesar, 99.999%) were dissolved in diluted nitric acid. After a transparent solution formed under magnetic stirring, citric acid (99.0-102.0%, BDH) and EDTA (99.4-100.6%, BDH) were added into the solution with molar ratio of citric acid:EDTA:metal ions = 1.5:1:1 as complexants. The pH value of the solution was adjusted to about 8 by adding ammonium hydroxide. After being mixed homogenously, the precursor solution was heated in a water bath at 80 ^oC to evaporate excess water until a viscous gel was obtained. An electrical burner was then used to heat the gel until self-burned, forming a bouffant ash. The resulting precursor powder was ground and then calcined at 400 ^oC for 2 h to remove organic residues, and then 1000 ^oC in air for 6 h to form $Sr_{1-x}Yb_xCoO_{3-\delta}$ (denoted as SYbCx) phase, followed by high energy ball milling for 1 h with ethanol as milling medium.

3.2.2 Symmetrical cell preparation

To characterize the electrochemical performance of synthesized SYbCx materials, symmetrical cells with configuration of SYbCx | $Ce_{0.8}Sm_{0.2}O_{1.9}$ | SYbCx were fabricated. $Ce_{0.8}Sm_{0.2}O_{1.9}$ (SDC) electrolyte powder (tape cast grade, Fuel Cell Material, USA) was mixed and ground with a binder of polyvinyl butyral (PVB, 2 wt.%) in ethanol. After completely dried, the powder was uniaxially pressed at around 200 MPa using a stainless

steel die to form a disk with a diameter of ~15 mm. Green pellets were then sintered and densified at 1450 ^{o}C in air for 6 h. Surfaces of densified SDC pellets were polished with sand paper and then cleaned in ethanol in an ultrasonic cleaner. SYbCx cathode powders were mixed with a balanced amount of 6 wt.% ethyl cellulose-terpineol binder to form a cathode ink, which was then screen-printed onto both sides of each SDC pellet. After drying and aging, the symmetrical cells were sintered at 1050 ^{o}C in air for 2 h. Silver paste and wire were attached at either surface of electrodes as current collectors.

3.2.3 Characterization

X-ray diffraction (XRD, D/MAX-3C) with Cu Kα radiation (λ = 1.5406 Å) was employed to characterize phase purity and crystal structure of powder materials at room temperature. XRD data was collected over a 2θ range from 10-90^{o} with a step size of 0.02^{o}. Rietveld refinements were performed on XRD patterns of SYbC5 and SYbC10, respectively, with GSAS-II/EXPGUI software.[68] Transmission electron microscopy (TEM) measurements were performed on a Hitachi H-9500 TEM with an accelerating voltage of 300 kV. To prepare samples for TEM measurements, nanoparticle samples were diluted in ethanol and sonicated for 30 min to ensure a homogeneous distribution of particles. Two drops of the suspension were deposited onto a carbon stabilized Formvar-coated copper grid and completely dried at room temperature prior to measurement. The microstructure of the prepared samples was characterized with scanning electron microscope (SEM, Zeiss Ultra Plus FESEM, Germany).

Electrochemical impedance spectroscopy (EIS) of symmetrical cells with SYbC5 and SYbC10 as electrode materials was measured using a Zahner IM6E electrochemical workstation under open circuit voltage in the frequency range from 10^{6} to 0.1 Hz with a

voltage perturbation of 10 mV. To further investigate the kinetics of oxygen reduction reactions of cathode material, polarization resistances at different oxygen partial pressure ($p(O_2)$) and different temperatures were measured. Various $p(O_2)$ were obtained by adjusting the flow rate ratios of oxygen *vs.* nitrogen, controlled by flow meters (APEX). Oxygen and nitrogen were supplied to a three-way valve through two individual lines and mixed. The mixed oxygen/nitrogen gas then flowed into a surge flask before entering the alumina test chamber.

The stability of the synthesized material was characterized, including crystal structure stability and long-term stability as cathode material as well as stability in CO_2-containing atmosphere. In particular, to examine thermal stability, powders were annealed at 700 ^oC in air for 250 h, followed by XRD characterization. Long term stability of SYbC10 as cathode material was characterized at 700 ^oC in air for ~ 300 h, during which polarization resistance of symmetrical cell SYbC10 | SDC | SYbC10 was measured periodically. CO_2 tolerance and recovery capability of SYbC10 as cathode material were also characterized using symmetrical cell at 700 and 650 ^oC respectively. The atmosphere surrounding symmetrical cell was switched periodically between pure air and 5% CO_2-air. The polarization resistance of the symmetrical cell was measured every half hour.

3.3 Results and Discussion

3.3.1 Crystal structure characterization and analysis of as-prepared $Sr_{1-x}Yb_xCoO_{3-\delta}$ powders

The synthesis of a perovskite material usually starts from a precursor powder preparation, followed by calcination at elevated temperatures to form a desired crystal

phase. After cooling down, the formed phase at elevated temperatures is remained at room temperature. Unfortunately, undoped strontium cobalt oxide loses lattice oxygen at elevated temperature, forming $Sr_2Co_2O_5$ as described by reaction (3-1). During the cooling down process, $Sr_2Co_2O_5$ absorbs oxygen from air, forming $Sr_6Co_5O_{15}$ and Co_3O_4 as expressed by reaction (3-2).[100-103]

$$2SrCoO_{3-\delta} \leftrightarrow Sr_2Co_2O_5 + \frac{(1-2\delta)}{2}O_2 \quad (3\text{-}1)$$

$$3Sr_2Co_2O_5 + \frac{2}{3}O_2 \leftrightarrow Sr_6Co_5O_{15} + \frac{1}{3}Co_3O_4 \quad (3\text{-}2)$$

As shown in Figure 3.1, XRD patterns of our synthesized undoped $SrCoO_{3-\delta}$ does indeed consist of $Sr_6Co_5O_{15}$ and Co_3O_4, confirming that it is very difficult to synthesize a pure $SrCoO_{3-\delta}$ phase. Interestingly, upon substitution of Sr by Yb, the material phase is stabilized and exhibits a higher symmetrical perovskite phase. It is easy to see that SYbC5 and SYbC10 powders are well crystalized to a single phase respectively. With increasing Yb doping level to 15 mol%, secondary phase peaks appear in the SYbC15 XRD patterns (Figure 3.1), implying that a 10 mol% doping level seems to be the upper-limit for Yb solubility on the A-site of $SrCoO_{3-\delta}$. Using the basis of cubic structure (JCPDS 38-1148), indices of diffraction peaks of SYbC5 and SYbC10 are marked in Figure 3.1, indicating that main features of the XRD patterns could be explained by cubic phase with the perovskite structure. Accordingly, these materials exhibit a higher symmetrical structure of perovskite phase upon A-site partial substitution of Sr by Yb.

Figure 3.2a shows magnified XRD patterns of SYbC5 and SYbC10 in the range of 2θ = 38-56°. One can see that some small peaks appear at 42° and 48.5° in diffraction patterns. The magnified XRD patterns around $(200)_c$, $(211)_c$, $(220)_c$ in Figure 3.2b demonstrate increasingly obvious peak splitting of the XRD patterns. It is not

straightforward to interpret either additionally appeared small peaks or peak splitting based on the understanding of cubic crystal structure. The peak variations could be related to the distribution of oxygen vacancies in the crystal structure, for instance, oxygen vacancies in perovskite phase are not disordered completely and vacancy ordering can appear locally.[104] In fact, upon oxygen vacancy ordering, tetragonal superstructures (*I4/mmm*) can occur in Co-based perovskites, and has following relationship with the corresponding unit cell:

$$a_t \times a_t \times c_t \approx 2a_c \times 2a_c \times 4a_c \quad (3\text{-}3)$$

where a_t and c_t are lattice parameters of the tetragonal structure, while a_c is one of the corresponding primitive cubic unit cell.[105, 106] The two additional small peaks at 42° and 48.5° could originate from the supercell formed upon vacancy ordering, which can also explain the splitting of the peaks.[104] Thus, more than likely, the structures of SYbC5 and SYbC10 are tetragonal with oxygen ordering vacancies instead of cubic perovskite with disordered vacancies. With increasing Yb content from 5 to 10 mol%, two small peaks at 42° and 48.5° become less pronounced, indicating dissolution of the oxygen-ordered superlattice into an oxygen-disordered primitive cubic structure. Seemingly, a structural transition takes place from tetragonal towards cubic. In the meantime, the peaks shift to higher angles as shown in Figure 3.2, indicating that such a structural transition is accompanied by lattice shrink.

To further understand XRD data and examine the above analysis, Rietveld refinement was performed on these experimental XRD patterns of SYbC5 and SYbC10 by using the GSAS-II program, where the tetragonal structure with *I4/mmm* space group was used as an initial model. Figure 3.3a and 3b show the refinement results of XRD

patterns for SYbC5 and SYbC10, respectively. Table 1 lists the details of fitting and structure parameters. A reasonable low weighted profile R-factor (R_{wp}), integrated intensity R-factor (${R_F}^2$) and goodness of fit (χ^2) are achieved when the tetragonal *I4/mmm* space group is used to fit the experimental XRD data. And a good agreement was achieved between XRD profile and the fitting results as graphically shown in Figure 3.3, which ensures a good quality for Rietveld refinement. It can also be observed that partial substitution of Sr by Yb leads to smaller lattice and cell volumes, which is consistent with the XRD peak shifting in Figure 3.2. With increasing Yb-doping levels from 5 to 10 mol%, the corresponding $c_t/2a_t$ ratio gradually closes to 1, leading to a structural transition tendency towards a cubic lattice. This result is also consistent with the above analysis of crystal structure evolution. Schematic crystal structure of SYbC0 and SYbC10 is shown in Figure 3.4.

A transmission electron microscope (TEM) was employed to further characterize crystal structures of SYbC5 and SYbC10. Figure 3.5a and 5b show micro-morphology of SYbC5 and SYbC10 powders, respectively. More TEM images of SYbC10 powders are also provided in Figure 3.5. It can be seen that the powders consist of both large particles and small spherical particles. The small spherical particles with a diameter of ~2-3 nm can be observed (see dashed circle marks in Figure 3.5 and Figure 3.6). Additionally, some larger particles are formed with aggregation of small spherical particles (Figure 3.6). High-resolution TEM images in selected regions of SYbC5 and SYbC10 exhibit well-defined crystalline fringes as shown in Figure 3.5c and 5d respectively. Interplanar distances of 0.283 nm and 0.258 nm were obtained from the fringe measurements for SYbC5 and SYbC10, respectively, which is related to the $(220)_t$ or $(110)_c$ lattice plane.

Although interplanar distances obtained from these TEM images show a little bit difference from the above Rietveld refinement result due to measurement and fitting errors, variation tendency of lattice parameters is consistent with each other. All of these results suggest that partial substitution of Sr with 5 and 10 mol% Yb on A-site exhibits an evolution of the corresponding lattice structure and is able to stabilize high temperature phase of $SrCoO_{3-\delta}$ to room temperature.

3.3.2 Structural stability of synthesized powders after thermal treatment

SOFCs operate at elevated temperatures and require long-term stability of the involved materials, in particular, the cathode materials. The purpose of the partial substitution of Sr with Yb in $SrCoO_{3-\delta}$ mentioned above is to stabilize the high temperature crystal structure down to room temperature, so that crystal structure stability can be obtained in a wide operating temperature range. In this section, the thermal stability of the synthesized powders of SYbC5 and SYbC10 is evaluated. In particular, the as-prepared SYbC5 and SYbC10 powders were annealed at 700 ^{o}C in air for 250 h. The XRD patterns of the powders before and after annealing treatment were obtained. As shown in Figure 3.7, the materials maintained the same crystal structures before and after annealing treatment, indicating that both SYbC5 and SYbC10 powders are thermally stable at 700 ^{o}C in air.

3.3.3 Electrochemical performance and stability of SYbC5 and SYbC10 as electrode materials

To evaluate Yb dopant effect on electrochemical performance of SYbC5 and SYbC10, the polarization resistance (R_p) was measured on symmetrical cells using EIS under open circuit voltage conditions in the temperature range of 600-750 ^{o}C. SEM

images (Figure 3.8) show that SYbC5 and SYbC10 cathodes demonstrate intimate contact with SDC electrolyte and have sufficient porosity; the sintered particles also show good inter-connectivity throughout the cathode.

Figure 3.9 shows typical EIS of SYbC5 and SYbC10 electrodes measured at 700 ^{o}C in air. Spectra fitting results are shown in the same figure using an equivalent circuit with the configuration of $L - R_o - (R_h Q_h) - (R_l Q_l)$ (inset in Figure 3.9a). Here, L denotes inductance of the circuit, R_o represents ohmic resistance induced by electrolyte and electrode backbone as well as current collecting wires. R_i and Q_i are the resistance and constant phase capacitance of high (h) and low (l) frequency processes, respectively. The fitting results of R_h and R_l are corrected by electrode area and divided by two due to the symmetrical configuration of the cell. The polarization resistance of electrode R_p is then obtained by adding R_h and R_l together. The Bode plot in Figure 3.9b shows the frequency response of the imaginary part of the impedance spectra, indicating that the improved performance of SYbC10 electrode is mainly associated with low frequency processes. Arrhenius plots of R_p of SYbC5 and SYbC10 electrode at different temperatures and corresponding activation energy (E_a) are presented in Figure 3.10. Obviously, R_p decreases with increasing temperatures, indicating that electrochemical processes occurring in the electrode are thermally activated. Increasing the amount of Yb dopant from 5 mol% to 10 mol% resulted in a decrease in R_p. The SYbC10 electrode demonstrates R_p of 0.051, 0.115 and 0.272 Ω cm^2 at 750, 700 and 650 ^{o}C, respectively, lower than that of the SYbC5 electrode. Activation energy of SYbC10 is 1.39 eV, which is also lower than that of SYbC5 electrode, that is 1.57 eV. This could be attributed to crystal structure evolution induced by the Yb dopant. As mentioned previously, with

increasing doping content of Yb from 5 mol% to 10 mol%, a gradual structural transition took place from tetragonal structure with oxygen vacancy ordering towards disordered vacancies. Accordingly, SYbC10 possesses a structure similar to the ORR/OER active primitive cubic symmetry with disordered oxygen vacancies. This creates 3D pathways for oxygen ion transport, favoring electrode processes. The resulting lower R_p and E_a values obtained from the SYbC10 electrode, when compared to the SYbC5 electrode results, support this explanation.

ORR in porous SYbC10 electrode involves complicated multistep reactions. The reaction process is strongly dependent on oxygen pressures applied on electrode and determines electrode polarization resistance. Mathematically,

$$R_i = kP_{O_2}^{-m}, i = h, l \tag{3-4}$$

where, R is polarization resistance, k a constant, P_{O_2} oxygen partial pressure, m is reaction order and quantitatively related to each of multistep reactions as follows:

Step 1: molecular oxygen adsorption process onto porous electrode surface ($m = 1$)

$$O_{2,g} + SYbC10\ (s) \leftrightarrow O_{2,ads}(SYbC10) \tag{3-5}$$

Step 2: dissociation of adsorbed molecular oxygen into atomic oxygen ($m = 0.5$)

$$O_{2,ads}(SYbC10) \leftrightarrow 2O_{ads}(SYbC10) \tag{3-6}$$

Step 3: charge transfer reaction for oxygen anion formation and incorporation into oxygen vacancy ($m = 0.25$)

$$O_{ads}(SYbC10) + 2e^- + V_O^{\cdot\cdot} \leftrightarrow O_O^{\times} + SYbC10(s) \tag{3-7}$$

Figure 3.11a shows the correlation between high frequency polarization and applied oxygen partial pressures at different temperatures. It can be seen that reaction orders *m* of 0.28, 0.23, 0.29, and 0.27 are obtained at 600, 650, 700, and 750 ^{o}C respectively, which

are close to 0.25, suggesting that high frequency polarization is mainly associated with the charge transfer reaction process. Values of reaction order m for low frequency polarization are 0.48, 0.60, 0.57 and 0.59, respectively (Figure 3.11b), indicating that the low frequency polarization is mainly associated with dissociation process of adsorbed oxygen into atomic oxygen. Accordingly, oxygen molecule dissociation and charge transfer processes are the two rate-limiting steps for the SYbC10 cathode material.

Electrochemical kinetic stability of SYbC10 cathode

Durability is critical for practical applications of SOFCs cathode materials. In this section, a durability test was carried out using a symmetrical cell with SYbC10 electrode at 700 ^{o}C in air for ~ 300 h. EIS was measured periodically during the test. The polarization resistance R_p was then derived from the fitted EIS data as described in the previous section. Figure 3.12a shows time history of polarization resistances. It can be seen that R_p fluctuates in the first 50 hours, then increases a little bit between 50 and 175 h. Beyond 175 h, R_p gradually approaches an equilibrium state. Figure 3.12b shows EIS curves measured at 0th, 52th, 113th, 263th, 309th hour respectively. The EIS arcs gradually increase with time and reach an equilibrium state by the end of the test. As mentioned above, polarization resistance of electrode is contributed by several steps in the ORR. This increase in electrode polarization resistance could be linked to specific ORR steps, through which the degradation mechanism of electrode might be identified. For this purpose, time history of high (R_h) and low (R_l) frequency polarization resistances were obtained from the EIS measurements and shown in Figure 3.13a and 13b respectively. The R_h data shows some scatter in the first 100 hours, but gradually stabilizes and reaches a value comparable to (actually a little bit lower than) the values recorded at the

start of the durability test. Since high frequency polarization is associated with charge transfer process as confirmed above for oxygen anion formation and incorporation into oxygen vacancy, it is reasonable to assume that surface oxygen vacancy distribution and electronic structure near oxygen vacancies remain stable during the test. The fluctuations in the R_h data in the first 100 hours may be related to reorganization and stabilization of oxygen vacancy distribution on the electrode surface. The R_l data also fluctuates in the first 25 hours, but then slowly increases, and reaches a relatively stable value around 300th h. As mentioned above, low frequency polarization resistance is closely related to the dissociation process of adsorbed oxygen molecule into atomic oxygen. Certainly, the dissociation process is effected by the surface catalytic property of the electrode, so it is reasonable to assume that the increase of R_l could be induced by a change in electrode surface characteristics. For ABO_3 perovskites, both A-site and B-site elements could be exsolved onto the bulk surface in long-term thermal treatment condition.[95, 107-111] As shown in Figure 3.7, no any secondary phase can be found in XRD results of SYbC10 powders after 250 h thermal treatment, implying that either no element was exsolved from A-/B-sites or the amount of surface element exsolution was below the level detectable by the XRD. On the other hand, surface nano-particles are observed from the SEM image of SYbC10 electrode after the durability test (Figure 3.14b), indicating that some elements were indeed exsolved. It has been widely demonstrated that transition metal exsolution from the B-site usually improves catalytic property or surface exchange rate of the material.[112, 113] However, the increase of R_l shown in Figure 3.12b indicates that this is less likely the case. Therefore, the surface nano-particles in Figure 3.14b is most likely induced by the element exsolution from the A-site. In $Sr_{1-x}Yb_xCoO_{3-}$

$_{\delta}$, the size mismatch between dopant and host cations induces elastic energy in crystals. During long-term thermal treatment process, such an elastic energy may drive cation rearrangement, resulting in surface Sr segregation. Ideal cubic $SrCoO_{3-\delta}$ consists of SrO and CoO_2 planes alternating stacking with $-(SrO-CoO_2)_n-$ sequences. The Sr and Co cations have charges of +2 and +4, respectively, leading to neutral charge of $Sr^{2+}O^{2-}$ [0] and $Co^{4+}O_2^{2-}$ [0] planes. However, Yb with charge of +3 makes positive charge of $Yb^{3+}O^{2-}$ [+1] in the AO planes and potential formation of negatively charged $Co^{3+}O_2^{2-}$ [-1] in the BO_2 planes. The alternating stacking of the charged AO and BO_2 planes would result in polar surface, which in turn could electrostatically drive surface cation segregation. Due to the lower surface energy of SrO surface[114, 115], SrO-terminated surface is prone to be formed with segregated Sr. Therefore, surface Sr segregation of $Sr_{1-x}Yb_xCoO_{3-\delta}$ could be induced by both elastic force and electrostatic force during long-term thermal treatment. To keep charge neutrality, surface oxygen vacancies will be created. This process can be expressed as,

$$Sr_{Sr}^{\times} + O_O^{\times} \leftrightarrow V_{Sr}'' + V_O^{\cdot\cdot} + SrO_{surface} \quad (3\text{-}8)$$

The created surface oxygen vacancies via surface Sr segregation will improve surface oxygen exchange rate and ORR kinetics. However, when the amount of Sr segregation is beyond a certain level, it might block the neighboring oxygen vacancies and reaction sites.[116, 117] These understanding may explain the time history of R_l. In the first 10 hours, R_l shows a rapid decrease likely due to a small amount of surface Sr segregation. Beyond ~10th h, the amount of surface Sr segregation increases, leading to gradual increase of R_l values. The R_l data stabilizes around the 300th h, implying that surface Sr segregation reaches an equilibrium state. It seems that the increase of overall polarization

resistance R_p during the durability test is primarily induced by the increase of R_l, and therefore performance degradation could be mainly caused by surface Sr segregation.

3.3.4 CO_2 tolerance and recovery capability of SYbC10 cathode

Gas supplied to cathode electrodes of SOFCs may contain a small amount of CO_2 especially air from the surrounding ambient atmosphere. Even though CO_2 content is very low, it may easily adsorb onto cathode surface, forming several types of surface adsorbates. Surface adsorbed CO_2 could even react with cathode material, resulting in surface secondary phases.[118] This usually occurs for Sr containing perovskite cathodes, where surface oxo-carbonaceous species are formed at elevated temperatures, such as adventitious-like carbon species, monodentate carbonate, bidentate carbonate and carbonate species.[119, 120] Such surface oxo-carbonaceous species block ORR active sites and deteriorate surface (electro)catalytic properties, causing degradation of cathode electrodes. Although degradation alleviation is possible by annealing at a relatively high temperature, e.g., decomposition of $SrCO_3$ in air[121, 122] and desorption of surface oxo-carbonaceous species, the high temperature process may induce other problems such as microstructure coarsening of electrodes and unwanted side reactions at interfaces within the device, which make it difficult to recover to its initial state and performance. In this section, stability and recovery capability of SYbC10 as cathode material is evaluated using a symmetrical cell in CO_2-containing atmosphere at elevated temperatures. For this test, a symmetrical cell SYbC10/SDC/SYbC10 was sealed in an alumina tube chamber. Pure air and 5% CO_2-containing air were supplied into the chamber alternatively every 2 hours for the first 12 hours. After 12 hours, pure air was constantly supplied into the chamber without switching to CO_2 containing air. EIS was

measured every half hour during the testing. R_o and R_p were then extracted from the EIS data. Figure 3.15 shows the time history of R_o and R_p at 700 and 650 °C respectively. It can be seen that at 700 °C, the ohmic resistance remained stable for the first ~ 7 hours, then showed a small increase, and stayed unchanged for the remainder of the test (Figure 3.15a). It did not show any obvious variations following the applied cycling between pure air and 5% CO_2-air. This observation indicates that variations in R_O are mainly induced by the thermal ageing process, in which the cell may experience microstructure evolution during the course of stability test at 700 °C. The polarization resistance in Figure 3.15b clearly shows fluctuations that followed the applied cycles of surrounding gas atmosphere. R_p was relatively low in pure air but quickly increased to a high value once gas atmosphere was switched to 5% CO_2-air. This result indicates that SYbC10 material is very sensitive to CO_2 but reversible from CO_2-contaminated state. Interestingly, after a few gas cycles, R_p becomes lower than the initial value, implying that surface phase/microstructure favoring electro-catalytic property of electrode could be formed, which is not completely clear at this stage. In addition to potential adsorption/desorption of surface carbonaceous species, it is assumed that following surface reactions are occurring:

In 5%-CO_2 containing Air:

$$Sr_{0.9}Yb_{0.1}CoO_{3-\delta} + xCO_2 \rightarrow xSrCO_3 + Sr_{0.9-x}Yb_{0.1}CoO_{3-\delta} \quad (3\text{-}9)$$

In pure air:

$$SrCO_3 + O_2 \rightarrow SrO + CO_2 \ \ (in\ pure\ air) \quad (3\text{-}10)$$

At the temperature of 700 °C, Sr segregation first occurs and appears on the cathode surface. When CO_2 is adsorbed onto the cathode surface, the surface segregated

Sr and/or lattice Sr is converted into $SrCO_3$ (reaction 3-9). Figure 3.16 shows XRD patterns of SYbC10 powders after treated in 5% CO_2-air for 2 h at 650 and 700 ^oC respectively followed by cooling down under the protection of nitrogen gas. It can be seen that the peaks corresponding to $SrCO_3$ phase occurred. This result confirms the assumption that CO_2 did react with Sr in SYbC10, forming $SrCO_3$ phase. After switching to pure air, the chemisorbed surface carbonaceous species are desorbed and the formed $SrCO_3$ is decomposed into SrO and CO_2 at 700 ^oC (reaction 3-10). In fact, after SYbC10 powders were treated at 700 in 5% CO_2-air for 2 h followed by treatment in pure air for another 2 h at 700 ^oC, $SrCO_3$ phase completely disappeared but SrO phase appeared as shown in Figure 3.17. After a few gas cycles, the nano-porous surface and/or surface micro-composition that favors ORRs on the electrode may be formed, leading to the smaller values of R_p. At a lower temperature of 650 ^oC, the variations in ohmic resistance synchronize with the cycles of applied gas atmosphere (Figure 3.15c). Interestingly, R_o was slightly larger during the pure air portion of the cycle than in the 5% CO_2-air portion of the cycle. Variation in polarization resistance also followed the cycles of applied gas atmosphere, low in pure air cycle but high in 5% CO_2-air cycle (Figure 3.15d). While R_p remained relatively constant in pure air after the first gas cycle; in 5% CO_2-air, it increased by ~350% of its initial value, but began decreasing following every subsequent gas cycle. After air treatment, R_p at the 28th h showed a little higher value than its initial one before the cycling test.

Based on above analysis and experimental results, one can see that R_p variations of SYbC10 electrode are attributed to two major surface factors during the atmosphere switching between pure air and 5% CO_2-air: one is surface oxo-carbonaceous species,

e.g., adventitious-like carbon and (bi)carbonate species, induced by direct chemisorption of CO_2; another is surface $SrCO_3$ phase formed by chemical reaction of Sr and CO_2. At elevated temperatures, SYbC10 electrode will lose oxygen and generate more oxygen vacancies. It has been reported that surface oxygen vacancy is the acidic center for the adsorption of CO_2.[123] This may lead to more CO_2 reacting with surface Sr, forming $SrCO_3$ phase in 5% CO_2-air since perovskite with more oxygen vacancies is more susceptible to CO_2.[124] It is reasonable to assume that the amount of $SrCO_3$ phase formed at 700 ^oC will be more than that at 650 ^oC. This understanding is confirmed by XRD results in Figure 3.15, where after SYbC10 powders were treated in 5% CO_2-air for 2 h at 650 and 700 ^oC respectively, the secondary phase of $SrCO_3$ was formed. And the relative peak intensity of $SrCO_3$ at 700 ^oC is stronger than that at 650 ^oC, indicating that the formation of strontium carbonates is more favorited at higher temperatures for SYbC10. On the other hand, it has been recognized that surface oxo-carbonaceous species, e.g., adventitious-like carbon and (bi)carbonate species, are favorably chemisorbed at lower temperatures.[119] In other words, it is difficult to desorb such surface oxo-carbonaceous species at lower temperatures. Both the formed surface strontium carbonate and chemisorbed surface oxo-carbonaceous species will block reaction sites for surface oxygen exchange. Since the formed surface strontium carbonate and chemisorbed surface oxo-carbonaceous species are sensitive to operating temperatures, the combinational effect of these two surface factors leads to different R_p behaviors at 650 ^oC from those at 700 ^oC. This could be the reason that the increase of R_p (or the increase ratio of R_p relative to its initial value) at 650 ^oC is bigger than that at 700 ^oC when the atmosphere is switched from pure air to 5% CO_2-air (Figure 3.15). After the

atmosphere is switched from 5% CO_2-air back to pure air, R_p at 700 °C rapidly recovers and reaches a value that is a little bit lower than its initial one (Figure 3.15b). This result implies that not only the chemisorbed surface carbonaceous species are completely desorbed but also the formed surface strontium carbonates are fully decomposed. Meanwhile, the decomposition of surface strontium carbonates might also introduce porous nano-surface structures favoring ORRs. By contrast, R_p at 650 °C shows only partial recovery and reaches a value that is higher than its initial one (Figure 3.15d). This observation indicates that the chemisorbed surface oxo-carbonaceous species are not completely desorbed and/or the formed surface strontium carbonates are not completely decomposed at 650 °C after the atmosphere is changed back to pure air from 5% CO_2-air. As a consequence, the surface ORR sites of SYbC10 electrodes are still partially blocked. The non-complete recovery of ORR sites also leads to a hysteresis behavior in the cell resistance at 650 °C during the atmosphere cycles between pure air and 5% CO_2-air. In open literatures, the R_p of the widely-studied $Ba_{0.5}Sr_{0.5}Co_{0.8}Fe_{0.2}O_{3-\delta}$ (BSCF)[98] may reach 9 times its initial value after being exposed to 10% CO_2 for 15 min at 700 °C, and 27 times its initial value after being exposed to 5% CO_2 for 15 min at 600 °C. The maximum R_p of SYbC10 developed in this paper only reached ~ 2.1 times (Figure 3.15b) and 4.5 times (Figure 3.15d) at 700 °C and 650 °C respectively after being exposed to 5% CO_2 for 30 min. This simple comparison indicates that SYbC10 has good property for CO_2 tolerance. The partial substitution of Sr by Yb with higher electronegativity on A-site is able to mitigate CO_2 adsorption onto SYbC10 electrode surface.

3.4 Conclusion

A new series of $Sr_{1-x}Yb_xCoO_{3-\delta}$ (x = 0, 0.05, 0.10 and 0.15) with different Yb doping concentrations has been synthesized and systematically characterized. Results indicate that $Sr_{0.95}Yb_{0.05}CoO_{3-\delta}$ and $Sr_{0.90}Yb_{0.10}CoO_{3-\delta}$ samples possess a tetragonal superstructure phase with oxygen vacancy ordering (*I4/mmm*;). With increasing the amount of Yb doping level, the phases demonstrate a transition tendency towards cubic structure with disordered oxygen vacancies. Both SYbC5 and SYbC10 phases show excellent thermal stability at 700 ^oC. Due to the less ordered oxygen vacancies, SYbC10 demonstrates very good ORR activity with polarization resistance of 0.051, 0.115 and 0.272 Ω cm^2 at 750, 700 and 650 ^oC, respectively. Dissociation of adsorbed oxygen and charge transfer processes are the two rate-limiting steps in the ORR for the SYbC10 cathode. Durability testing (~ 300 h) in combination with EIS analysis indicates that surface oxygen vacancy distribution and electronic structure near oxygen vacancies are very stable but dissociation of adsorbed oxygen molecule into atom oxygen process is affected by surface Sr segregation, and polarization resistance degradation is mainly induced by surface Sr segregation. SYbC10 is very sensitive to CO_2 containing atmospheres. At a relatively high temperature of 700 ^oC, the polarization resistance closely follows the cycles between pure air and CO_2-air and has a relatively higher values during CO_2-air portion of the cycle. This effect is temporary and polarization performance completely recovers in pure air cycle, likely due to complete desorption of surface oxo-carbonaceous species and decomposition of surface carbonates. The polarization resistance after a few gas cycle treatments becomes lower than that before the CO_2 treatment, probably due to surface nanostructures induced by cyclic formation

and decomposition of surface carbonates. At a relatively low temperature of 650 ºC, the polarization resistance still follows the same cyclic behavior, but complete recovery from CO_2-air portion of cycle is not observed, leading to hysteresis behavior likely due to non-complete desorption of surface oxo-carbonaceous species and/or non-complete decomposition of surface carbonates after switching to pure air portion of cycle. After a few pure air to 5% CO_2-air cycles at 650 ºC, the polarization resistance of SYbC10 electrode increases from the initial data in pure air. This work provides a promising strategy to stabilize $SrCoO_{3-\delta}$ through a simple cation doping method while obtaining very good electrochemical kinetic properties and stability of the material. The material developed in this study can be used as an alternative cathode for intermediate temperature SOFCs toward commercial applications.

Table 3.1 Structure parameters and R-factors for SYbC5 and SYbC10 derived from Rietveld refinement using XRD data at room temperature.

	$x = 0.05$	$x = 0.10$
a_t (Å)	7.6944(7)	7.6813(0)
c_t (Å)	15.4117(7)	15.3809(7)
$c_t/2a_t$	1.00147(9)	1.00119(5)
V(Å^3)	912.453	907.513
χ^2	6.29	4.67
R_{wp} (%)	3.01	2.26
${R_F}^2$ (%)	6.02	2.63

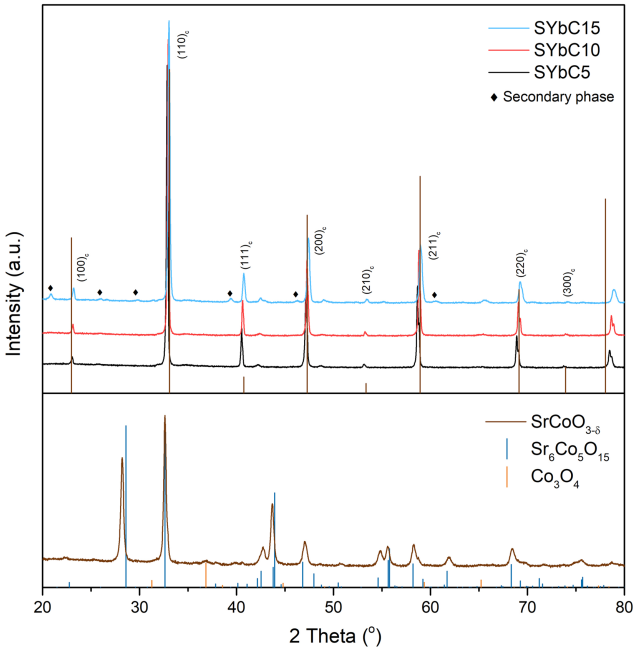

Figure 3.1 XRD patterns of $Sr_{1-x}Yb_xCoO_{3-\delta}$ (x = 0, 0.05, 0.10 and 0.15) powders calcinated at 1000 ^oC in air for 6 h, peak positions of $Sr_6Co_5O_{15}$, and Co_3O_4 and indices of simple cubic structure $SrCoO_{3-\delta}$ (Pm-3m, JCPDS 38-1148).

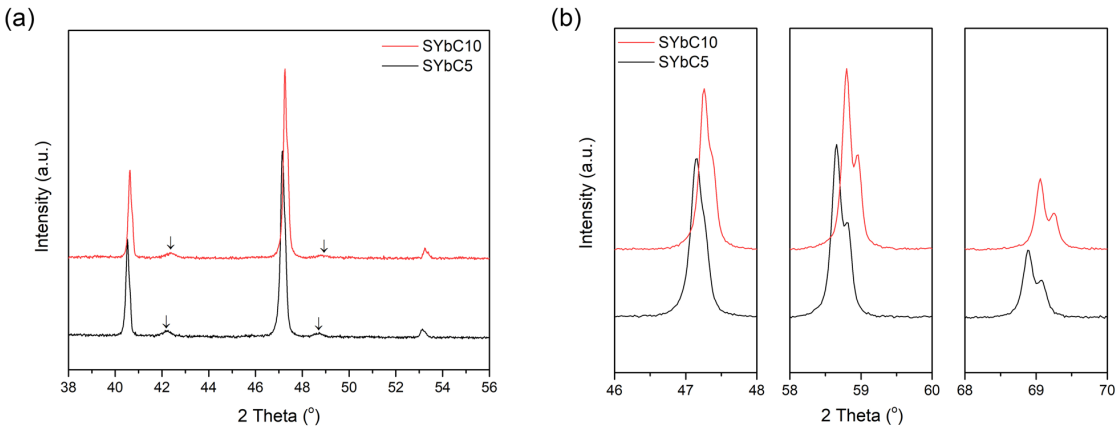

Figure 3.2 Magnified XRD patterns of SYbC5 and SYbC10 powders calcinated at 1000 °C in air for 6 h: (a) 2θ = 38-56°; (b) $(200)_c$, $(211)_c$, $(220)_c$ peaks.

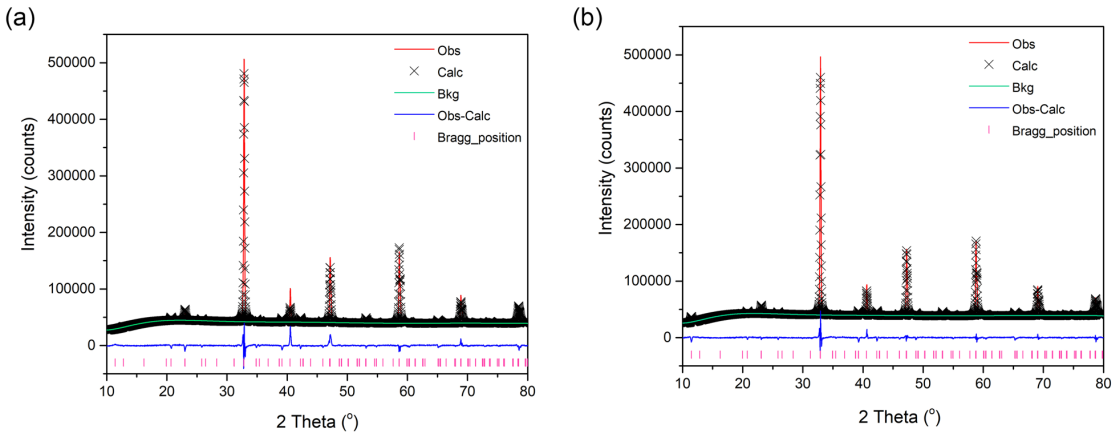

Figure 3.3 Rietveld refinement plot of SYbC5 (a) and SYbC10 (b) powders at room temperature using XRD data.

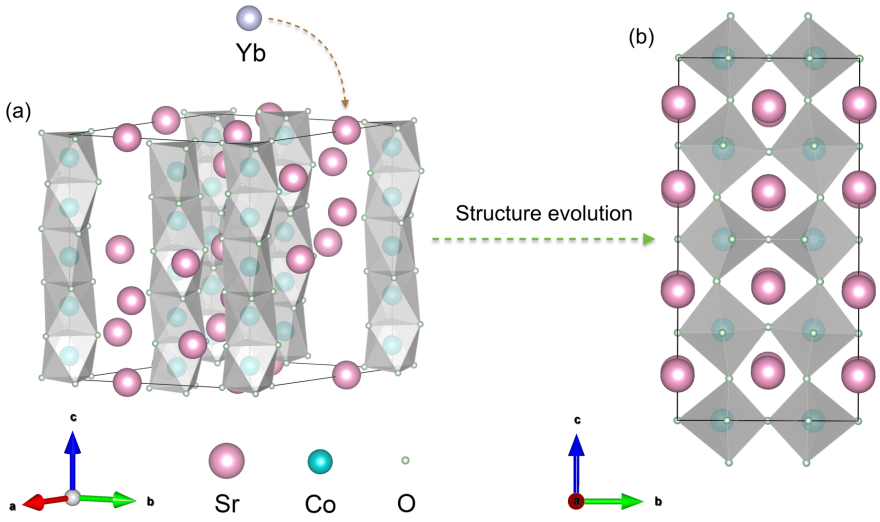

Figure 3.4 Schematic crystal structure: (a) SYbC0 at room temperature ($Sr_6Co_5O_{15}$, space group *R32*), (b) SYbC10 at room temperature (space group *I4/mmm*). The crystal structures are visualized with VESTA program.

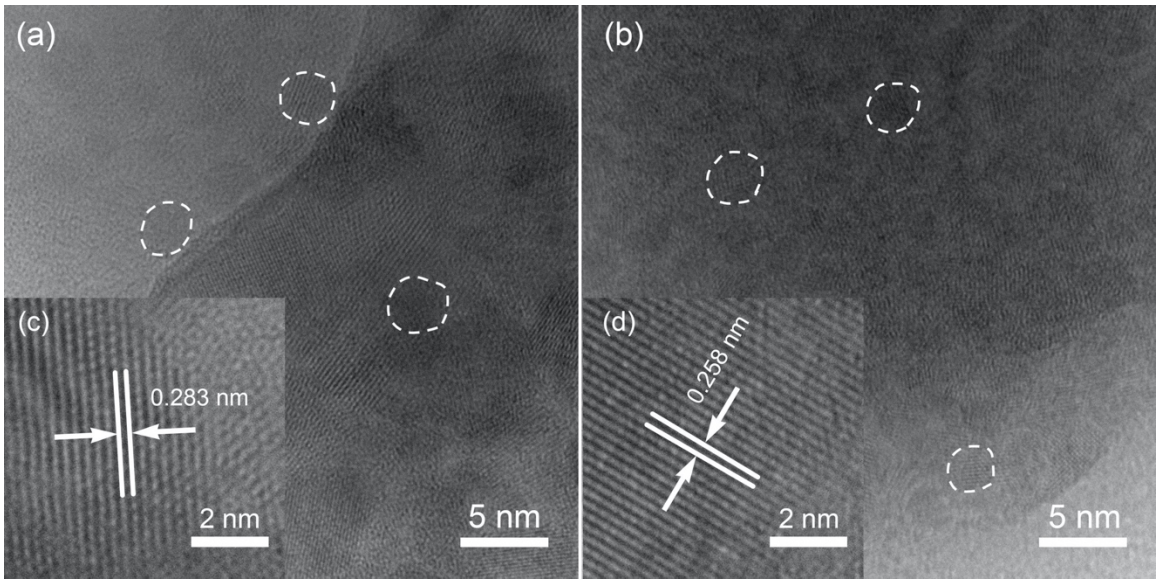

Figure 3.5 High-resolution TEM images of SYbC5 (a) and SYbC10 (b) powders after high energy ball milling and interplanar distance of SYbC5 (c) and SYbC10 (d) powders.

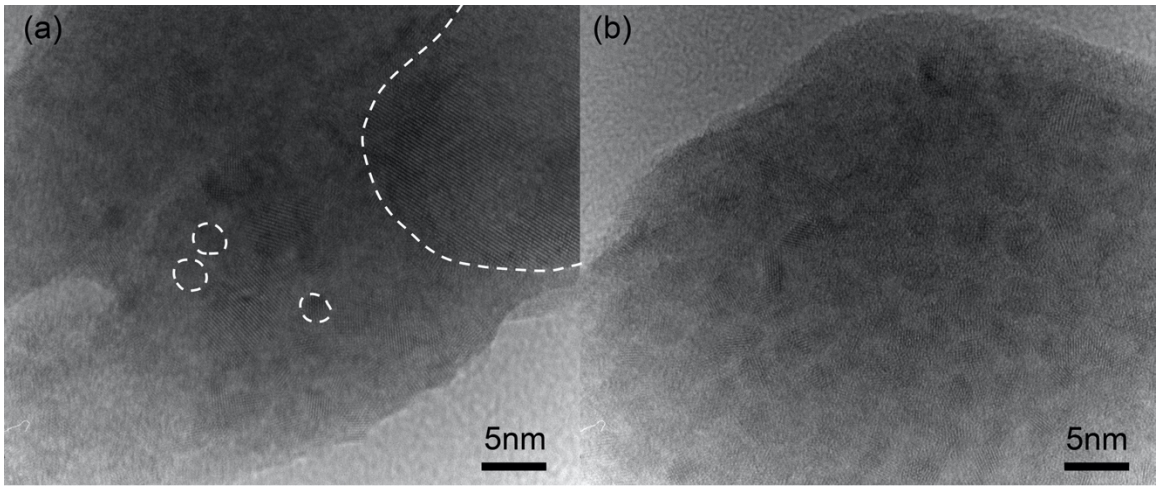

Figure 3.6 TEM images of SYbC10 powder: (a) particles with different sizes are marked, (b) aggregation of small particles.

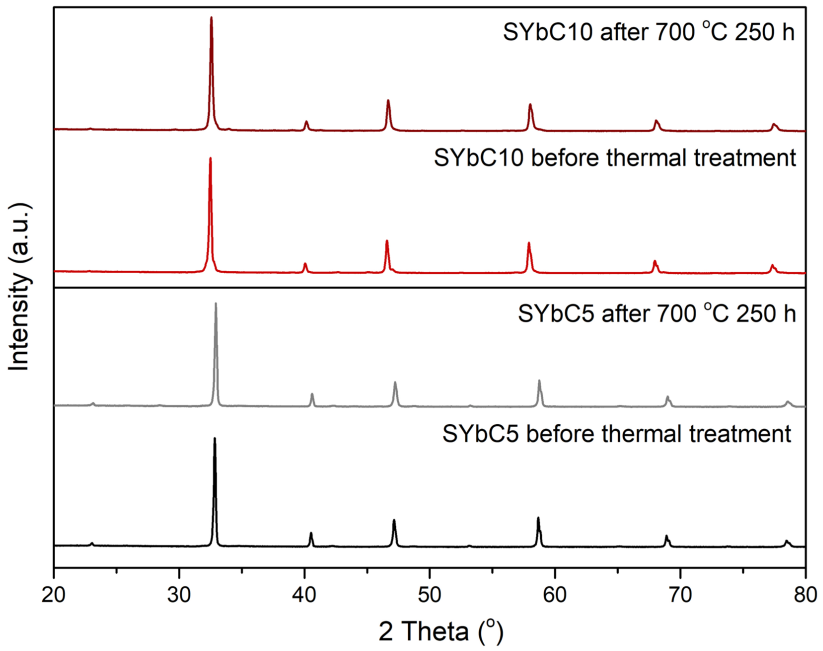

Figure 3.7 Polarization resistance *vs* 1000/T of SYbC5 and SYbC10 electrode measured in air from 750-600 ºC.

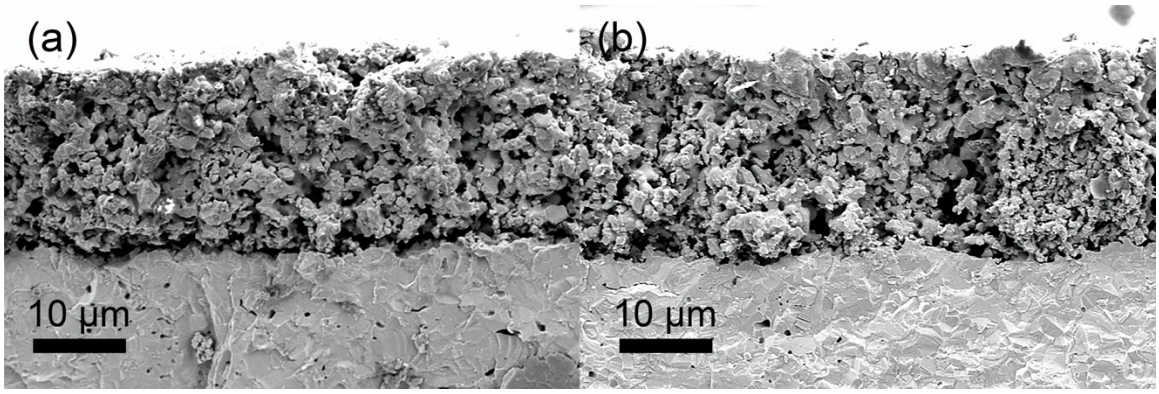

Figure 3.8 Cross-sectional SEM micrographs of symmetrical cell with SYbC5 (a) and SYbC10 (b) electrode sintered at 1050 ^{o}C in air for 2 h.

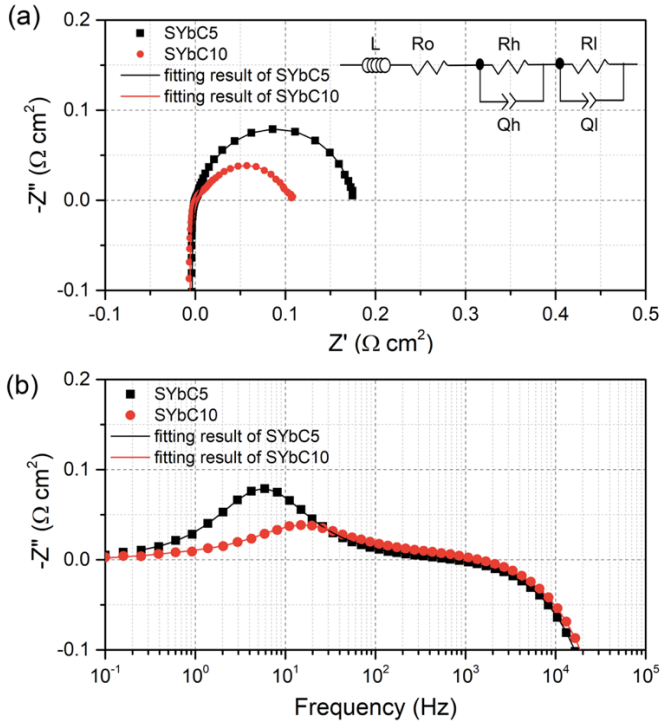

Figure 3.9 Typical Nyquist (a) and Bode (b) plots of symmetrical cells with SYbC5 and SYbC10 electrode measured at 700 ºC in air. The inset is an equivalent circuit model used for curve fitting.

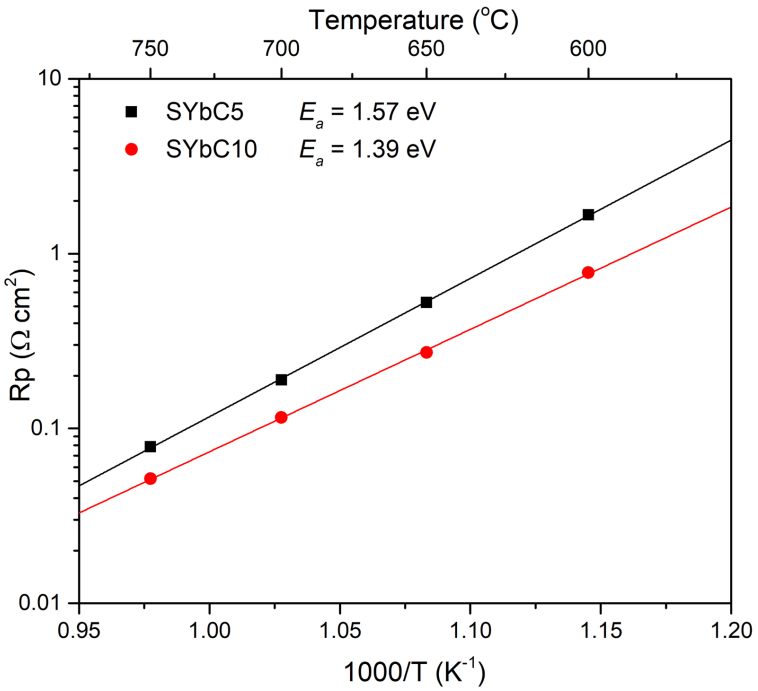

Figure 3.10 Polarization resistance *vs* 1000/T of SYbC5 and SYbC10 electrode measured in air from 750-600 °C

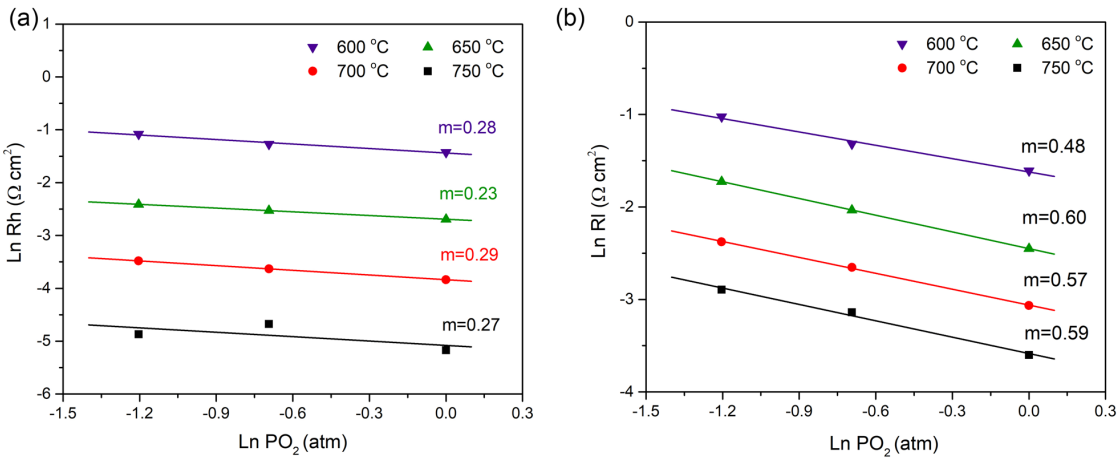

Figure 3.11 Correlations between Rh (a), Rl (b) and applied oxygen partial pressures at different temperatures.

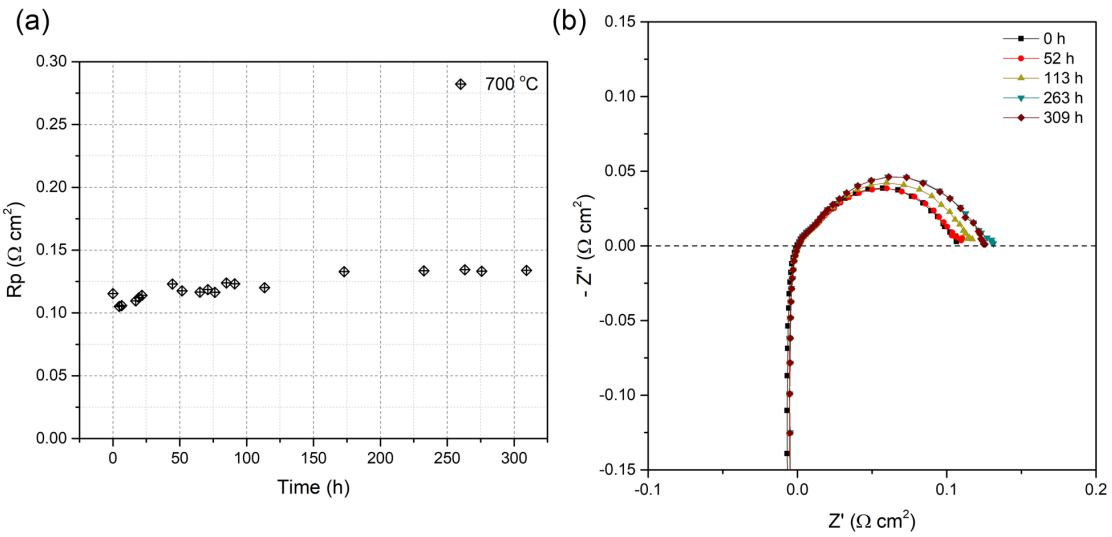

Figure 3.12 Long-term stability of SYbC10/SDC/SYbC10 symmetrical cell in air at 700 ºC: (a) time history of polarization resistance, (b) evolution of EIS at selected measurement points.

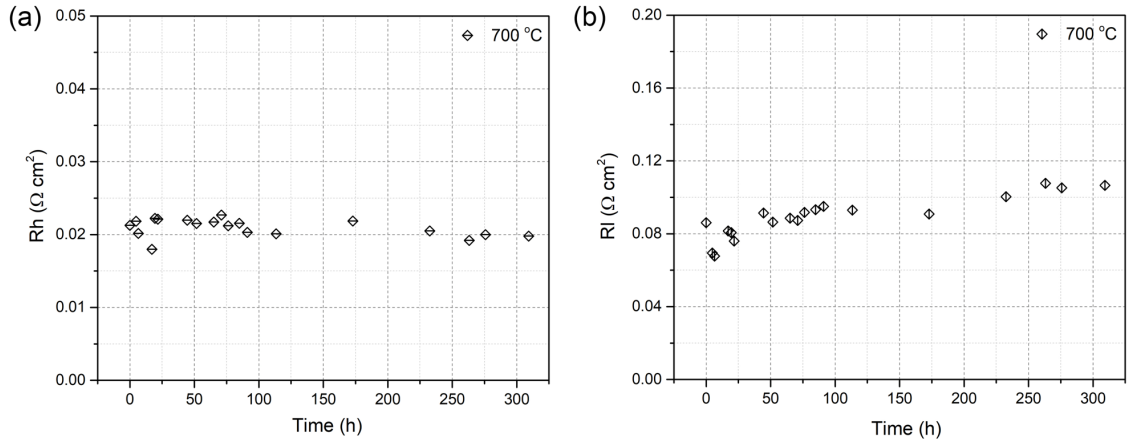

Figure 3.13 Time history of polarization resistance associated with high frequency (a) and low frequency (b) process for SYbC10 cathode at 700 °C in air.

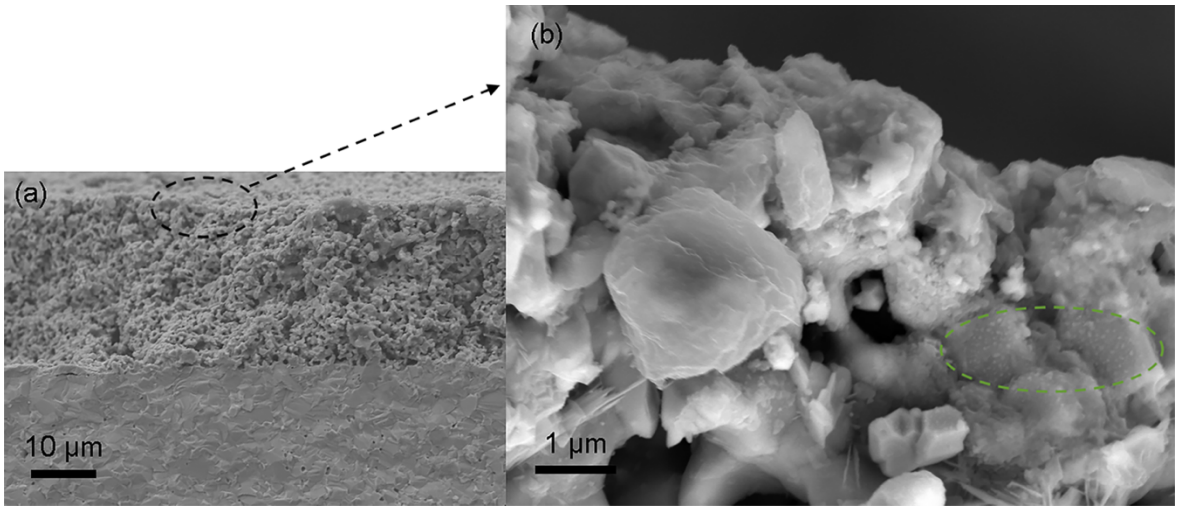

Figure 3.14 Cross-sectional SEM micrographs of symmetrical cell with SYbC10 electrode after durability test (a) and locally enlarged SEM image (b), the area with surface exsolved nano-particles are marked.

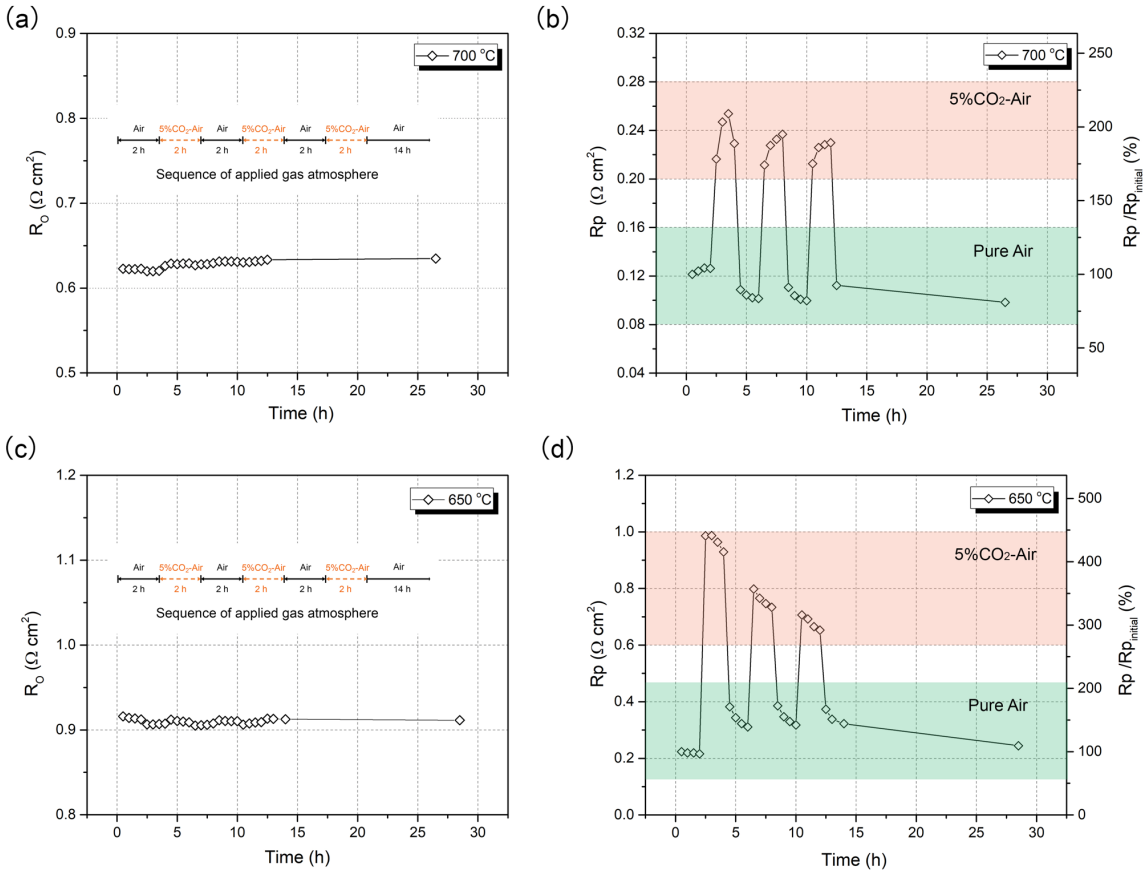

Figure 3.15 Time history of ohmic and polarization resistance evolution curves of SYbC10 electrode in applied gas cycles between air and 5% CO_2-air at 700 (a and b) and 650 ^oC (c and d).

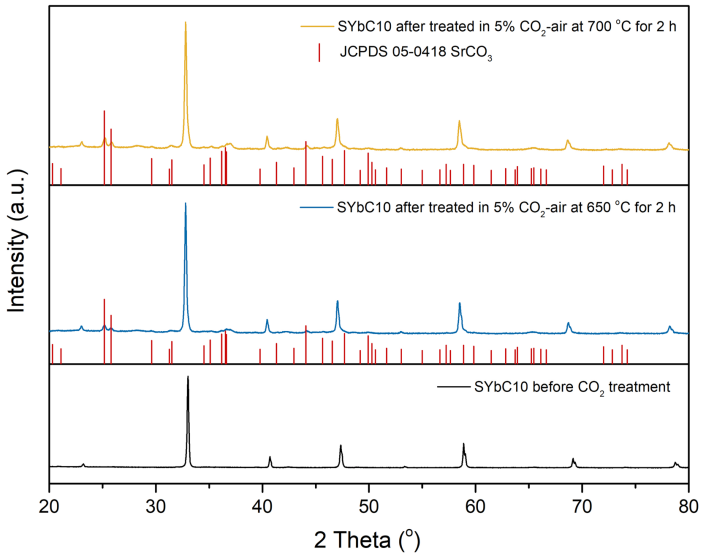

Figure 3.16 XRD patterns of SYbC10 powders before and after treated at 700 and 650 ºC respectively in 5% CO_2-air for 2 h followed by cooling down under the protection of nitrogen gas, and peak position of $SrCO_3$ (JCPDS 05-0418).

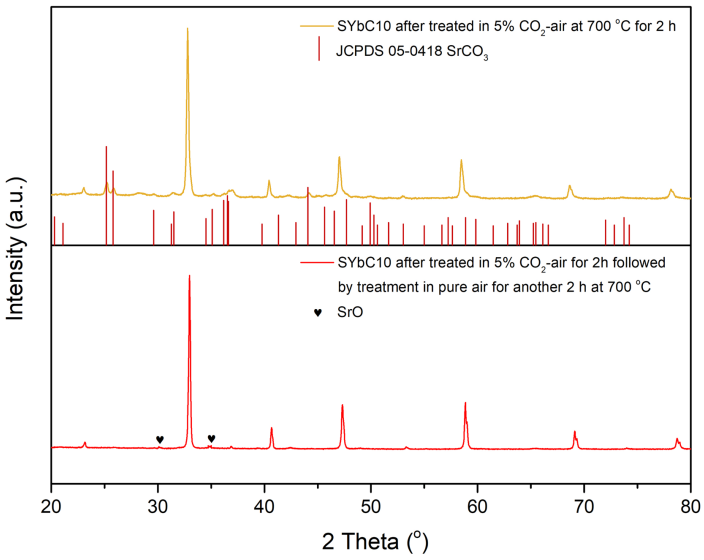

Figure 3.17 XRD patterns of SYbC10 powders after treated at 700 in 5% CO_2-air for 2 h followed by cooling down under the protection of nitrogen gas, and those after treated at 700 in 5% CO_2-air for 2 h followed by treatment in pure air for another 2 h at 700 ^oC

CHAPTER 4

A NANOPARTICLE-DECORATED MULTI-PHASE COMPOSITE CATHODE FOR LOW-TEMPERATURE SOLID OXIDE FUEL CELLS WITH PROMOTED KINETIC PROPERTY

4.1 Introduction

Low-temperature Solid oxide fuel cells (LT-SOFCs) have attracted considerable attention as the "next generation" technology.[4, 82, 125] Reducing the operating temperature to low temperature range (LT, ≤ 650 ^{o}C) have the potential to further reduce cost due to wider material choices for interconnects, sealing materials and balance-of-plant, enable acceleration in cell start-up and shut-down.[1, 8, 126] All these features could improve prospects for SOFCs commercialization in applications including base-load power plants, portable and transportation market, etc..[127] As mentioned above, with the reduction of operating temperature to low temperature range, insufficient cathodic performance becomes the major challenge because of the thermal activation nature of the processes in the cathode. As such, it is of interest to develop novel cathode materials or innovation cathode microstructures with excellent kinetic property that enables the operation of SOFCs below 650 ^{o}C.[128]

SOFCs cathode materials primarily consist of perovskites, which are mixed ionic and electronic conductors (MIEC).[129] Due to perovskites' versatile composition, fine-tuning their properties becomes possible.[130] A range of new perovskite cathode

materials have been developed, often yielding excellent performance. Cobalt-containing perovskite are of particular interest, such as $La_{0.6}Sr_{0.4}Co_{0.2}Fe_{0.8}O_{3-\delta}$, $Ba_{0.5}Sr_{0.5}Co_{0.8}Fe_{0.2}O_{3-\delta}$, $Sr_{0.95}Nb_{0.1}Co_{0.9}O_{3-\delta}$, show excellent ORR activity at low temperatures.[21, 131, 132] However, these Co-containing cathode materials always suffer from low chemical stability. O-migration is promoted by the flexible Co(III)/Co(IV) redox behavior which also decrease the stability of the compounds at the same time.[133] Compared with Co, Fe is an less expensive additive. Fe-containing cathodes attract widespread attention because of their higher chemical stability such as $Ba_{0.5}Sr_{0.5}Cu_{0.2}Fe_{0.8}O_{3-\delta}$, $SrFe_{0.9}Nb_{0.1}O_{3-\delta}$, etc..[134, 135] However, their practical application is still restricted by insufficient ORR activity. Moreover, strontium in these MIEC also causes Sr-segregation which could induce performance degradation.[95] Thus, it is challenging to develop a single-phase material to meet all the requirements as a cathode for SOFCs.[136]

To improve cathode performance at low temperatures, the formation of composite material and fabrication of nanostructured cathode could be alternative strategies. For the composite material, different components performed different functionalities can be combine together. For example, a MIEC mixed with an oxygen ion conductor can provide excellent performance at low temperature, such as $(La_{0.8}Sr_{0.2})_{0.95}MnO_{3-\delta}$-$(Er_{0.2}Bi_{0.8})_2O_3$.[137] For this type of composite material, both phases are synthesized separately and mixed mechanically. Thus the composite material is mixed in micrometer scale and interfaces between the two phases are limited. So the development of nanoscale composite could be a better choice to enhance ORR kinetic properties because of enlarged two-phase boundaries. Recently, a nanocomposite $BaCo_{0.7}(Ce_{0.8}Y_{0.2})_{0.3}O_{3-\delta}$ was developed as dual-ion conducting fuel cell cathode. The nanoscale interfaces within the

composite increased the active site for ORR and greatly promotes the cathode performance.[138]

Decorated active nanoparticles on cathode supports have been proven to be an effective method delivering excellent catalytic performance.[139-142] Infiltration technique is an effective method to introduce catalytic nanoparticles onto a pre-fired porous scaffold. And in most cases, these two materials are different, thus the formed electrode can also be seen as another type of composite material. Infiltration process has several steps including preparation of porous cathode backbones at high temperatures, infiltration of a precursor liquid solution into the backbone, and then subsequently thermal treated.[143] Decorating perovskite oxides-based nanoparticles on the surface is reported to significantly enhance the catalytic activity of the electrodes for ORR. For example $Sm_{0.5}Sr_{0.5}CoO_{3-\delta}$ nanoparticles are deposited on the surface of a porous LSCF cathode which reduce the polarization resistance of the cathode, achieving polarization resistance of 0.688 Ω cm^2 at 550 ^oC.[144] Modification of selected electrode by exsolution of precious metals has emerged as effective method to improve kinetic property of cathode materials. For instance, Ag was incorporated into A-site of $Sr_{0.95}Nb_{0.1}Co_{0.9}O_{3-\delta}$ to form $Sr_{0.95}Ag_{0.05}Nb_{0.1}Co_{0.9}O_{3-\delta}$. After treated in reducing atmosphere, Ag nanoparticles exsolved from the perovskite lattice and decorated on the cathode surface, which highly promoted catalytic property.[141] However compared with normal one-step sintering, both infiltration method and exsolution of nano-decorators are complicated and effort cost processing procedures.

Inspired by the composite material and nanoparticle decorated cathode structure, we report a nanocomposite material with the nominal composition $Sm_xBa_{1-x}Co_{0.8}Fe_{0.2}O_{3-\delta}$

investigated as a potential cathode material for LT-SOFCs. The material can be self-assembled to form the nano-composite. Among them, $Sm_{0.1}Ba_{0.9}Co_{0.8}Fe_{0.2}O_{3-\delta}$ is consisted of a main phase of A-site cation deficiency cubic phase $Ba_{1-x}(Co/Fe)O_{3-\delta}$ type perovskite, and a minor tetragonal phase layered perovskite $SmBa(Co/Fe)_2O_{5+\delta}$. For the single perovskite, the introduction of less easily reducible Fe into the B-site could obtain proper stability-activity tradeoff. And A-site cation deficiency can effectively facilitate the creation of additional oxygen vacancies due to the electrical neutrality ,and benefit for the mobility of oxygen due to increasing of the lattice free volume. And the increase of the charge carriers and decrease of the migration barriers improve electro-catalytic activity for ORR.[145] However, the $Ba_{1-x}(Co/Fe)O_{3-\delta}$ type single perovskites always have low electrical conductivity. For instance, the electrical conductivity of $(Ba_{0.5}Sr_{0.5})_{0.91}Co_{0.8}Fe_{0.2}O_{3-\delta}$ is 9.7-26.6 S cm^{-1} at 300-800 ^oC, while $Ba_{0.95}Co_{0.7}Fe_{0.2}Nb_{0.1}O_{3-\delta}$ has the electrical conductivity of 2.2-10.2 S cm^{-1} at 300-800 ^oC.[54, 146] And for the recent popular cathode material for LT-SOFC $BaCo_{0.4}Fe_{0.4}Zr_{0.1}Fe_{0.1}O_{3-\delta}$, the electrical conductivity is 0.4-2.2 S cm^{-1} at 300-800 ^oC.[147] And as a good cathode materials, sufficient electronic conductivity is desirable to minimize ohmic losses when used in conjunction with a suitable current collector, typically > 100 S cm^{-1} at ~ 600 ^oC.[8] On the other hand, the layered perovskites have high electrical conductivity and high rates of oxygen surface and O-ion diffusivity, as well as phase stability.[129] For example, the electrical conductivity for $SmBaCo_2O_{5+\delta}$ is 500-800 S cm^{-1} at 600 ^oC.[148, 149] Thus, the combine of two type materials can effective improve the electrical property of the composite material. The $Sm_xBa_{1-x}Co_{0.8}Fe_{0.2}O_{3-\delta}$ composite are fabricated by the self-assembly process which can induce

the strong interactions and uniform distribution in nanodomain which can increase active sites for ORR, thus enhancing electro-catalytic kinetics. Besides of the nature of the nanocomposite material, some nanoparticles also decorated on the surface of the main phase. Compared with the infiltration and exsolution process, the fabrication of our new cathode is just a one-step procedure which is very simple. In this chapter, a new series of $Sm_xBa_{1-x}Co_{0.8}Fe_{0.2}O_{3-\delta}$ was synthesized. The crystal structure, electrical conductivity, electrochemical performance as well as single cell performance and stability at low temperature were systematically investigated.

4.2 Experimental

4.2.1 Powder synthesis

$Sm_xBa_{1-x}Co_{0.8}Fe_{0.2}O_{3-\delta}$ powders (x = 0, 0.05, 0.10, 0.15 and 0.30, noted as Sm0BCF, Sm5BCF, Sm10BCF, Sm15BCF and Sm30BCF respectively) were synthesized *via* a combined ethylenediaminetetraacetic (EDTA) and citric acid complexing method. Stoichiometric amounts of $Sm(NO_3)_3 \cdot 6H_2O$ (Alfa Aesar, 99.99%), $Ba(NO_3)_2$ (Alfa Aesar, 99.999%), $Co(NO_3)_2 \cdot 6H_2O$ (Alfa Aesar, 99.99%) and $Fe(NO_3)_3 \cdot 9H_2O$ (Alfa Aesar, 99.99%) served as raw materials for the necessary metal ions, while EDTA and citric acid played the role of complexing agents with the molar ratio of citric acid: EDTA: metal ions = 1.5: 1: 1. Ammonia was used to adjust the pH of the solution to ~8. After being mixed homogenously, the solution was dehydrated at 80 ^oC to form a gel, which was then burned on an electrical heater until it combusted to form a bouffant precursor powder. Subsequently, the precursors were ground, followed by calcining at 400 °C for 2 h to remove organic residues. Finally, the powders were heat-treated at 1000 °C for 6 h in air to achieve the desired phases.

4.2.2 Sample preparation

Rectangular bar of Sm10BCF was fabricated for electrical conductivity and electrical conductivity relaxation (ECR) test. Sm10BCF powder was ground with PVB binder (2 wt.%) and uniaxially pressed, then sintered at 1100 ^{o}C for 6 h. The surface of the sample bars was mechanically polished with sand-paper, followed by washing in an ultrasonic cleaner within ethanol. Four silver wires were attached at well-aligned different locations on the surface of the sample bars using Ag paste (Heraeus 2807).

The $Ce_{0.8}Sm_{0.2}O_{1.9}$ (SDC) electrolyte powder (tape cast grade, Fuel Cell Material, USA) was mixed and ground thoroughly with PVB binder (2 wt%) in ethanol. After completely drying, the electrolyte powder was then dry-pressed into pellets, which were then sintered at 1450 ^{o}C for 6 h to get dense SDC pellets. And then, the pellets were polished to remove the surfaces, followed by cleaning in the ultrasonic machine. Symmetrical cells with the configuration of $Sm_xBa_{1-x}Co_{0.8}Fe_{0.2}O_{3-\delta}$ | SDC | $Sm_xBa_{1-x}Co_{0.8}Fe_{0.2}O_{3-\delta}$ were fabricated for electrochemical impedance spectroscopy (EIS) measurements. The cathode slurry was prepared by mixing respective cathode powders with binder (α-terpineol solution of 6 wt. % ethylene cellulose) in a weight ratio of 2:1. The prepared slurry was then symmetrically screen-printed onto both sides of SDC electrolyte pellets followed by annealing at 1050 ^{o}C for 2 h in air. A thin layer of Ag paste was then painted onto the electrode surfaces and silver wires were attached onto the surfaces, which were served as current collector.

The anode-supported single cell Sm10BCF | SDC | NiO + SDC was fabricated by dry pressing and drop-coating process. The anode precursor powder NiO (fine grade, Fuel Cell Material, USA), SDC and starch (60:40:20 by weight ratio) anode powder were

mixed and ball-milled for 24 h with ethanol as the milling medium. After a drying step, the well mixed anode powder was mechanically pressed and pre-sintered at 1100 ^{o}C for 3 h to form the anode green pellets. SDC powder was used as the electrolyte precursor. 10 g SDC powder was ball-milled with 1g triethanolamine as dispersant, 0.5 g di-n-butyl phthalate and 0.5 g polyethylene glycol as plasticizers, 0.5 g polyvinyl butyral as binder and 87.5 g ethanol as solvent for 7 days to form a homogenous spinning slurry. The as prepared SDC electrolyte slurry (80 μL) was dropped onto the surface of the green anode pellets. And then the pellets were dried in air for 6 h before pre-sintered at 800 ^{o}C for 2 h. This process was repeated 2 times. Another 80 μL was dropped to the pre-sintered electrolyte surface to obtain sufficient electrolyte thickness. After drying, the cells were co-firing at 1450 ^{o}C for 6 h. Subsequently, the thickness of the anode was reduced to ~0.5 mm by grinding. Sm10BCF cathode slurry was then applied onto the electrolyte surface using the same procedure as described earlier followed by sintering at 1050 ^{o}C for 2 h. Ag paste was applied as a current collector on both the anode and cathode electrodes.

4.2.3 Characterization

The phase analysis were performed using X-ray diffraction (XRD, Rigaku) with Cu Kα (λ = 1.5406 Å) at room temperature with a step size of 0.02^{o} in the range of 10^{o} ≤ 2θ ≤ 90^{o}. The microscopic features of the cells were examined using scanning electron microscopy (SEM, Zeiss Ultra Plus FESEM, Germany). The morphology of Sm10BCF powder was characterized by Transmission electron microscopy (TEM) measurements (Hitachi H-9500 TEM with an accelerating voltage of 300 kV). To prepare samples for TEM measurements, Sm10BCF powder were diluted in ethanol and sonicated for 30 min to ensure homogeneous distribution of particles. Two drops of the suspension were

deposited onto a carbon-stabilized formvar copper grid and completely dried at room temperature prior to measurement.

The electrical conductivity of Sm10BCF bar sample was measured in air from 700 to 250 ^{o}C with an interval of 50 ^{o}C using a four-terminal DC method. The electrical conductivity of the sample was automatically recorded by a digital multimeter (Agilent 34401A) until it was stable. The electrical conductivity relaxation (ECR) measurement was used to determine the surface exchange coefficient (k*) and bulk diffusion coefficient (D*) over Sm10BCF sample. During the ECR test, the oxygen partial pressure in the surrounding atmosphere was abruptly changed from 0.21 to 0.1 atm. Various were controlled by adjusting the ratio of oxygen and nitrogen. The variation of the conductivity was recorded continuously with relaxation time till the sample reached equilibrium again. And ECR tools were applied for data fitting.[150]

Electrochemical impedance spectroscopy (EIS) of symmetrical cells with $Sm_xBa_{1-x}Co_{0.8}Fe_{0.2}O_{3-\delta}$ as electrode was performed with a Zahner IM6E electrochemical workstation in air and open circuit voltage (OCV) condition. The frequency was ranged from 10^6 to 0.1 Hz with a signal amplitude of 10 mV. EIS was conducted at 500 to 650 ^{o}C. Zview software is used to fit the EIS data. To further investigate the kinetic of Sm10BCF cathode, polarization resistances were measured at different oxygen partial pressure and different temperature. The symmetrical cell Sm_{10}BCF | SDC | Sm_{10}BCF was tested in air at 600 ^{o}C for ~200 h to evaluate the short-term stability of Sm10BCF as a cathode material. For fuel cell testing, single cells were sealed on alumina tubes by ceramic binder (Aremco products, inc. USA), and then dried at room temperature

overnight. I-V polarization curves were measured with 80 mL min^{-1} hydrogen as fuel and ambient air as oxidant over a temperature range from 550 to 650 ^oC.

4.3 Results and Discussion

4.3.1 Crystal structure

The phase formation of $Sm_xBa_{1-x}Co_{0.8}Fe_{0.2}O_{3-\delta}$ (x = 0, 0.05, 0.1, 0.15 and 0.3) was confirmed by XRD measurement, as shown in Figure 4.1. Upon doping Sm into A-site of $BaCo_{0.8}Fe_{0.2}O_{3-\delta}$, the crystal structure transferred obviously. The undoped sample is crystalized into a hexagonal phase $BaCoO_{2.6}$ and Fe_3O_4 as impurity, which is shown in Figure 4.2. Upon substitution of Ba by 5 mol% Sm, the diffraction peak pattern of Sm5BCF is identified as a hexagonal phase $BaCoO_{2.6}$, a simple perovskite phase with cubic symmetry and a minor phase of CoO, as shown in Figure 4.3. The appearance of the cubic phase can be explained by the substitution of Ba by Sm in A-site or/and the substitution of (Co, Fe) in the B-site, which can be denoted as $(Ba/Sm)(Co/Fe/Sm)O_{3-\delta}$. However, the exact composition of the simple perovskite is not clear at this stage. With increasing the Sm amount to 10 mol%, two phases are identified: one is a simple perovskite phase with cubic symmetry and the other is a layered perovskite phase $SmBa(Co/Fe)_2O_{5+\delta}$ with orthorhombic symmetry, which are shown in Figure 4.4. One can also notice that there is a very small amount of BaO (PDF#74-1228) around 28^o which is marked in Figure 4.4a. This result is also confirmed by Figure 4.4b which shows the magnified XRD patterns of Sm10BCF sample in the range of $2\theta = 30\text{-}60^o$ and the peaks corresponding to each phase. Upon increasing Sm amount to 15 mol%, a hexagonal phase is identified besides the simple perovskite and the layered perovskite which is shown in Figure 4.5a. Moreover, the relative amount of double perovskite

increased in Sm15BCF than that of Sm10BCF, and became even more when x = 0.30 for Sm30BCF as shown in Figure 4.5b.

The evolution of $Sm_xBa_{1-x}Co_{0.8}Fe_{0.2}O_{3-\delta}$ composition is complicated and might be explained as: The simple perovskite first appeared in x = 0.05 sample. Besides the existence of the simple perovskite, the layered perovskite $SmBa(Co/Fe)_2O_{5+\delta}$ appears when x = 0.1. The formation of the composite material is thermally stable. This also indicates that the formation energy of the simple perovskite is smaller than that of the layered perovskite, thus simple perovskite is firstly appeared. The $SmBa(Co/Fe)_2O_{5+\delta}$ can be understood as that a portion of Sm stays in the A-site of $Ba_{0.9}Co_{0.8}Fe_{0.2}O_{3-\delta}$. However, Sm cannot randomly distribute in the A-site with Ba together. The difference between the ionic radii of Ba^{2+} (r(XII) = 1.61 Å) and Sm^{3+} (r(XII) = 1.24 Å) induces a cationic ordering in alternating layers $BaO\text{-}(Co/Fe)O_2\text{-}SmO\text{-}(Co/Fe)O_2$ for layered perovskite.[89] Thus, when considering the composition of the simple perovskite ABO_3, it is reasonable to assume that it could be the B-site doped $Ba(Co/Fe/Sm)O_{3-\delta}$. In order to prove that Sm can embed in the B site of ABO_3 structure, we also synthesized $BaCo_{0.7}Fe_{0.2}Sm_{0.1}O_{3-\delta}$ which turns out to be cubic symmetry, which is shown in Figure 4.6. And if Sm went to the B-site, the simple perovskite would be A-site deficiency which was originated from the composition of the pristine material. Thus, the cubic phase simple perovskite might be the B-site doped Ba deficient ABO_3 perovskite other than the A-site doped simple perovskite. Therefore, the simple perovskite can be written as $Ba_{1-y}(Co/Fe/Sm)O_{3-\delta}$.

Now using Sm10BCF as an example, the exact composition of the phases is not clearly as mentioned above. However, a brief calculation may give some insight into the component of this nanocomposite material. Now we assume that $Sm_{0.10}Ba_{0.90}Co_{0.8}Fe_{0.2}O_{3-}$

$_{\delta}$ is consisted of only two phases: simple perovskite $Ba_{1-y}(Co/Fe/Sm)O_{3-\delta}$ and layered perovskite $SmBa(Co/Fe)_2O_{5+\delta}$. (This assumption is made based on the fact that the amount of the impurity BaO is very small) And the B site of simple perovskite (Co/Fe/Sm) is fully occupied which is 100 mol% and the ratio of Co/Fe on the B site is same with the original ratio which is 8/2. In order to simplified the calculation, $Sm_{0.10}Ba_{0.90}Co_{0.8}Fe_{0.2}O_{3-\delta}$ is written as $Sm_{0.10}Ba_{0.90}MO_{3-\delta}$ where M represents the Co/Fe in the B-site. Thus, the constitute of $Sm_{0.1}Ba_{0.9}MO_{3-\delta}$ can be expressed as:

$$1\ mol\ Sm_{0.10}Ba_{0.90}MO_{3-\delta} \rightarrow$$

$$m\ mol\ Ba_{1-y}(M_{1-z}Sm_z)O_{3-\delta} + n\ mol\ SmBaM_2O_{5+\delta} \quad (4\text{-}1)$$

From the equation (1), we can obtain equations based on the content of Ba, Sm and M:

$$\mathrm{m} * (1 - \mathrm{y}) + \mathrm{n} = 0.90 \quad (4\text{-}2)$$

$$\mathrm{m} * \mathrm{z} + \mathrm{n} = 0.10 \quad (4\text{-}3)$$

$$\mathrm{m} * (1 - \mathrm{z}) + 2\mathrm{n} = 1 \quad (4\text{-}4)$$

To figure out the numbers, another equation is still needed. Therefore, Rietveld refinement was performed with XRD patterns of Sm10BCF by Fullprof. Based on the analysis, the cubic *Pm-3m* space group and the orthorhombic *Pmmm* space group were used to fit the experimental XRD data and the refinement results is shown in Figure 4.7. According to the results of Rietveld refinement, Sm10BCF is composed of a main phase of cubic simple perovskite (86.87 wt%) and a minor orthorhombic layered perovskite phase (13.13 wt%). The fitting parameters of refinement are $\chi 2$ = 4.88, Rwp = 13.3%, Rp = 19.5%, and Rexp = 6.04%. The R-factors is a little bit high which may be caused by the assumptions made above such as the impurity in Sm10BCF sample and uncertain composition in the B-site. But a good agreement was achieved between the XRD profile

and the fitting results graphically as shown in Figure 4.7. Notice is needed here that the refinement may not very accurate but is enough for our rough estimate of Sm10BCF composition. Thus, based on the weight ratio of the two phases, equation (5) can be written as:

$$\frac{m*M_{mass,cubic}}{n*M_{mass,orthorhombic}} = \frac{86.87}{13.13} \tag{4-5}$$

Where M_{mass} is the molar mass of the compounds. Combining equations 4-2, 4-3, 4-4 and 4-5 yields the solutions:

$$m = 0.902,\ n = 0.066,\ y = 0.075,\ z = 0.038$$

Thus, we can get the components of the nanocomposite Sm10BCF which are 0.902 mol $Ba_{0.925}(Co/Fe)_{0.962}Sm_{0.038}O_{3-\delta}$ and 0.066 mol $SmBa(Co/Fe)_2O_{5+\delta}$. It should be noticed here that we have several assumptions applied when processing the calculation and the ratio between Co and Fe is not clear here. And the composition above may not be accurate constitute in the composition. However, we can still get useful information from the analysis that the simple perovskite is A-site deficiency and the brief ratio of the two phases. And the existence of the two phases can also be seen in high-resolution TEM image of Sm10BCF powder as shown in Figure 4.8. In order to verify the analysis above, the distribution of the different phases were investigated by energy-dispersive X-ray (EDX). The Sm10BCF pellet was characterized by SEM. Figure 4.9 shows the surface and cross-sectional SEM images of bulk Sm10BCF sintered at 1100 ºC in air for 6 h. It exhibits two kinds of particles with different sizes and clear grain boundaries between these two phases on the bulk surface as shown in Figure 4.9a. While in the internal of the bulk sample, two phases are also clearly identified as marked in Figure 4.9b. The selected region EDX results also suggest the different composition of the particles with different

sizes as shown in Figure 4.10. The quantitative results of EDX indicates that the smaller particle contains more Sm in the composition than the larger one. The surface and bulk EDX mapping of Sm10BCF pellet was also conducted. As presented in Figure 4.11, two phases with different Sm content can also be clearly identified. Based on the EDX and XRD results of Sm10BCF, the larger particle is the major phase which might be attributed to the simple perovskite and the smaller particle is the layered perovskite with more Sm content. When the amount of Sm continues increasing to 15 or 30 mol%, the amount of $SmBa(Co/Fe)_2O_{5+\delta}$ also increases while another hexagonal phase appears. Even though the composition of simple perovskite in Sm5BCF, Sm15BCF and Sm30BCF may not be same with Sm10BCF, they are still composite materials with a cubic phase simple perovskite, an orthorhombic phase layered perovskite and a hexagonal phase perovskite.

4.3.2 ORR activity

The ORR activity of the SmxBCF nanocomposite was measured by two-probe electrode impedance using SmxBCF | SDC| SmxBCF symmetrical cells at low temperature range. Figure 4.12 shows the of microstructures of the SmxBCF symmetrical cells that sintered at 1050 ^oC for 2 h. The SmxBCF electrode shows similar morphology with sufficient porosity. The cathodes exhibit good inner-connectivity and demonstrate intimate contact with SDC electrolyte. Typical EIS of SmxBCF electrodes at 650 ^oC is shown in Figure 4.13a and b shows the frequency response of the imaginary part of the impedance spectra. An equivalent circuit model $L - R_o - (R_h Q_h) - (R_l Q_l)$ (inset in Figure 4.13a) was used to fit the EIS data and spectral fitting results are also shown in the same figure. In this model, L is the inductance of the circuit caused by the electrical

equipment and lead wires, R_o represents ohmic resistance induced by electrolyte and electrode backbone as well as current collecting wires. R_i and Q_i are the resistance and constant phase capacitance of high (h) and low (l) frequency processes, respectively. The polarization resistance of electrode R_p is then obtained by adding R_h and R_l together.

Arrhenius plots of the R_p of the SmxBCF electrodes at 500-650 ^oC and corresponding activation energy (E_a) are presented in Figure 4.14. Attractive R_p values of 0.075, 0.151, 0.366, 0.993 Ω cm^2 were achieved at 650, 600, 550 and 500 ^oC, respectively, for Sm10BCF in air, which is the lowest among SmxBCF nanocomposite cathode, suggesting that the Sm10BCF was the optimal chemical composition in $Sm_xBa_{1-x}Co_{0.8}Fe_{0.2}O_{3-\delta}$ (x = 0, 0.05, 0.1, 0.15 and 0.3) series composite electrodes. Based on the results of XRD, Sm10BCF consisted of a major cubic phase simple perovskite and a minor phase of layered-perovskite, which both possess excellent catalytic activity towards ORR. The self-assembled nanocomposite Sm10BCF has good contact in nanodomain and increased active sites for electrochemical reaction. However, for the other three electrodes, the presence of the hexagonal phase may lead to lower electrochemical activity since the formation energy of an oxygen vacancy in the hexagonal lattice is much higher than that in the cubic phase.[56]

The surface of fresh Sm10BCF cathode before test was carefully checked by SEM as shown in Figure 4.15. Many nanoparticles with an average diameter of 30-40 nm were adhered on the grain surface of the cathode homogeneously. EDX scanning was conducted to examine the composition of the surface as shown in Figure 4.16. Based on the EDX results, it is reasonable to assume that the bulk phase is the simple perovskite. The composition shows no obvious difference between the nanoparticles and bulk phase.

However, we also notice that compared with bulk phase, the ratio of Ba/(Co+Fe) in the nanoparticles possesses a lower value and closer to 1, which suggests that the nanoparticles might be a Co-rich phase. As mentioned above, the bulk simple perovskite is an A-site cation deficiency phase. At the atomic scale, the presence of A-vacancies is thermodynamically instable, resulting in spontaneous B-species exsolution which can revert the perovskite to a thermodynamically stable stoichiometric one with A/B = 1. Consequently, there is a strong driving force that pulls B-site atoms to grow outward from the host lattice to minimize unsteadiness of the perovskite.[151] The similar exsolving phenomenon has been found in A-site cation deficient $PrBa_{0.94}Co_2O_{5+\delta}$, in which $PrCoO_3$ nanoparticles with the A/B=1 exsolved on the surface of the perovskite scaffold.[152] Since the composition of the nanoparticles is similar with the bulk phase, it is reasonable to assume that the nanoparticles are also electrocatalytically active. The high surface area of nanoparticles provides the rich active sites towards ORR, leading to better kinetic property. The Sm10BCF cathode surface of the symmetrical cell after the EIS measurement was also checked by SEM, which shows no obvious change of morphology as shown in Figure 4.17. We also notice that Sm5BCF also possesses lower polarization resistances which are 0.085, 0.174, 0.408, 1.163 Ω cm^2 at 650, 600, 550 and 500 ^oC, respectively. This could be explained by the extra CoO phase within Sm5BCF composite cathode as shown in Figure 4.3.

Notably, the activation energy of Sm10BCF is 103.32 kJ mol^{-1}, which is similar with that of Sm5BCF and Sm15BCF but lower than that of Sm30BCF. Compared with most developed BSCF cathode material (116 kJ mol^{-1})[21], Sm10BCF possesses a lower activation energy which means a lower chemical barrier for oxygen reduction,

subsequently a higher electro-catalytic activity at reduced temperature. So we hypothesize that Sm10BCF should also be an excellent cathode candidates for even low temperature SOFCs at even lower temperatures.

4.3.3 Electrical conductivity of Sm10BCF nanocomposite material

Since Sm10BCF shows the lowest polarization resistance among SmxBCF series nanocomposite, more detailed investigates were carried out on Sm10BCF. The electrical conductivity of Sm10BCF was measure via the four-terminal DC technique. As shown in Figure 4.9, the bulk sample sintered at 1100 ^{o}C in air for 6 h shows sufficient density for electrical conductivity measurement. Besides, the bulk sample shows a trans-granular fracture feature, indicating good grain-boundary contact and strong grain-boundary strength between the two phases. Temperature dependence of electrical conductivity of Sm10BCF sample in air is shown in Figure 4.18. The electrical conductivity increases monotonously with increasing of the temperature, suggesting semiconductor behavior. The electrical conductivity of Sm10BCF nanocomposite reaches 93.24 S cm^{-1} at 600 ^{o}C, which is close to requirement of 100 S cm^{-1} at 600 ^{o}C for the good cathodes of LT-SOFCs. And as mentioned before, this value is higher than that of some $BaCoO_3$-cathode material for LT-SOFCs reported in the literature. The relatively low electrical conductivity may induce an important drawback which could result in a dramatic increase of ohmic resistance at lower temperatures. The increase of the electrical conductivity of Sm10BCF nanocomposite can be attributed to the self-assembled layered perovskite $SmBa(Co/Fe)_2O_{5+\delta}$ which possesses high electrical conductivity.

For a cathode material, the bulk diffusion and surface exchange kinetics are closely related to the electrochemical performance. Here, oxygen bulk diffusion

coefficient (D*) and surface exchange coefficient (k*) were identified using the electrical conductivity relaxation method. The electrical conductivity were recorded with instant change of oxygen partial pressure from 0.21 to 0.1 atm. Figure 4.19 depicts the Arrhenius plots of D* and k* for Sm10BCF nanocomposite. Both D* and k* increase with increasing temperature, indicating higher activity at elevated temperatures. Since a long period of time is needed for reaching equilibrium when measuring temperature decreases, the extrapolating of the data can give more insights into the bulk diffusion and surface exchange of Sm10BCF nanocomposite at lower temperatures. The D* and k*values of 1.25×10^{-5} cm^2 s^{-1} and 2.66×10^{-4} cm s^{-1} are acquired at 600 ^oC for Sm10BCF, which is of the same order of magnitude with those of BSCF[153] (2.5×10^{-5} cm^2 s^{-1} for D* and 2.7×10^{-4} cm s^{-1} for k* at 600 ^oC).

4.3.4 Oxygen partial pressure dependent electrochemical kinetics

The multistep reactions involved in the cathode process are strongly dependent on oxygen pressures applied on the electrode. In order to get more insight into intrinsic ORR process of SmxBCF cathode, polarization resistance of Sm10BCF cathode with the configuration of Sm10BCF | SDC| Sm10BCF were measured in different oxygen partial pressures at different temperatures. In general, the relationship between the polarization resistance (R_p) and oxygen partial pressure (P_{O_2}) is shown as follows,

$$R_i = k(P_{O_2})^{-m}, i = h, l \tag{4-6}$$

where, R_i is polarization resistance of high or low frequency process, k a constant, P_{O_2} oxygen partial pressure, m is reaction order and quantitatively related to rate-limiting steps as follows[154]:

- $m = 1$:

$$O_{2,g} + Sm10BCF(s) \leftrightarrow O_{2,ads}(Sm10BCF) \quad (4\text{-}7)$$

Molecular oxygen adsorption process onto porous electrode surface.

- $m = 0.5$

$$O_{2,ads}(Sm10BCF) \leftrightarrow 2O_{ads}(Sm10BCF) \quad (4\text{-}8)$$

Dissociation of adsorbed molecular oxygen into atomic oxygen.

- $m = 0.25$

$$O_{ads}(Sm10BCF) + 2e^- + V_O^{\cdot\cdot} \leftrightarrow O_O^{\times} + Sm10BCF(s) \quad (4\text{-}9)$$

Charge transfer reaction for oxygen anion formation and incorporation into oxygen vacancy.

- $m = 0$

$$\mathrm{O}_{TPB}^{2-} + V_O^{\cdot\cdot}(\text{Sm10BCF bulk}, Sm10BCF/SDC\ interface) \leftrightarrow O_O^{\times} \quad (4\text{-}10)$$

Oxygen ion transfer within the bulk electrode and/or through the electrolyte/electrode interface.

The oxygen partial pressure P_{O_2} dependence of R_p for Sm10BCF nanocomposite cathode at different temperature is show in Figure 4.20. The slope m can be calculated from the linear variation of the P_{O_2} dependence. For the high frequency process, the m values are 0.06, 0.03, 0.08 and 0.05 for 650, 600, 550 and 500^o C, respectively, which are close to 0. This result indicates that the high frequency process is independent of the oxygen partial pressure, which is mainly associated with oxygen ion transfer within the bulk electrode and/or through the electrolyte/electrode interface. 0.32, 0.29, 0.30 and 0.29 P_{O_2} dependency were observed at different temperatures for low temperature process, which is close to the theoretical value 0.25. Thus, the low frequency arc could be related to charge transfer process. With regard to the results in Figure 4.20, it is also observed

that R_l is larger than R_h in the whole range of oxygen partial pressure at different temperatures. Therefore, charge transfer process is the major rate-limiting step for Sm10BCF cathode.

4.3.5 Stability test

The stability of a cathode material is critical for practical application for SOFCs. In order to gather more information on the Sm10BCF nanocomposite cathode, short-term stability of Sm10BCF was studied at 600 ^{o}C in air for ~200 h with a symmetrical cell Sm10BCF | SDC | Sm10BCF. EIS was performed periodically during the test. Figure 4.21 shows the time history of polarization resistance. It can be seen that R_p increases in the first 49 hours, and gradually reaches a stable state. R_p is 0.158 Ω cm^2 at the 0th hour, while it reaches 0.181 at 49th hour and 0.189 at the end of the test which is 192th hour. The R_p increasing rate of Sm10BCF nanocomposite is 4.69×10^{-4} Ω cm^2/h during the first 49 h, 5.59×10^{-5} Ω cm^2/h during the following 143 h. After the first 50 h, the Sm10BCF electrode remains quite stable.

Since the polarization resistance of Sm10BCF electrode can be separated into two processes and linked to specific ORR steps, through which the mechanism of the performance degradation might be identified. Figure 4.22a and b shows the time history of high (R_h) and low (R_l) frequency polarization resistance, respectively. R_h is relatively stable during the test. Since the high frequency polarization is related to the oxygen ion transfer within the bulk electrode and/or through the electrolyte/electrode interface, it is reasonable to assume that the structure and state within the electrode and electrolyte/electrode interface is quite stable during the test. For the low frequency polarization, it follows the same trend with the overall polarization resistance which

increases in the first 49 h and then reaches a stable state in the following testing period. As mentioned above, the low frequency process is closely related to the charge transfer process. Certainly, the charge transfer process is the formation of oxygen anion and incorporation into oxygen vacancies, thus highly related to the surface oxygen vacancy distribution. The increase of the R_h in the first 49 hours might be induced by the nanoparticles that decorated on the electrode surface. When testing, the fresh nanoparticles would go through a process of reorganization and aging which could in turn affect the oxygen vacancy distribution. The detailed analysis will be discussed later. And on the other hand, the segregation of inert cation Ba^{2+} may also degrade electrode performance.[95] However, the degradation in the Sm10BCF nanocomposite cathode is very limited and R_p remains stable after 49 hours adjustment.

4.3.6 Single-cell performance

Fuel cell test offers further verification of the electrochemical performance of Sm10BCF nanocomposite as cathode for LT-SOFCs under real condition. The test performed on an anode supported cell with Ni+SDC anode, SDC electrolyte and Sm10BCF nanocomposite cathode. *I-V* and *I-P* curves are presented in Figure 4.23a, while Figure 4.23b shows the corresponding polarization resistance at OCV condition. The single cell with Sm10BCF cathode delivered an attractive peak power density of 1271, 965, 572 mW cm^{-2} at 650, 600 and 550 ^{o}C, respectively. The morphology of the single cell after electrochemical measurement is shown in Figure 4.24. The cathode and anode well adhered to the electrolyte and shows uniform porosity. The electrolyte is dense which is ~10 μm thick. The electrochemical performance of fuel cell can be affected by various factors, such as contact resistance, electrolyte resistance, and so on.

Even better electrochemical performance can be expected to be achieved by optimization the process of electrolyte fabrication to increase OCV or adjusting sintering temperatures. Furthermore, the fuel cell with Sm10BCF cathode displayed a robust operational stability at a high current density of 600 mA cm^{-2} over 330 h at 600 ^{o}C, as shown in Figure 4.25. The Sm10BCF cathode surfaces after the stability test with the symmetrical cell and single cell are further characterized by SEM and shown in Figure 4.26. The nanoparticles on both Sm10BCF cathode surfaces have larger sizes than the fresh cathode, which change from 30-40 nm to ~100 nm after the stability tests. It is also noticed that more nanoparticles are appeared on the grainboundary. Based on EDX scanning, the nanoparticles attached on the surface and grainboundary are Co-rich phase as shown in Figure 4.27 and Figure 4.28. For the symmertical cell stability test, the cathode is mainly affected by thermal effect. While for single cell test, both the thermal effect and current driving are impact factors for cathode. As mentioned above, the simple perovskite in Sm10BCF is an A-site cation deficient oxide. The strong driving force induced by the thermodynamic and electrical effect act as significant driving forces to facilitate the exsolution of B-site element from their parent perovskite oxides. Thus, the Co content of the nanoparticles become more pronounced compared with the fresh one or the one after simple EIS measurement. On the other hand, nanoparticles have high surface energy. Therefore, under the long-term thermal treatment and continuous current applying, the nanoparticles are easily aggregated and grown to a bigger size. The Co-rich nanoparticles might enhance the ORR activity of the cathode, while the aggregation of the nanoparticles could affect the stability of the cathode. However, both the symmetrical cell and single cell exhibit excellent durability performance. The favorable cell performance

and stability test suggest that Sm10BCF holds great potential as an ORR electrocatalyst for application in the LT-SOFCs field.

4.4 Conclusion

A new series of $Sm_xBa_{1-x}Co_{0.8}Fe_{0.2}O_{3-\delta}$ material (x = 0, 0.05, 0.10, 0.15 and 0.30) was synthesized and characterized systematically as cathode for low temperature SOFCs. The $Sm_xBa_{1-x}Co_{0.8}Fe_{0.2}O_{3-\delta}$ nanocomposite materials are consisted of multiple phases. The formation of the nanocomposite is a thermally induced self-assembled process. The constitute in the nanocomposites adjusts with changing the different ratio between Sm and Ba. Among them, a hexagonal phase that less favorable towards ORR presents in the x = 0, 0.05, 0.15 and 0.30 powders except for the x = 0.10 sample. The $Sm_{0.10}Ba_{0.90}Co_{0.8}Fe_{0.2}O_{3-\delta}$ nanocomposite is composed of a major cubic phase of B-site doped Ba deficient ABO_3 simple perovskite, and a layered perovskite with orthorhombic symmetry. As to ORR activity, the combination of the two phases delivers excellent kinetic property and electrical property. At the same time, the self-assembled method also induces nanoparticles on the cathode surface, which is thermally favorable. The two phases are intimately mixed in nanodomain. The $Sm_{0.10}Ba_{0.90}Co_{0.8}Fe_{0.2}O_{3-\delta}$ nanocomposite shows affordable electrical conductivity, excellent bulk diffusion and surface exchange properties. Attractive polarization resistances are obtained for the $Sm_{0.10}Ba_{0.90}Co_{0.8}Fe_{0.2}O_{3-\delta}$ nanocomposite at low temperatures. The performance of the symmetrical cell shows degradation in the first 49 h in a 200 h short-term stability test which may be caused by the stabilization of the surface decorated nanoparticles. Under the real condition measurement, a high peak powder density of 1271 mW cm^{-2} at 650 ^oC is achieved with an anode-supported single cell, which also exhibits excellent stability

during ~330 h operation under a constant current density of 600 mA cm^{-2} at 600 ^{o}C. This research provides a new type of composite cathode material which shows promising features that may applied in low temperature SOFCs.

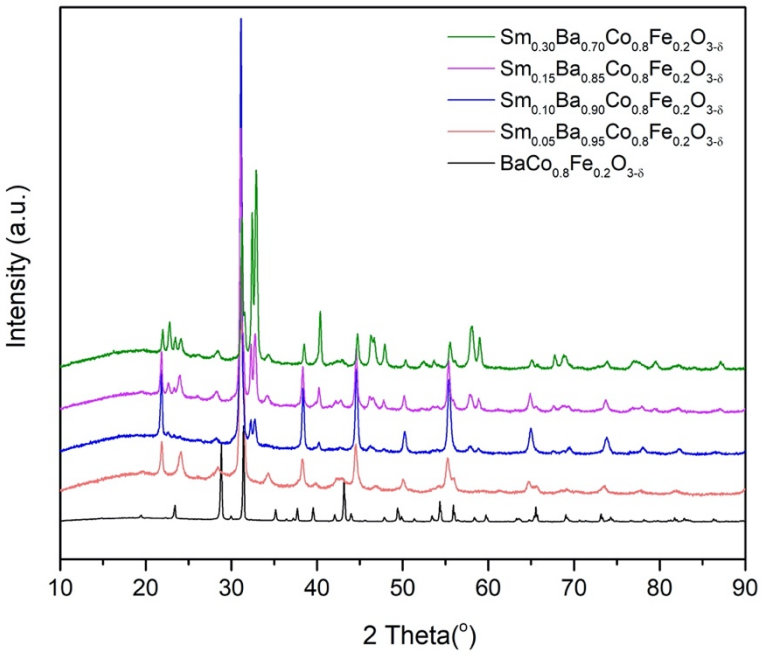

Figure 4.1 XRD patterns of $Sm_xBa_{1-x}Co_{0.8}Fe_{0.2}O_{3-\delta}$ (x = 0, 0.05, 0.1, 0.15 and 0.3) powders calcined at 1000 °C in air for 6 h.

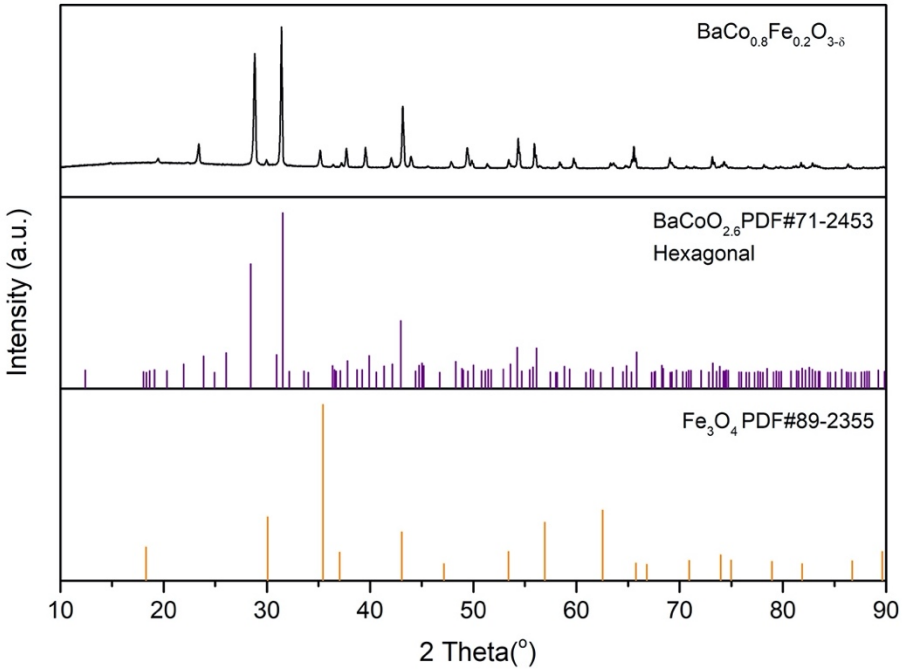

Figure 4.2 XRD pattern of $BaCo_{0.8}Fe_{0.2}O_{3-\delta}$ powders calcined at 1000 °C in air for 6 h; peak positions of hexagonal phase $BaCoO_{2.6}$ and Fe_3O_4.

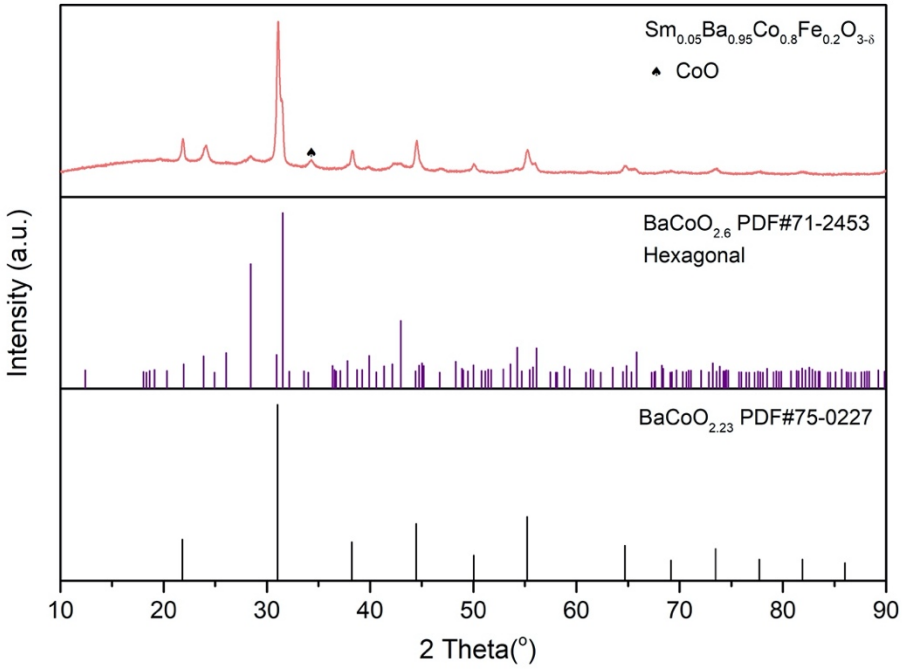

Figure 4.3 XRD pattern of $Sm_{0.05}Ba_{0.95}Co_{0.8}Fe_{0.2}O_{3-\delta}$ powders calcined at 1000 °C in air for 6 h; peak positions of hexagonal phase $BaCoO_{2.6}$, cubic phase $BaCoO_{2.23}$ and CoO.

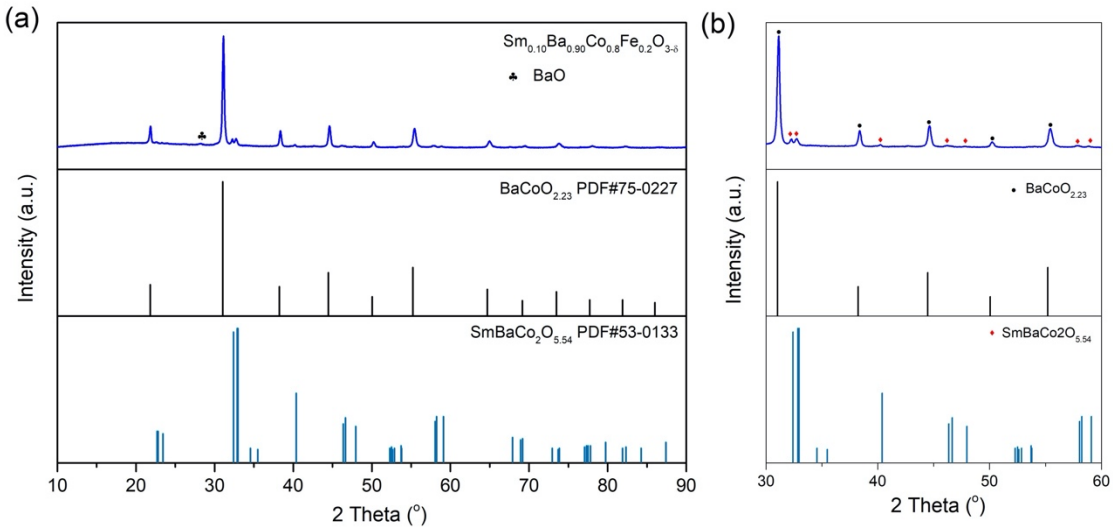

Figure 4.4 XRD pattern of $Sm_{0.10}Ba_{0.90}Co_{0.8}Fe_{0.2}O_{3-\delta}$ powder calcined at 1000 ^{o}C in air for 6 h; peak positions of cubic phase $BaCoO_{2.23}$ and orthorhombic phase $SmBaCo_2O_{5.54}$ (a); magnified pattern of 2θ = 30-60^{o}.

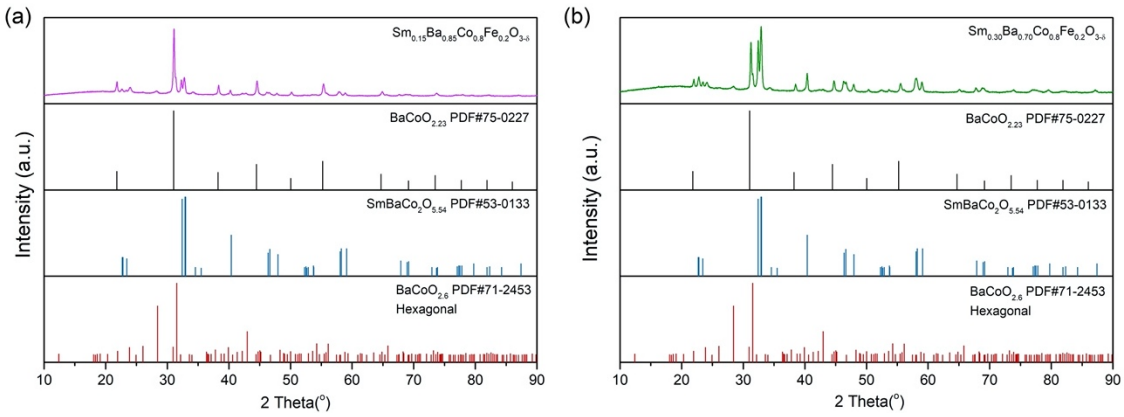

Figure 4.5 XRD pattern of $Sm_{0.15}Ba_{0.85}Co_{0.8}Fe_{0.2}O_{3-\delta}$ powder calcined at 1000 °C in air for 6 h (a) and $Sm_{0.30}Ba_{0.70}Co_{0.8}Fe_{0.2}O_{3-\delta}$ (b); peak positions of cubic phase $BaCoO_{2.23}$, orthorhombic phase $SmBaCo_2O_{5.54}$ and hexagonal phase $BaCoO_{2.6}$.

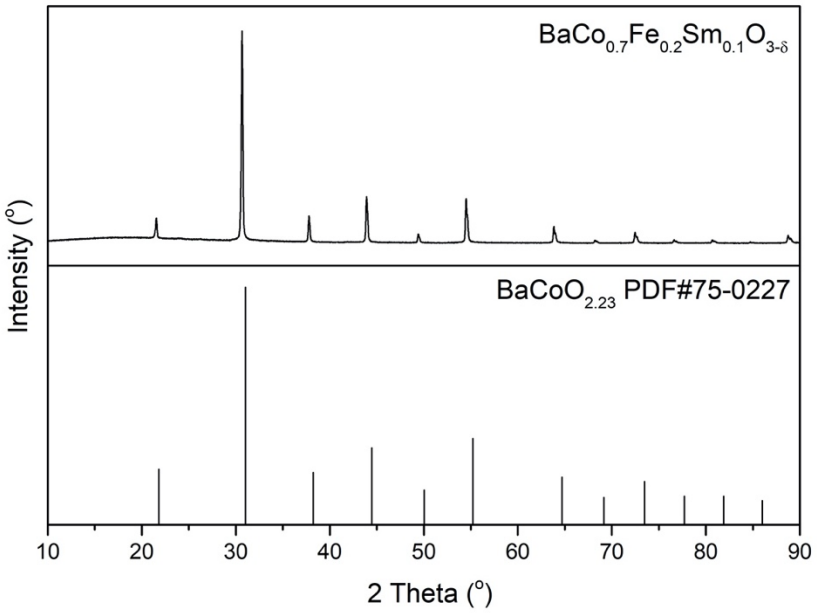

Figure 4.6 XRD pattern of $BaCo_{0.7}Fe_{0.2}Sm_{0.1}O_{3-\delta}$ powder calcined at 1000 °C in air for 6 h.

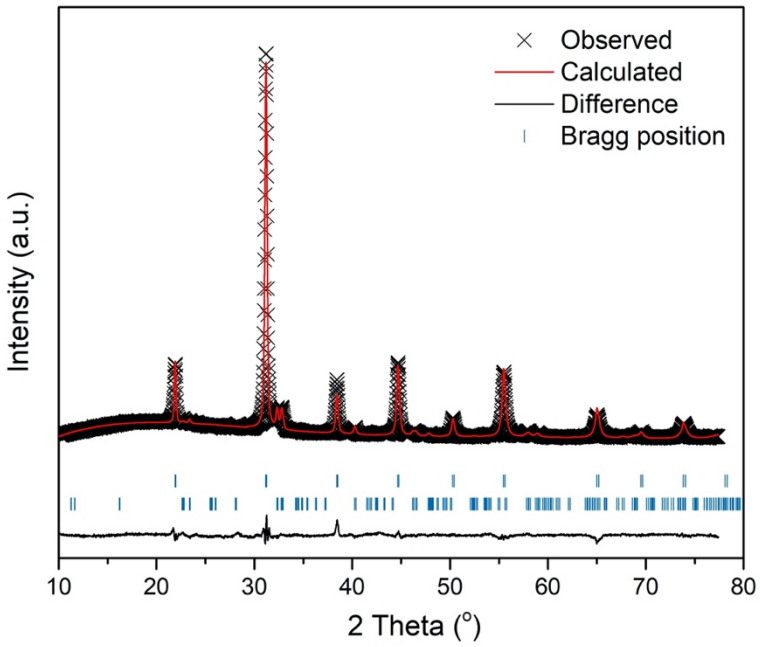

Figure 4.7 Refined XRD profiles of $Sm_{0.10}Ba_{0.90}Co_{0.8}Fe_{0.2}O_{3-\delta}$ powder.

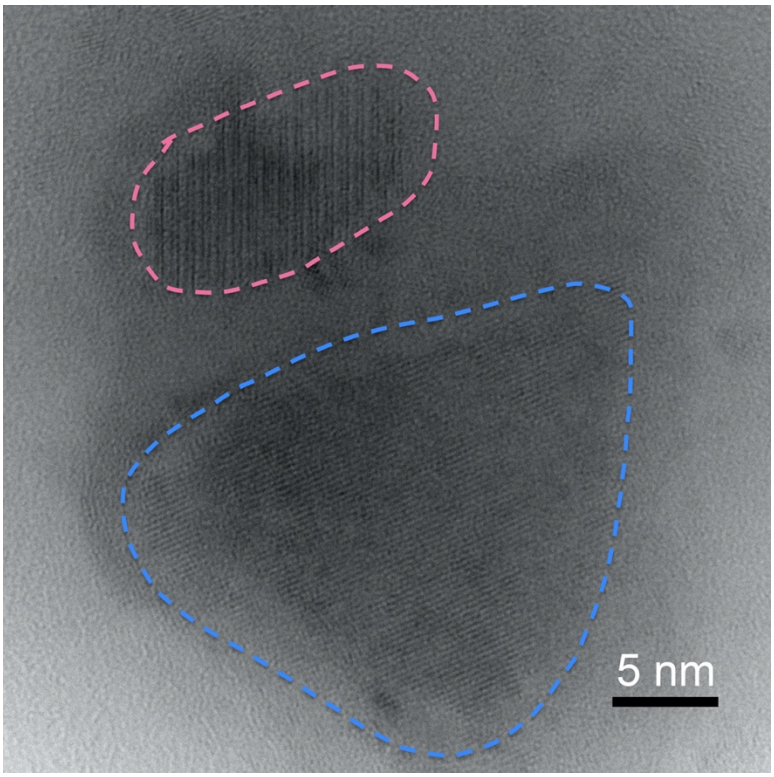

Figure 4.8 High-resolution TEM image of $Sm_{0.10}Ba_{0.90}Co_{0.8}Fe_{0.2}O_{3-\delta}$ powder.

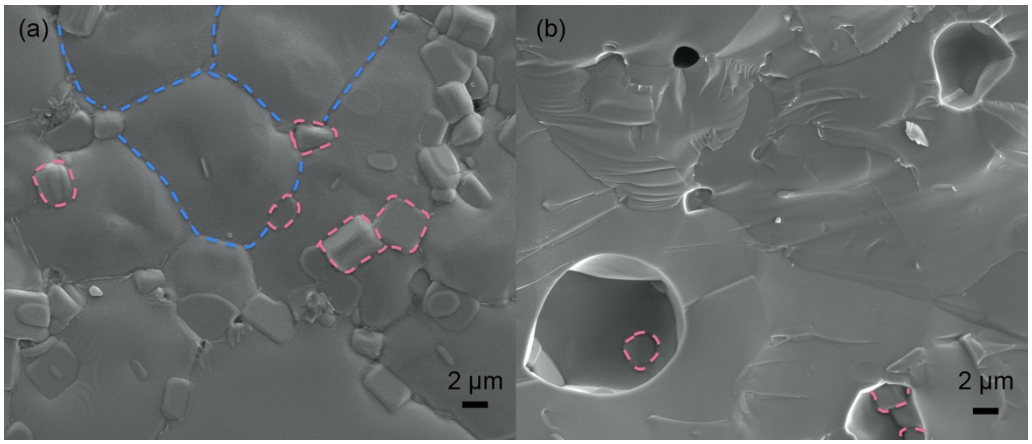

Figure 4.9 Surface (a) and cross-sectional (b) SEM images of bulk Sm10BCF sintered at 1100 ºC in air for 6 h.

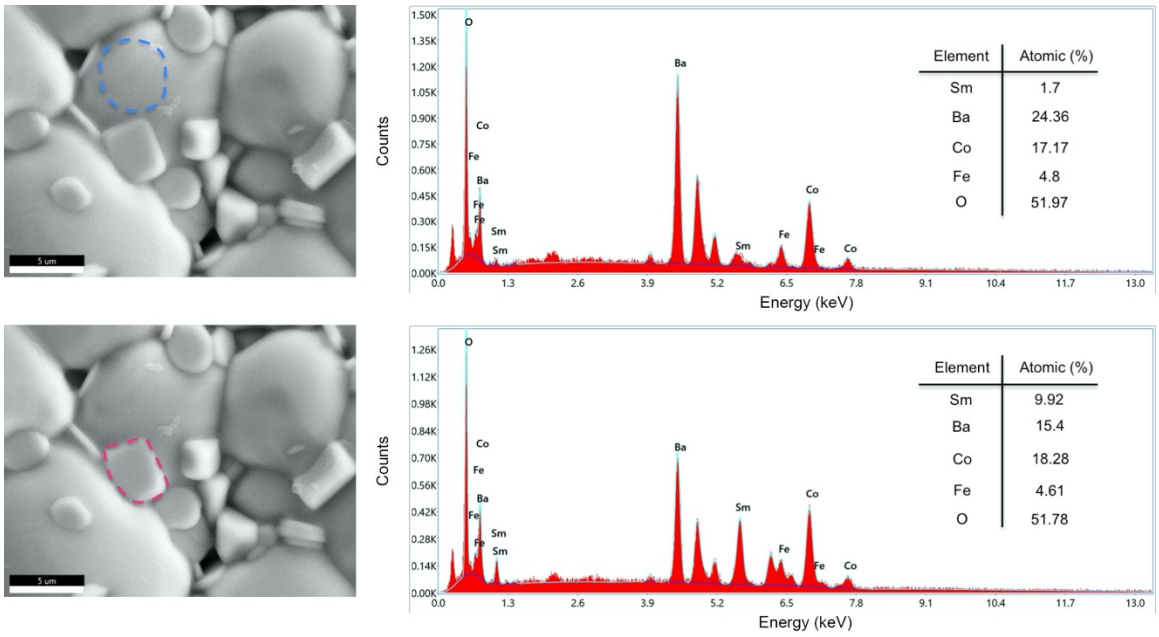

Figure 4.10 EDX scanning results of Sm10BCF pellet surface.

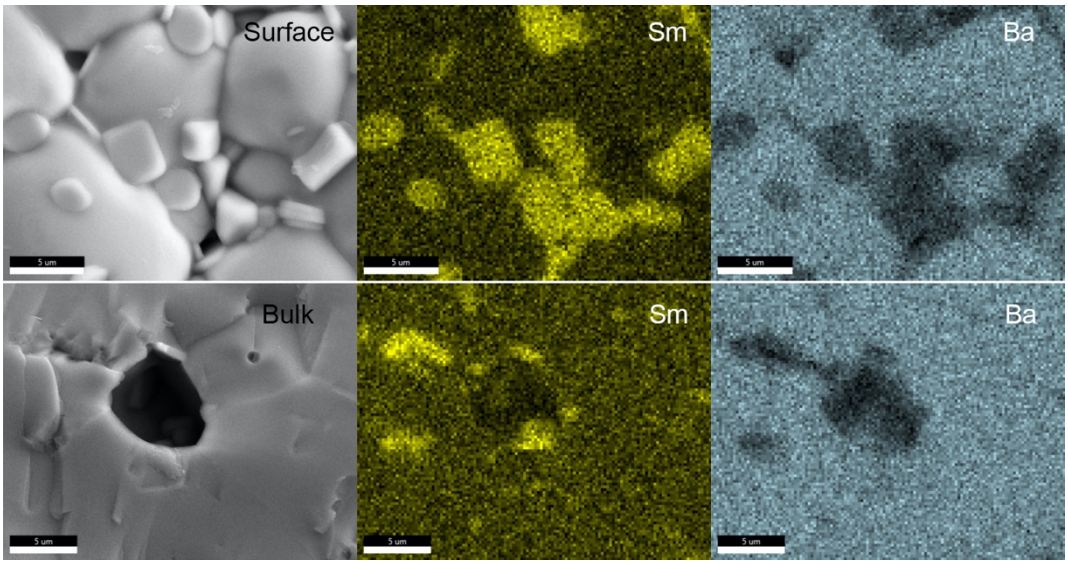

Figure 4.11 EDX mapping of Sm10BCF pellet surface and bulk.

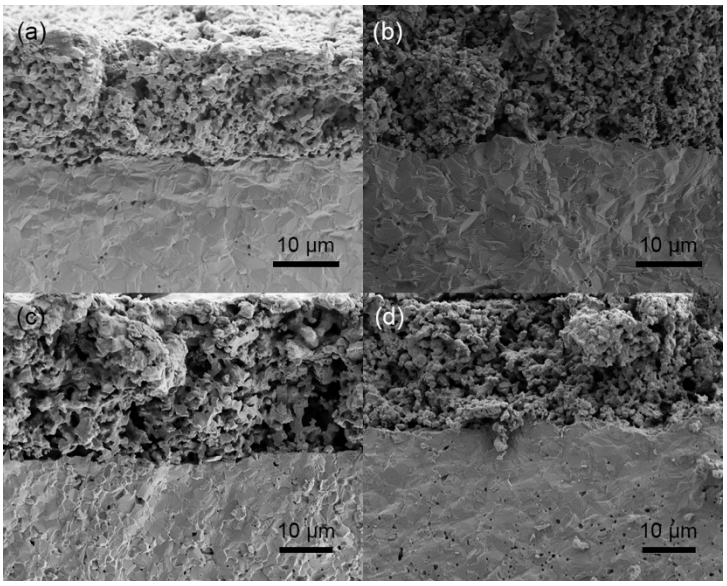

Figure 4.12 Cross-sectional SEM image of symmetrical cell with $Sm_xBa_{1-x}Co_{0.8}Fe_{0.2}O_{3-\delta}$ electrodes: (a) Sm5BCF, (b) Sm10BCF, (c) Sm15BCF and (d) Sm30BCF.

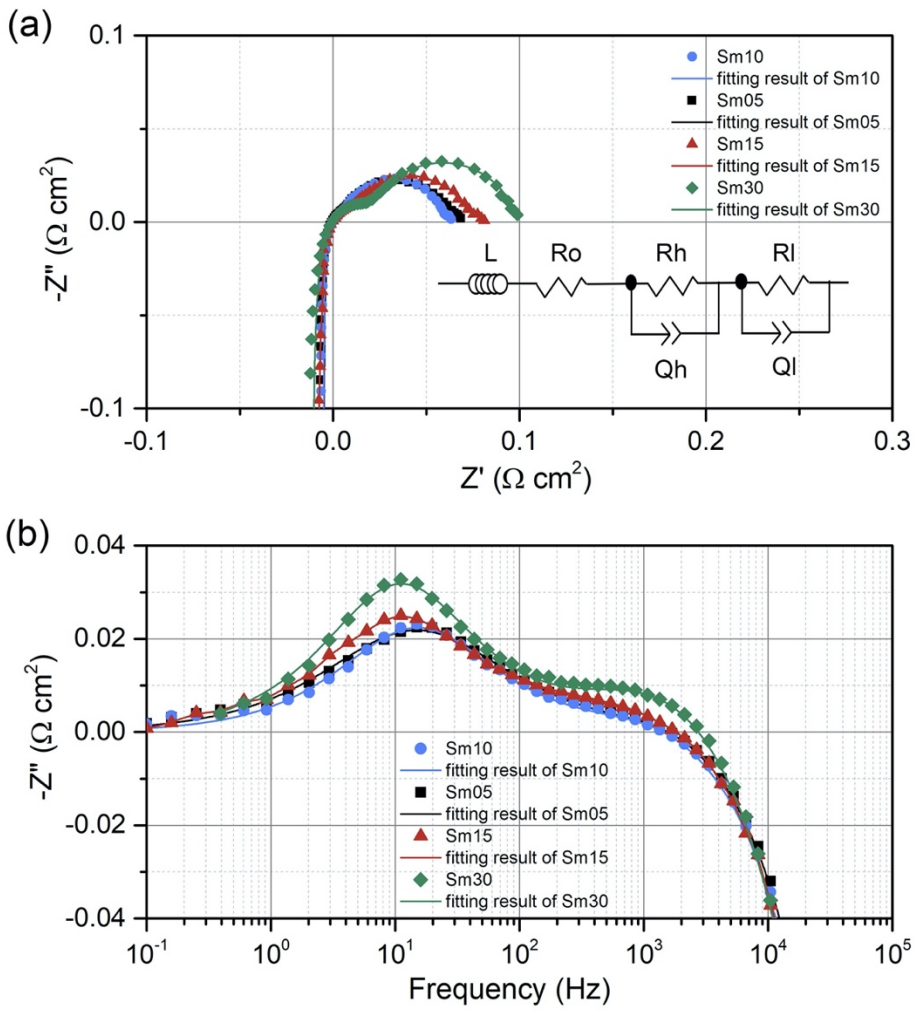

Figure 4.13 Typical Nyquist (a) and Bode (b) plots of symmetrical cells with SmxBCF electrodes measured at 650 °C in air. The inset is an equivalent circuit model used for curve fitting.

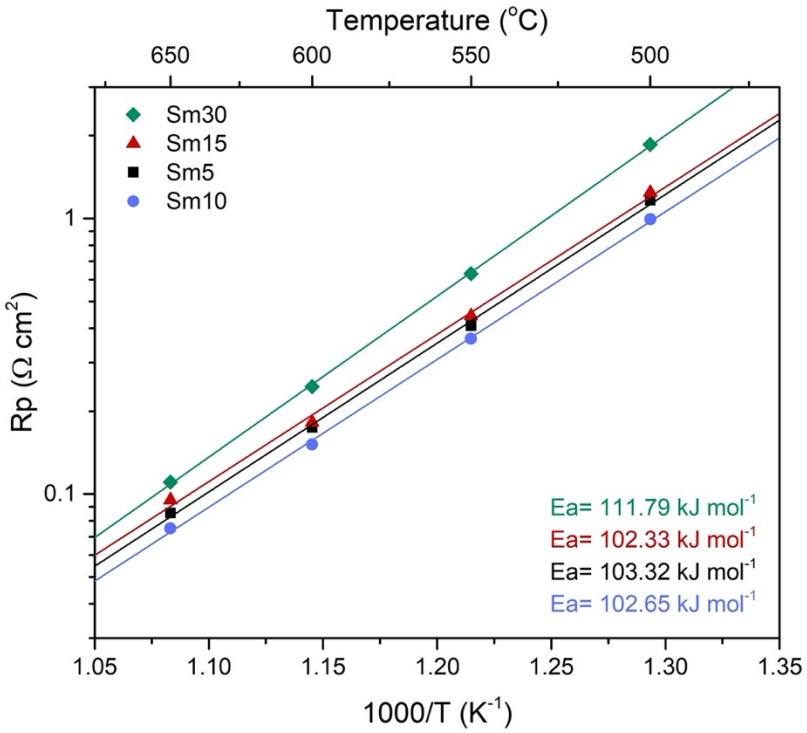

Figure 4.14 Polarization resistances vs. 1000/T of Sm10BCF electrodes measured in air from 500 to 650 °C.

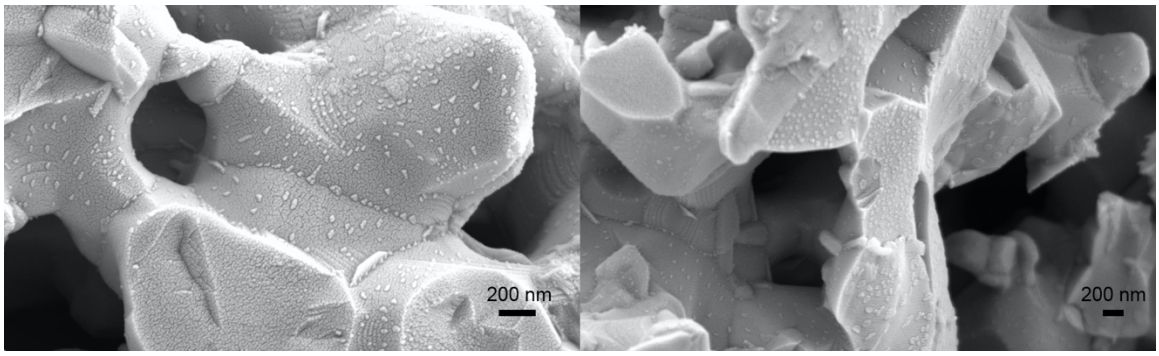

Figure 4.15 SEM images of Sm10BCF electrodes calcined at 1050 ^{o}C in air for 2 h.

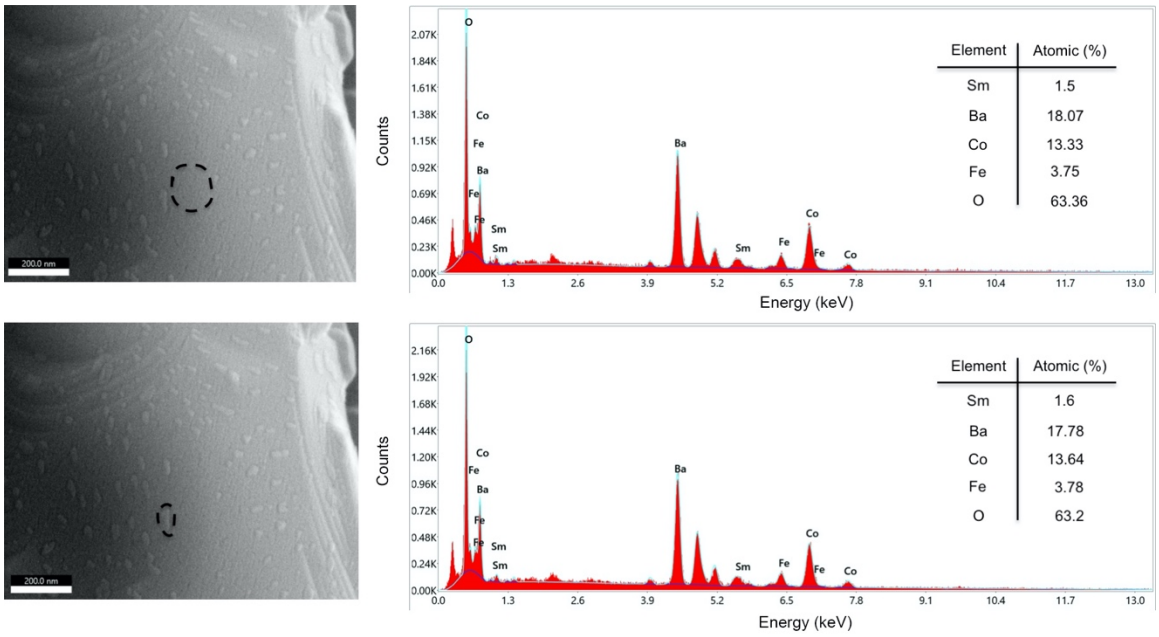

Figure 4.16 EDX scanning results of Sm10BCF electrode before EIS measurement.

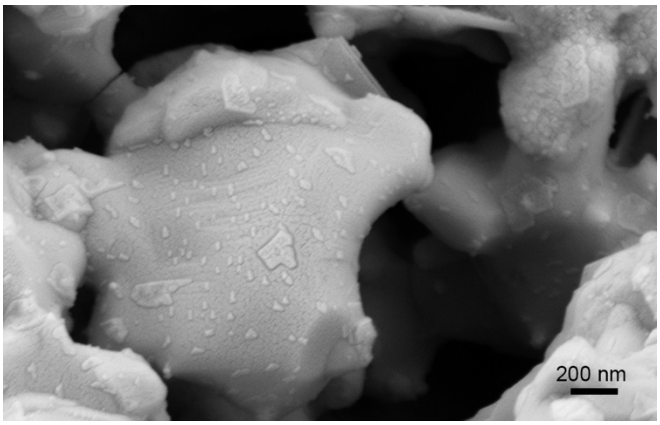

Figure 4.17 SEM images of Sm10BCF electrode after EIS measurement.

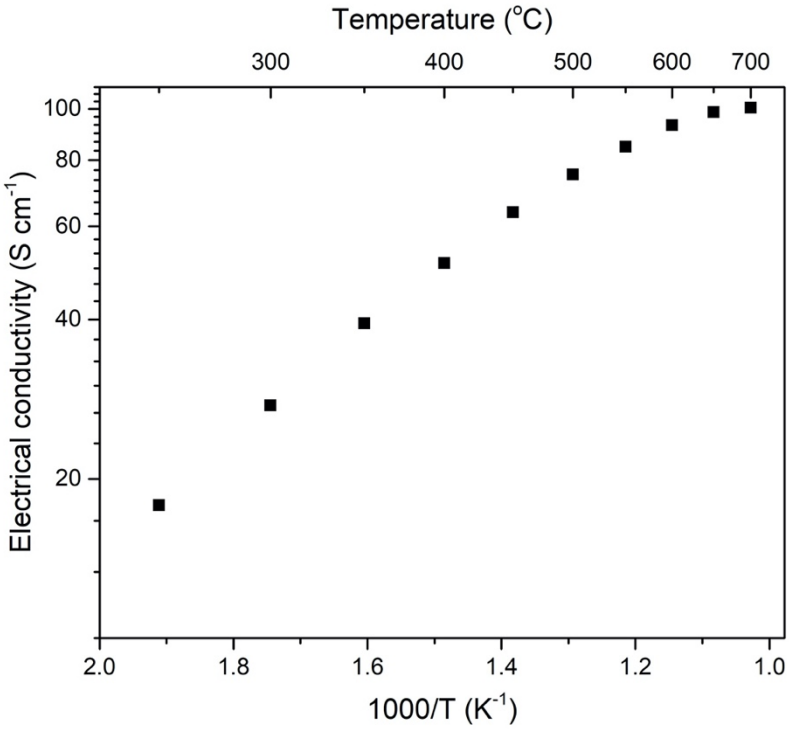

Figure 4.18 The electrical conductivity of Sm10BCF versus temperature.

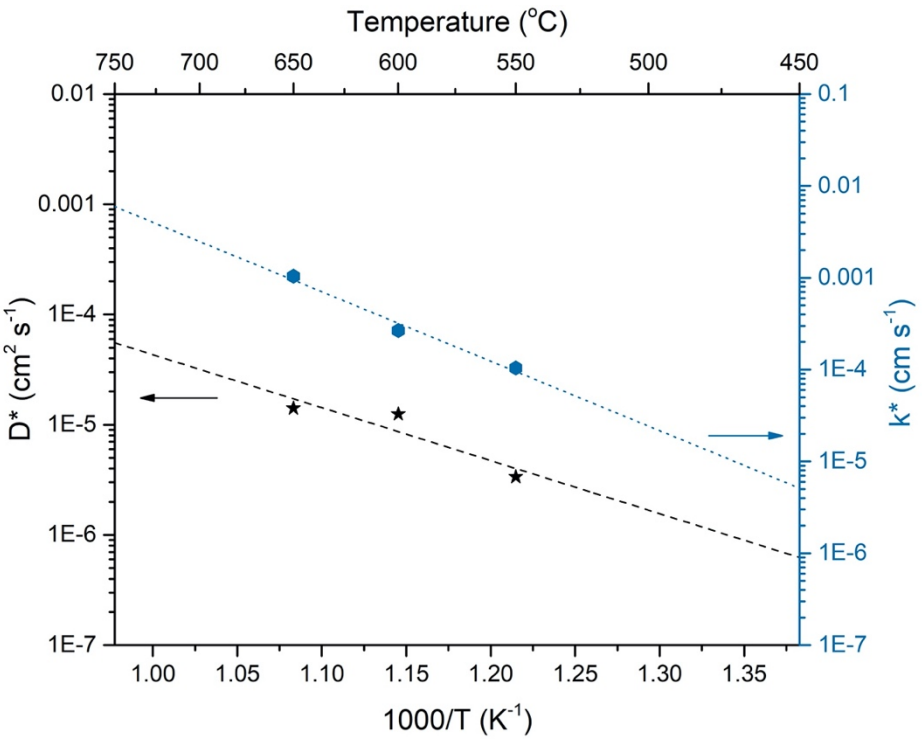

Figure 4.19 Values of D* and k* for Sm10BCF with regard to the temperature dependence derived from the ECR measurement.

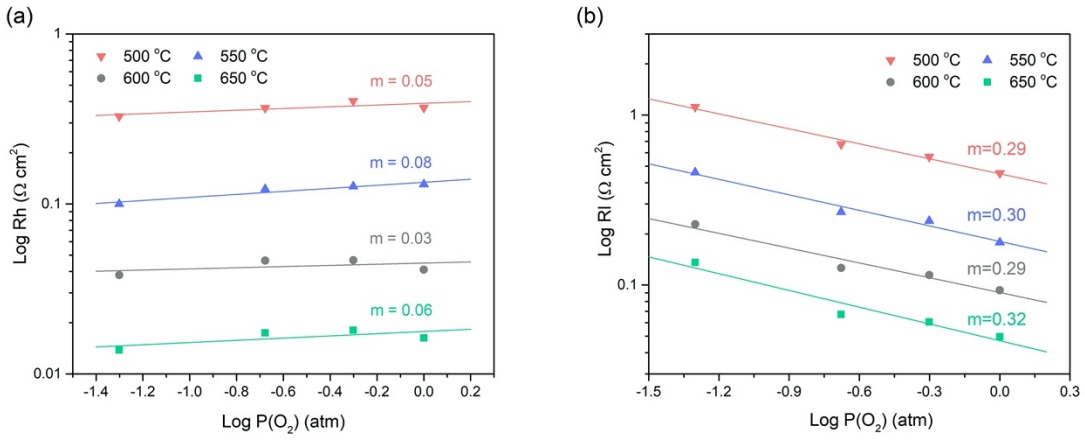

Figure 4.20 Correlations between Rh (a), Rl (b) and applied oxygen partial pressures at different temperatures.

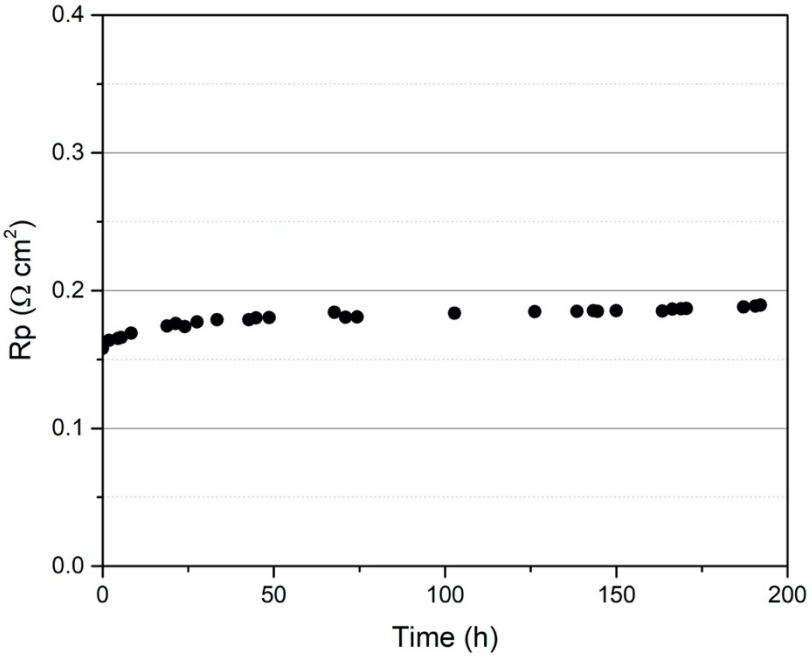

Figure 4.21 Short-term stability of symmetrical cell Sm10BCF | SDC | Sm10BCF tested at 600 ºC in air for 192 h.

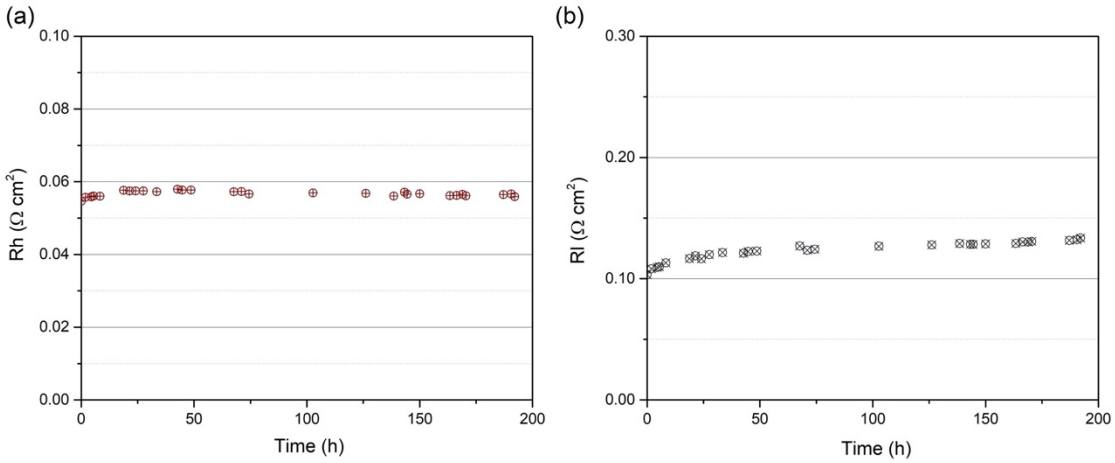

Figure 4.22 Time history of the Sm10BCF cathode polarization resistance tested at 600 ºC: (a) high frequency process, (b) low frequency process.

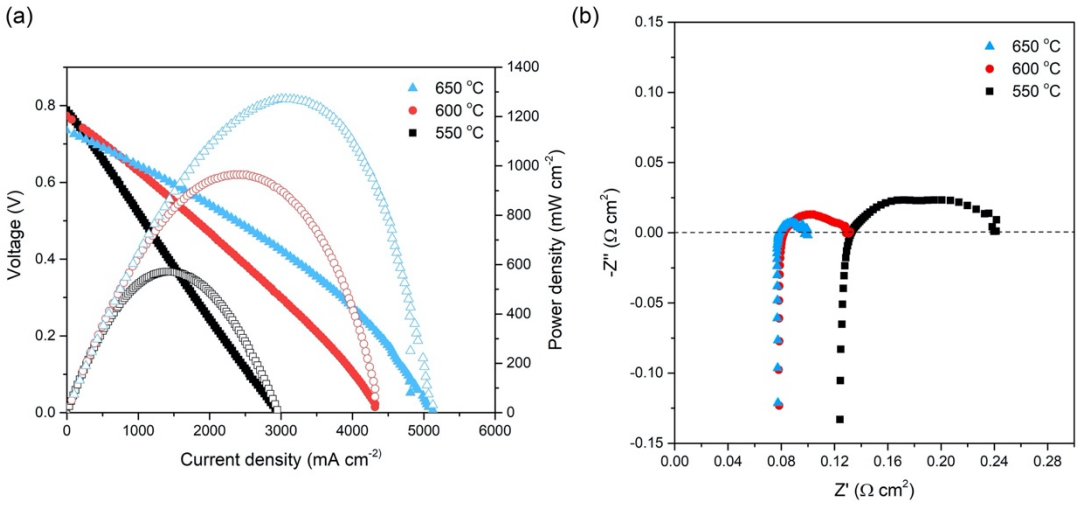

Figure 4.23 I-V and I-P curves of Anode supported single cell with the configuration of Sm10BCF | SDC | NiO + SDC from 550-650 ºC (a) EIS curves of the single cell at OCV condition (b).

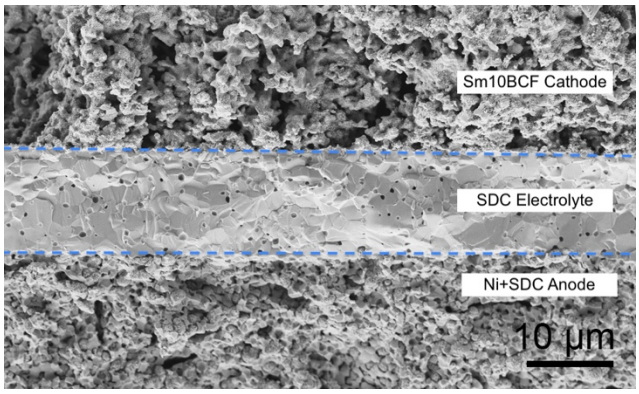

Figure 4.24 Cross-sectional SEM image of single cell after testing.

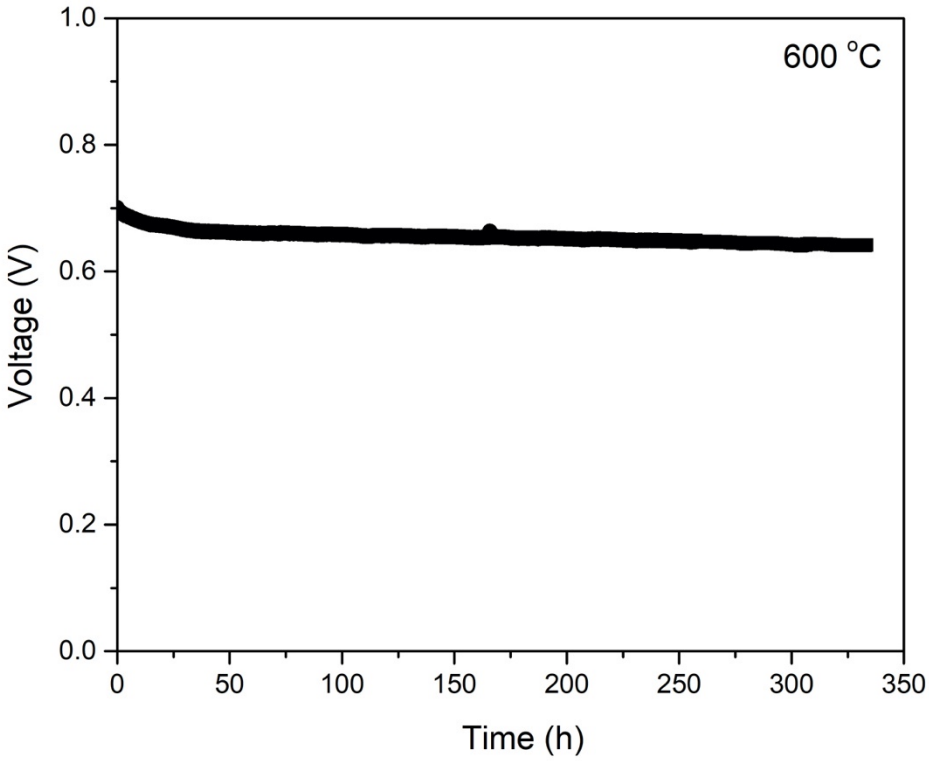

Figure 4.25 Electrochemical performance stability test of a fuel cell with Sm10BCF cathode under a constant current density of 600 mA cm^{-2} at 600 °C.

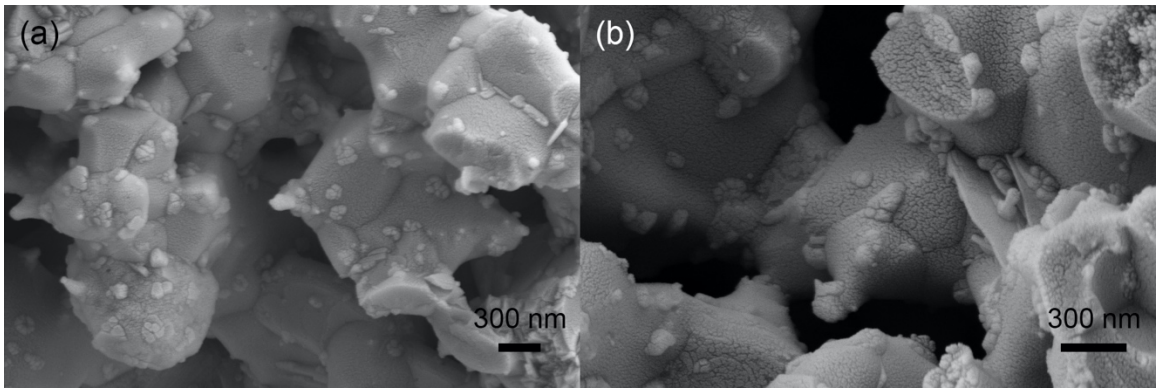

Figure 4.26 SEM images of Sm10BCF cathode in symmetrical cell (a) and single cell (b) after stability test.

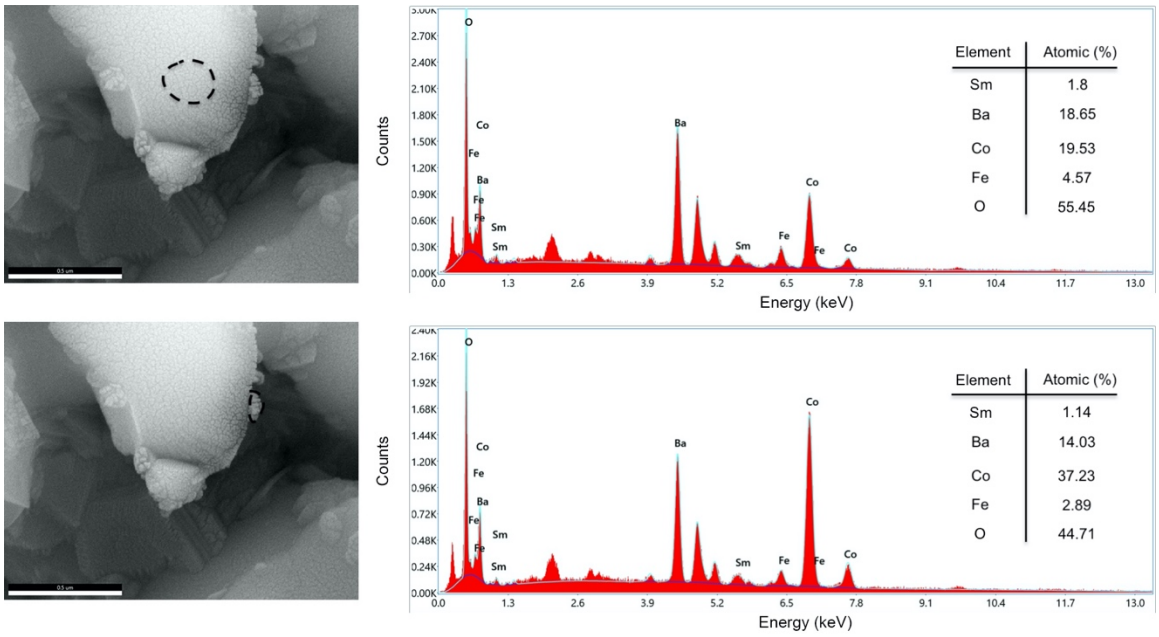

Figure 4.27 EDX scanning results of Sm10BCF cathode after symmetrical cell stability test.

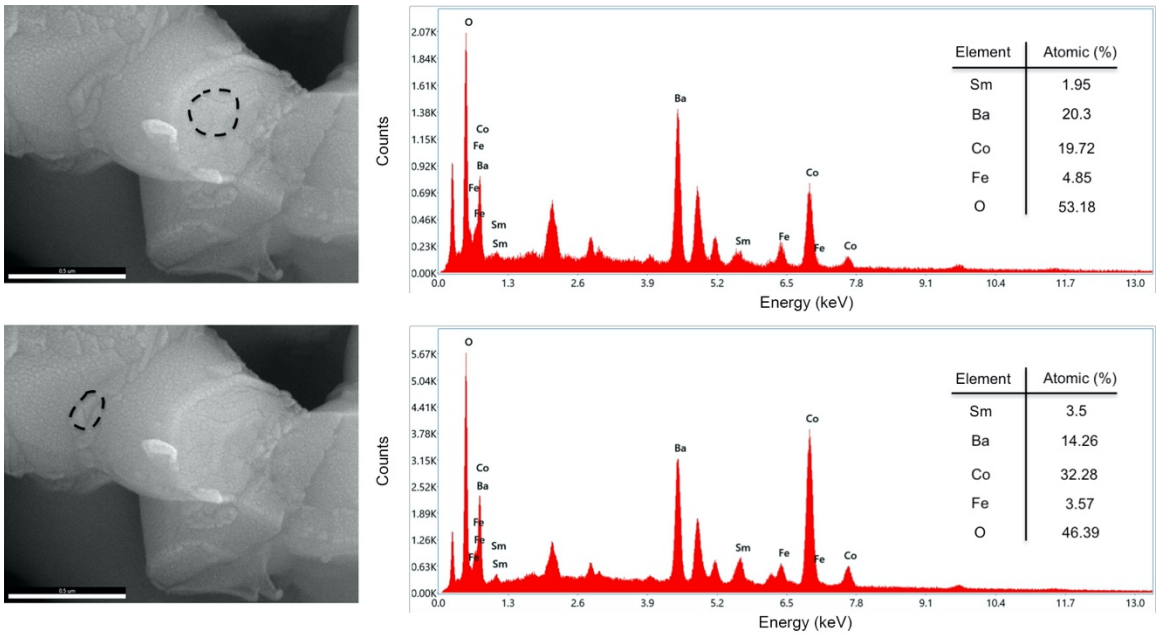

Figure 4.28 EDX scanning results of Sm10BCF cathode after single cell stability.

CHAPTER 5

AN A-SITE CATION DEFICIENT PEROVSKITE ENABLED HIGH CATALYTIC ACTIVITY AND STABILITY AS CATHODE FOR LOW-TEMPERATURE SOLID OXIDE FUEL CELLS

5.1 Introduction

Solid oxide fuel cells (SOFCs) can directly convert chemical energy to usable electrical energy, with the advantageous features of high conversion efficiency, low emission and fuel flexibility.[1, 4] [155] However, the conventional SOFCs usually operate at high temperatures (>850 ^{o}C), which leads to high performance degradation rates and high cost due to the strict requirements on material selection. Thus, the high operating temperature is the key technical issue that hinder the development and commercialization of this transformative technology.[1] Lowering the operating temperature to an intermediate range (IT, 650-800 ^{o}C) or even to a low temperature range (LT, ≤ 650 ^{o}C) enable extended lifetime of devices and reduced cost due to wider material choices for interconnects (e.g. metallic interconnects) and balance-of-plant systems. [141] However with reducing the operating temperature, the degraded catalytic activity of cathode material has become the dominant cause of cell losses due to the high activation energy required for oxygen reduction reaction (ORR) occurring in the cathode, especially for the LT-SOFCs.[4, 156, 157] Therefore, it is of practical and fundamental

significance to develop cathode materials with reduced polarization losses and good stability towards ORR at lower temperatures.

Mixed ionic and electronic conductor (MIEC) has been believed to be a promising candidate with excellent ORR activity to enable reduced operating temperature to low temperature range.[8, 158] Among the recently developed MIEC, a family of cobalt (Co)-based perovskites $BaCo_{1-x}Fe_xO_3$ is a promising parent component for cathode materials that exhibit exceptional catalytic activity at low temperatures.[21, 66, 70, 159] However, at low temperatures, $BaCo_{1-x}Fe_xO_3$ cannot sustain the ORR-favored cubic symmetry but convert to a hexagonal structure at low temperature due to the size mismatch between A-site Ba and B-site Co/Fe. Moreover, the phase transition would bring a 10% volume change and the formation energy of oxygen vacancy in the hexagonal lattice is much higher than that in the cubic lattice.[56] Thus, doping cations into the A-site and B-site of $BaCo_{1-x}Fe_xO_3$ was used as a strategy to stabilize the cubic structure down to low temperatures and enhance catalytic activity towards ORR. For instance, alkaline earth element Sr can be used to replace Ba in the A-site of $BaCo_{1-x}Fe_xO_3$ to form $Ba_{0.5}Sr_{0.5}Co_{0.8}Fe_{0.2}O_{3-\delta}$ (BSCF) and elements like Nb or Y can be doped in the B-site to form $BaCo_{0.7}Fe_{0.2}Nb_{0.1}O_{3-\delta}$ or $BaCo_{0.8}Fe_{0.2}Y_{0.1}O_{3-\delta}$, which all show superior activity for ORR at reduced temperature. [21, 70, 71, 160] A research of Zr and Y co-doped $BaCo_{0.4}Fe_{0.4}Zr_{0.1}Y_{0.1}O_{3-\delta}$ is evaluated as cathode material for SOFCs and protonic ceramics fuel cells, showing attractive kinetic property at low to intermediate temperature range. [159] Thus, co-doping of Zr and Y in the B-site of $BaCo_{1-x}Fe_xO_3$ brings positive effect towards the ORR activity. However, Co-based cathode materials also exhibits poor phase stability, thermal expansion and CO_2 tolerance that limit its practical application.

In addition to doping strategy, the introduction of A- or B-site cation deficiency was also found as an effective method to improve the catalytic activity of the cathode. For the simple perovskite ABO_3, the ratio of the A and B-site cations is usually 1:1. Due to the tolerance of the perovskite structure against the composition change, the perovskite structure can tolerance a certain non-stoichiometry while maintaining the structure.[161] In the cation deficient cases, the B-site cation deficiency is believed less energetically favored than the A-site cation deficiency because of the stability of BO_3 sublattice.[162] [18] By introduction of the A-site cation deficiency, the catalytic activity of the cathode might be improved due to the formation of additional oxygen vacancies within the lattice caused by charge-compensated.[163, 164] Moreover, for stoichiometric ABO_3 oxides, A-site element enriched surfaces are frequently found because of lattice mismatch, as well as electrostatic interaction.[165, 166] The cation segregation could be suppress by A-site cation deficiency leading to improved stability.[95] However, on the other hand, A-site cation deficiency may bring negative effect on electrical conducting.[54, 167] And the defected cation sites may act as trap sites for the mobility of oxygen ions, leading to a reduction in oxygen diffusion.[145] Both the barrier in electronic and ionic conducting could results in the poor activity. Moreover, when introducing A-site cation deficiency, it is found that the perovskite containing Co has difficulty to form the desired composition because of the segregation of metal oxides from perovskite structure.[168] As mentioned above, BSCF shows excellent ORR activity. The content of A-site cation deficiency can highly affect the property of the perovskite oxides. For example, in 20 % A-site cation deficient $(Ba_{0.5}Sr_{0.5})_{0.8}Co_{0.8}Fe_{0.2}O_{3-\delta}$, an impurity of $(Fe,Co)_3O_4$ is found besides the perovskite phase. The introduction of 3% A-site cation deficiency can make it more

thermos-mechanically compatible with the electrolytes by decreasing the thermal expansion coefficient (TEC) of the cathode, while the polarization resistance of $(Ba_{0.5}Sr_{0.5})_{0.97}Co_{0.8}Fe_{0.2}O_{3-\delta}$ increased from 0.093 Ω cm^2 for $Ba_{0.5}Sr_{0.5}Co_{0.8}Fe_{0.2}O_{3-\delta}$ to 0.138 Ω cm^2 at 600 ^oC.[54] For $BaCo_{0.7}Fe_{0.2}Nb_{0.1}O_{3-\delta}$, the kinetic performance was highly promoted by the introduction of 10% A-site cation deficiency. The polarization resistance of $Ba_{0.9}Co_{0.7}Fe_{0.2}Nb_{0.1}O_{3-\delta}$ was decreased from 0.230 to 0.09 Ω cm^2 in comparison to the A-site fully occupied $BaCo_{0.7}Fe_{0.2}Nb_{0.1}O_{3-\delta}$ due to the formation of additional oxygen vacancies.[146] Thus, the introduction of A-site cation deficiency should be well-designed and understood so that the introduction of cation deficiency can bring a beneficial effect for physical and chemical properties of cathode material.

Herein, we propose a new series of cathode material, $Ba_{1-x}Co_{0.6}Fe_{0.2}Zr_{0.1}Y_{0.1}O_{3-\delta}$ (x = 0, 0.05 and 0.10), which combines the doping strategy of Zr and Y in the B-site and introduction of A-site cation deficiency. The perovskite oxide is investigated as an alternative cathode material operating at low temperature range of 650-500 ^oC. The effect of different Ba-deficiency on the properties of the material were characterized, including crystal structure evolution with different Ba-deficiency, electrical conductivity, oxygen reduction reaction activity, stability, CO_2 tolerance as well as single cell performance.

5.2 Experimental

5.2.1 Sample preparation

Combined ethylenediaminetetraacetic (EDTA) and citric acid complexing sol-gel method was used to synthesize $Ba_{1-x}Co_{0.6}Fe_{0.2}Zr_{0.1}Y_{0.1}O_{3-\delta}$ (x = 0, 0.05 and 0.10, denoted as Ba100CFZY, Ba95CFZY and Ba90CFZY, respectively). Stoichiometric amounts of $Ba(NO_3)_2$ (Acros Organics, ACS reagent), $Co(NO_3)_2{\cdot}6H_2O$ (Alfa Aesar, 97.7%),

$Fe(NO_3)_3 \cdot 9H_2O$ (Alfa Aesar, 98.0-101.0%), $ZrO(NO_3)_2$ 35wt.% in dilute nitric acid (Sigma Aldrich) and Y_2O_3 (Alfa Aesar, 99.99%) were dissolved in dilute nitric acid under continuously stirring to form a transparent solution. Citric acid as EDTA were added into the solution with the molar ratio of citric acid:EDTA:metal ions = 1.5:1:1 as complexants. The pH of the solution was adjusted to 8 by adding ammonium hydroxide. After being mixed homogenously, the solution was heated in a water bath at 80 ^oC to evaporate excess water to form a dark purple gel. The gel was then burned on an electrical burner to get a porous precursor. The precursor powder was ground and calcined at 400 ^oC for 2 h to remove the organic residues, subsequently sintered at 1000 ^oC for 6 h in air to obtain the desired material. The resulting powder was then milled within a high energy ball milling machine for 1 h using ethanol as media.

Dense sample bars are used to measure the thermal expansion coefficient and the electrical conductivity. The resultant Ba100CFZY and Ba95CFZY powder was mixed with polyvinyl butyral (PVB) as binder in a weight ratio of 100:2. Then the powders were pressed into bars under sustained pressure at ~300 MPa. The as-prepared green bars of Ba100CFZY and Ba95CFZY were then sintered at 1150 ^oC for 6 h. After polishing and cleaning the sintered sample bars, four silver wires were attached onto the surface of the bars at four well-aligned locations.

5.2.2 Cell preparation

$Ce_{0.8}Sm_{0.2}O_{1.9}$ (SDC, tape cast grade, Fuel Cell Material, USA) was chosen as the electrolyte for symmetrical cell. SDC powder was mixed homogenously with binder PVB (2 wt.%). The resultant powder was dry-pressed under 325 MPa to obtain green pellets, which were sintered at 1450 ^oC for 6 h in air to get dense SDC pellets. And then, the

pellets were polished with sand paper to remove the surfaces, followed by cleaning in the ultrasonic machine. Then, symmetrical cells with the configuration of Ba100CFZY | SDC | Ba100CFZY and Ba95CFZY | SDC | Ba95CFZY were fabricated. Cathode slurry was prepared by mixing Ba100CFZY and Ba95CFZY powder with binder (6 wt.% ethylene cellulose in α-terpineol) in a weight ratio of 2:1. Cathode slurry was then screen-printed on both sides of the SDC electrolyte pellets and subsequently calcined at 1050 ^{o}C for 2 h. Ag wires and Ag paste were attached on both the cathode and anode side acting as the current collector.

5.2.3 Characterizations

The phase analysis were characterized using room temperature powder X-ray diffraction (XRD, Rigaku) with Cu Kα (λ = 1.5406 Å). The diffraction patterns were recorded in the range of $10^{o} \leq 2\theta \leq 90^{o}$ with a step size of 0.02^{o}. Rietveld refinements were performed on the obtained diffraction profiles using GSAS-II program and EXPGUI interface.[68] The microstructure of the cells were examined by scanning electron microscopy (SEM, Zeiss Ultra Plus FESEM, Germany). A Netzsch DIL 402C/3/G dilatometer was used to measure the TEC of Ba100CFZY and Ba95CFZY in air from room temperature to 850 ^{o}C with a heating rate of 5 ^{o}C min^{-1}.

A DC four-probe method was used to measure the electrical conductivity of Ba100CFZY and Ba95CFZY in air at 250-700 ^{o}C with an interval of 50 ^{o}C. A digital multimeter (Agilent 34401A) is used to record the electrical conductivity of the sample bar until it reached equilibrium. The bulk diffusion coefficient (D*) and surface exchange coefficient (k*) were determined by the electrical conductivity relaxation (ECR) measurement. The oxygen partial pressure () in the atmosphere was abruptly shifted from

0.21 to 0.1 atm. Various were obtained by adjusting the flow rate ratio between oxygen and nitrogen. The electrical conductivity of the sample was monitored on-line until it reached an equilibrium at a given temperature or a given . ECRTOOLS were used for data fitting.[150]

Electrochemical impedance spectroscopy (EIS) of symmetrical cells with Ba100CFZY and Ba95CFZY electrodes were performed with a Zahner IM6E electrochemical workstation in air and open circuit voltage (OCV) condition. The EIS was measured in the frequency range of 10^6 to 0.1 Hz with a signal amplitude of 10 mV. The resultant impedance was analyzed by Zview software. In order to get more insights into the kinetics of the electrodes, the polarization resistance of Ba100CFZY | SDC | Ba100CFZY and Ba95CFZY | SDC | Ba95CFZY symmetrical cells were measured at different at different temperatures. The short-term stability of the electrodes was conducted at 650 ^oC in air. The CO_2 tolerance of Ba100CFZY and Ba95CFZY electrodes were also measured using symmetrical cells at 650 ^oC by introducing 1%, 5% and 10% CO_2 into the surrounding atmosphere.

5.3 Results and Discussion

5.3.1 Crystal Structure

The crystal structure of Ba100CFZY, Ba95CFZY and Ba90CFZY was identified by X-ray diffraction, and the XRD patterns are presented in Figure 5.1a. The oxides are well fitted with the cubic symmetry ($BaCoO_{2.23}$, JCPDS 75-0227, *Pm-3m*). No impurity can be detected for Ba100CFZY and Ba95CFZY powder. However, secondary phases (ZrO_2 JCPDS 89-6976 and $BaFeO_3$ JCPDS 14-0180) are observed on the XRD pattern of Ba90CFZY sample. Therefore, 5% seems to be the upper limit for Ba-deficiency in the

A-site of $BaCo_{0.6}Fe_{0.2}Zr_{0.1}Y_{0.1}O_{3-\delta}$ to avoid the appearance of impurity phase. Figure 5.1b depicts the magnified XRD patterns of Ba100CFZY and Ba95CFZY in the range of $2\theta =$ 28-32°. As the A-site cation deficiency increases, the main diffraction peak gradually shifts to higher angles, implying the shrinkage of the lattice. Rietveld refinement was performed on XRD patterns of Ba100CFZY and Ba95CFZY to further verified the above analysis. Cubic structure with the space group *Pm-3m* was used as the initial model for fitting. The refinement results of Ba100CFZY and Ba95CFZY XRD patterns are shown in Figure 5.2a and b respectively. The fitting results are well fitted the XRD profiles as graphically presented. Table 5.1 lists the structural parameters and *R*-factors. A reasonable low weighted profile *R*-factor (R_{wp}), integrated intensity *R*-factor (R_F^2) and goodness of fit (χ^2) are achieved, indicating a reliable fitting when cubic *Pm-3m* space group is used to fit the experimental XRD data. The refinement results also indicate the decrease of the lattice parameters as the A-site cation deficiency increases.

5.3.2 Thermal expansion coefficient

Thermal expansion coefficient (TEC) of cathode is an important parameter for long-term cell operational stability. A good match between the cathode and electrolyte is desired to avoid excessive thermo-mechanical stress that might induce cracks or delamination of the cathode from the electrolyte surface. The SEM micrographs of Ba100CFZY and Ba95CFZY bars sintered at 1150 °C for 10 h are shown in Figure 5.3. Both of the samples exhibit dense microstructure, suggesting that Ba-deficiency has no obvious impact on the sinterability of the two materials. The thermal expansion curves of Ba100CFZY and Ba95CFZY bulk samples are presented in Figure 5.4. Based on $\Delta L/L$ vs. temperature, Ba100CFZY and Ba95CFZY exhibits linear expansion behavior as the

temperature increases. However, there is a inflections on the thermal expansion curve of Ba95CFZY, while no obvious inflection can be seen in Ba100CFZY sample. The occurrence of the inflection can be explained by chemical expansion, which originates from the cobalt ion spin transition and thermal/chemical reduction of cobalt ions to lower states, as well as the formation of oxygen vacancies with increasing temperature.[132, 169] For comparison, the TEC values are calculated in three temperature ranges which are 25-500 ºC, 500-850 ºC and 25-850 ºC and the calculated TEC values are listed in Table 5.2. The TEC values are highly dependent upon the A-site cation deficiency. TEC values decrease with increasing A-site cation deficiency in all three temperature ranges which could be attributed to the increased electrostatic attraction resulting from the decrease of the lattice parameter.[170]

5.3.3 Electrical conductivity

Electrical conductivity is important for a cathode material to ensure efficient current collection. Thus, the A-site cation deficiency effect on electrical conductivity are investigated. Temperature dependence of electrical conductivity of Ba100CFZY and Ba95CFZY are measured. Figure 5.5 shows the electrical conductivity of the sample Ba100CFZY and Ba95CFZY measured in different oxygen partial pressure from 500 to 700 ºC. With increasing P_{O_2}, the electrical conductivity also increases, implying a p-type conducting behavior of both Ba100CFZY and Ba95CFZY. Electron holes and oxygen ions are charge carriers within the oxides. Considering the relatively low mobility of oxygen ions compared to electron holes, the measured electrical conductivity is mainly attributed to the electronic conductivity.[59, 171] Figure 5.6 shows the electrical conductivity of Ba100CFZY and Ba95CFZY in air at different temperatures and

corresponding Arrhenius plots. With increasing temperature, the electrical conductivity also increases, which is originated from the nature of thermally activated charge transport process. Arrhenius plots present a linear behavior, indicating the small polaron hopping mechanism which occurs in the lattice along the strongly overlapped B-O-B chains with B representing transition metal Co and Fe with multiple valence states. However, there is a fluctuation at 350-400 ^{o}C and the rate of electrical conductivity increase for both Ba100CFZY and Ba95CFZY is reduced, which may results from the release of lattice oxygen at high temperature.[59] As shown in Eq. 5-1, the release of lattice oxygen causes the partial annihilation of electron holes which are charge carriers in the two oxides, leading to the conductivity fluctuation.

$$O_O^{\times} + 2h^{\cdot} \rightarrow V_O^{\cdot\cdot} + {}^{1}/_{2}\, O_2 \qquad (5\text{-}1)$$

As shown in Figure 5.6a and b, the electrical conductivity decreases as the A-site cation deficiency increases. This can be explained from the aspects of charge compensation. To maintain the charge neutrality of the material, introduction of A-site cation deficiency requires the increase of the positive charge or decrease of negative charge. Therefore, on the one hand the valance state of B^{x+} may increase to $B^{(x+1)+}$ by releasing an electron to form a free electron, thus leaving behind an electronic holes (electronic compensation); on the other hand an oxygen vacancy can form to compensate the charge (ionic compensation).[172] If electronic compensation was the major method, A-site cation deficiency might results in the partial oxidization of $(Co,\ Fe)^{3+}$ to $(Co,\ Fe)^{4+}$ which accompanied by the increase of the concentration of electronic holes, resulting in the increase of the electrical conductivity.[59] And if ionic compensation was the major process, the increasing oxygen vacancy concentration could block the electronic transport

through the B-O-B bonds, leading to the decrease of the electrical conductivity. Thus, for Ba100CFZY and Ba95CFZY, the reduced electrical conductivity suggests that the formation of oxygen vacancy is major way for the charge compensation induced by the A-site cation deficiency.

The activation energy (E_a) is also extracted by fitting the Arrhenius plots and calculated from the slope as listed in Figure 5.6. It is found that for Ba100CFZY, E_a is 36.74 kJ mol^{-1} in the low temperature range and 17.84 kJ mol^{-1} in the high temperature range. For Ba95CFZY, the corresponding E_a is 35.62 kJ mol^{-1} and 17.21 kJ mol^{-1}, respectively. As A-site cation deficiency increases, E_a reduces, which can be explained by the hopping mechanism. As we know, the BO_6 octahedra build up a three-dimensional network throughout the perovskite lattice and electronic conducting proceeds via electron holes along the B-O-B bonds. A covalent bond is formed between the oxygen ions and B-site cations due to the polarization of the anions. Therefore, the electronic conducting is supposed to closely related to the covalency of the B-O-B bond.[84] Since A-site cations also attract the anionic orbitals, the covalent B-O-B bond is highly related to the polarization degree of A-site cation. The polarization power can be evaluated by the Coulomb-potential Ze^2/r, where Z is the formal valence, e the elementary charge and r the radius.[173] As A-site cation deficiency increases, the nominal valence of Z_A decreases, resulting in a decrease of Z_A/r_A. A decreasing A-site Coulomb-potential increase the overlap between the anionic p_π and B-site cationic t_{2g} orbitals leading to a more itinerant state hence the decrease of the activation energy for charge carriers conducting.[84]

The oxygen bulk diffusion coefficient (D*) and surface exchange coefficient (k*) are important parameters that highly related to the catalytic activity towards ORR. ECR technique was used to determine D* and k*. With the abrupt change of p_{O_2} of surrounding atmosphere from 0.21 to 0.1 atm, the samples will reach to equilibrium and the electrical conductivity of the samples will increase to a constant value. The curves of normalized electrical conductivity of Ba100CFZY and Ba95CFZY as a function of balanced time at 600 ^{o}C are given in Figure 5.7. The time needed to reach equilibrium for Ba95CFZY is clearly less than that for Ba100CFZY. Shown in Figure 5.8 are the ECR experimental data and fitting curves of Ba100CFZY and Ba95CFZY at 500, 550 and 600 ^{o}C, respectively. The fitting curves are well matched with the experimental data. Values of D* and k* for Ba100CFZY and Ba95CFZY are listed in Table 5.3. Ba95CFZY shows higher D* and k* than that of Ba100CFZY, suggesting faster bulk diffusion process and surface oxygen exchange process, which might be attributed to the additional oxygen vacancies and the lower activation energy for charge carrier conducting that induced by Ba-deficiency. The D* and k* values of Ba95CFZY in this work is larger than the state-of-the-art cathode material BSCF for LT-SOFCs. For instance, the D* and k* of BSCF are 2.5×10^{-5} cm^2 s^{-1} and 2.7×10^{-4} cm s^{-1}at 600 ^{o}C, while for Ba95CFZY, the D* and k* are 8.77×10^{-5} cm^2 s^{-1}and 2.53×10^{-4} cm s^{-1} at 600 ^{o}C, respectively.[70]

5.3.4 Kinetic properties

To evaluate the effect of A-site cation deficiency on the oxygen reduction activity, the electrochemical impedance spectra of symmetrical cells Ba100CFZY | SDC | Ba100CFZY and Ba95CFZY | SDC | Ba95CFZY were investigated at 500-650 ^{o}C in air. The typical EIS of Ba100CFZY and Ba95CFZY electrodes measured at 600 ^{o}C in air are

shown in Figure 5.9. An equivalent circuit with the configuration of $L - R_o - (R_h Q_h) - (R_l Q_l)$ is used to fit the EIS data, which is also presented. Herein, L refers to the inductance of the circuit caused by the electrical equipment and lead wires, R_o represents ohmic resistance induced by electrolyte and electrode backbone as well as current collecting wires. R_i and Q_i are the resistance and constant phase capacitance of high (h) and low (l) frequency processes, respectively. The polarization resistance of electrode (R_p) is then obtained by adding area-corrected R_h and R_l together. The spectral fitting results are also shown in Figure 5.9. In order to compare R_p of Ba100CFZY and Ba95CFZY electrodes, R_o is set to be 0. R_p of Ba95CFZY electrode at 600 °C shows a smaller value than that of Ba100CFZY. The Arrhenius plots of R_p of Ba100CFZY and Ba95CFZY versus thermal evolution from 650 to 500 °C are presented in Figure 5.10. R_p values are 0.053, 0.106, 0.219, 0.546 Ω cm^2 for Ba95CFZY, and 0.090, 0.185, 0.425, 1.062 Ω cm^2 for Ba100CFZY at 650, 600, 550 and 500 °C, respectively. As compare to Ba100CFZY, Ba95CFZY electrode shows smaller R_p values at the testing temperatures, especially in low temperature range. Activation energy (E_a) of ORR for the Ba95CFZY electrode is 124.34 kJ mol^{-1}, lower than that of Ba100CFZY (126.01 kJ mol^{-1}). A lower activation energy indicate a lower chemical barrier for oxygen reduction, hence better ORR activity at lower temperature which is of great importance for developing the cathode materials for LT-SOFC. The decreased R_p as A-site cation deficiency introduced into Ba100CFZY can be explained from two aspects. On one hand, as discussed above, Ba95CFZY shows better surface exchange and bulk diffusion properties. The introduce of A-site cation deficiency could lead to creation of extra oxygen vacancies, which in turn brings catalytic performance improvements of Ba95CFZY. On the other hand, it's

reasonable to expect that migration barrier for oxygen anions through the perovskite lattice may have an impact on the catalytic activity of cathode material. The average metal-oxygen bond energy (ABE) could provide an estimation of the energy required to break a lattice cation-oxygen bond. For perovskites $A_xA'_{1-x}B_yB'_{1-y}O_{3-\delta}$ where that A-site cation are 12 coordinate and those for B-site 6 coordinate, ABE can be given by:[174]

$$\mathrm{ABE} = \mathrm{ABE(A-O)} + \mathrm{ABE(B-O)} \tag{5-2}$$

$$\mathrm{ABE(A-O)} = \frac{x}{12\cdot m}\left(\Delta_f H^o_{A_mO_n} - m\Delta H^o_A - \frac{n}{2}D_{O_2}\right) + \frac{1-x}{12\cdot m}\left(\Delta_f H^o_{A'_mO_n} - m\Delta H^o_{A'} - \frac{n}{2}D_{O_2}\right) \tag{5-3}$$

$$\mathrm{ABE(B-O)} = \frac{y}{6\cdot m}\left(\Delta_f H^o_{B_mO_n} - m\Delta H^o_B - \frac{n}{2}D_{O_2}\right) + \frac{1-y}{6\cdot m}\left(\Delta_f H^o_{B'_mO_n} - m\Delta H^o_{B'} - \frac{n}{2}D_{O_2}\right) \tag{5-4}$$

where $\Delta_f H^o_{A_mO_n}$, $\Delta_f H^o_{A'_mO_n}$, $\Delta_f H^o_{B_mO_n}$ and $\Delta_f H^o_{B'_mO_n}$ are the standard formation heats of A_mO_n, A'_mO_n, B_mO_n and B'_mO_n oxides; ΔH^o_A, $\Delta H^o_{A'}$, ΔH^o_B and $\Delta H^o_{B'}$ are the standard sublimation heats for metal A, A', B, B' and at 25 °C; and D_{O_2} represents the dissociation energy of oxygen (498.34 kJ mol^{-1}). Specifically, for Ba100CFZY and Ba95CFZY, the composition on the B-site is identical and hence only $\mathrm{ABE(A-O)}$ are evaluated here. Simple calculations indicate that the $\mathrm{ABE(A-O)}$ for Ba95CFZY is -77.36 kJ mol^{-1}, is lower than that of Ba100CFZY which is -81.43 kJ mol^{-1}. The lower ABE is favorable for the oxygen migration, which promotes the ORR catalytic property. Thus, with the extra oxygen vacancies and lower activation energy for oxygen transports, Ba95CFZY shows better oxygen reduction activity.

5.3.5 Rate-limiting steps

The oxygen reduction reaction occurring in the cathode includes several steps, such as oxygen gas diffusion, surface exchange process, charge transfer process, etc.. And some of the steps could limit the rate of reaction. The reaction process is highly dependent on oxygen partial press applied. Mathematically, the relationship between the polarization resistance of single step and oxygen partial pressure can be written as[154]:

$$R_i = k(P_{O_2})^{-m}, i = h, l \tag{5-5}$$

where, R_i is polarization resistance of high or low frequency process, k is a constant, P_{O_2} is oxygen partial pressure, m is reaction order and quantitatively related to rate-limiting steps as follows:

- $m = 1$:

$$O_{2,g} + \mathrm{Ba95CFZY}(s) \leftrightarrow O_{2,ads}(\mathrm{Ba95CFZY}) \tag{5-6}$$

  Molecular oxygen adsorption process onto porous electrode surface.

- $m = 0.5$

$$O_{2,ads}(\mathrm{Ba95CFZY}) \leftrightarrow 2O_{ads}(\mathrm{Ba95CFZY}) \tag{5-7}$$

  Dissociation of adsorbed molecular oxygen into atomic oxygen.

- $m = 0.25$

$$O_{ads}(\mathrm{Ba95CFZY}) + 2e^- + V_O^{\cdot\cdot} \leftrightarrow O_O^{\times} + \mathrm{Ba95CFZY}(s) \tag{5-8}$$

  Charge transfer reaction for oxygen anion formation and incorporation into oxygen vacancy.

In order to get more information of Ba95CFZY cathode catalytic activity, the symmetrical cell Ba95CFZY | SDC | Ba95CFZY were investigated under different P_{O_2} at different temperatures. The correlation between the polarization resistance in high and

low frequency and applied oxygen partial pressure are presented in Figure 5.11. The m values for high frequency are 0.22, 0.22 and 0.25 at 550, 600 and 650 °C, respectively, which are close to the theoretical value 0.25. Thus, the high frequency process is mainly related to the charge transfer process. Only high frequency process exists when testing under high oxygen partial pressure and high temperature (e.g. P_{O_2}= 1.0 atm, T = 650 °C), while low temperature process is appeared under low oxygen partial pressure (e.g. P_{O_2}= 0.05 atm, T = 650 °C). The impedance response of the low frequency is found to have a dependence of 0.52, 0.57 and 0.63 at 550, 600 and 650 °C, respectively, suggesting that dissociation of adsorbed molecular oxygen into atomic oxygen is mainly associated to the low frequency process. Accordingly, charge transfer and oxygen molecule dissociation process are two rate-limiting steps for Ba95CFZY cathode. However, compared with oxygen dissociation process, charge transfer is the pronounced process to determine the rate.

5.3.6 Electrochemical kinetic stability and CO_2 tolerance

Stability of cathode material is critical for the practical application of SOFCs. In this section, the short-term stability of Ba100CFZY and Ba95CFZY electrodes were carried out and the effect of A-site cation deficiency on the stability is discussed. The polarization resistance of symmetrical cells with Ba100CFZY and Ba95CFZY electrodes were measured in air for ~250 h and the time evolution of the polarization resistances are shown in Figure 5.12. It can be seen that R_p of Ba100CFZY electrode increases gradually in the first 50 hours. Beyond 50 h, R_p shows a little fluctuation and reaches a stable state till the end of the test. R_p of Ba100CFZY electrode is 0.089 Ω cm^2 at the beginning of the test and reaches 0.098 Ω cm^2 after 244 hours' test, with an increasing rate of 3.69 × 10^{-5}

Ω cm^2/h. For Ba95CFZY electrode, R_p fluctuates in the first 25 hours and increases between 25 and 50 hours, and then exhibits a relatively stable state to the end. R_p of Ba95CFZY electrode starts from 0.057 Ω cm^2 and reaches 0.059 Ω cm^2 after the 239 hours' test, with an increasing rate of 8.37 × 10^{-6} Ω cm^2/h. In order to identify the degradation mechanism, more analyses are performed in detail. As mentioned above, the overall R_p of the electrode can be linked to specific ORR steps, while charge transfer and oxygen dissociation are related to the processes for the high and low frequency. As shown in Figure 5.12, the increase of R_p for the two electrodes are mainly during in the first 50 hours. For this reason, the time evolution of R_h and R_l are extracted from the EIS measurements for the first 50 h and shown in Figure 5.13. For both Ba95CFZY and Ba100CFZY electrodes, the change of R_p with time is mainly induced by the evolution of R_h, while R_l only shows some fluctuations. As confirmed above, high frequency polarization is associated with the charge transfer process for oxygen anion formation and incorporation in an oxygen vacancy. Thus, it is reasonable to assume that the property of electrode surface, such as oxygen vacancies near the surface, affect the catalytic property of the cathode. It is well accepted that in perovskite-based electrode material, specific cations (e.g. Sr^{2+}, Ba^{2+}, etc.) trend to segregate to the surface because of cation size mismatch, impacting the catalytic activity of the electrodes.[95] For example, Ba segregation appears in $La_{0.5-x}Pr_xBa_{0.5}CoO_{3-\delta}$ and $LnBaCoO_{5+\delta}$.[175, 176] The decrease of catalytic property could be associated to a negative impact of Ba-surface segregation which could produce a local lattice distortion affecting the oxygen migration.[176] Therefore, the increase of R_h can be attributed to the Ba segregation on the surface occurring during the thermal treatment. Compared with Ba100CFZY, A-site cation

deficiency Ba95CFZY electrode shows better kinetic stability as a function of time. While there is a consensus in the literature that cation deficiency has profound influences on segregation behaviors as well as kinetic properties.[166, 177, 178] The A-site deficiency can suppress the corresponding cation segregation by allowing for more free space in lattice, consequently alleviate the enrichment of Ba on the surface. Thus, A-site cation deficiency Ba95CFZY shows better short-term stability.

For practical application of SOFCs, the gas supplied to the cathode side may containing a small amount of CO_2. The perovskites containing alkaline-earth cations on the A-site (e.g. Ba and Sr) are susceptible towards CO_2. Ba/Sr in the perovskite oxides can react with CO_2 at elevated temperatures to form surface oxo-carbonaceous species, such as adventitious-like carbon species, monodentate carbonate, bidentate carbonate and carbonate species, which block oxygen exchange at the surface.[119, 120] Therefore, performance degradation of the electrode can occur in the presence of CO_2. In addition, researches have shown that the performance degradation is more severe at lower temperatures (e.g. 450-600 ^oC) than over 700 ^oC under CO2-containing atmosphere.[121, 122, 179] Thus, the investigation of CO_2 tolerance for cathodes used in low temperature is of great importance. For this purpose, to investigate CO_2 tolerance of Ba100CFZY and Ba95CFZY cathodes, 1% CO_2-containing air are supplied to the testing chamber, followed by 5% CO_2-containing air and 10% CO_2-containing air for 3 hours respectively. EIS was performed every half hour during the test. The increase of polarization resistance of Ba100CFZY and Ba95CFZY cathodes measured 600 ^oC are compared and shown in Fig 5.14. $R_{p\ initial}$ is the polarization resistance at the 0^{th} hour in CO_2-free air. It can be seen that $R_p/R_{p\ initial}$ of both Ba100CFZY and Ba95CFZY cathodes increases with

introducing CO_2 into air, which is consistent with other Ba-containing perovskite cathodes such as BSCF, $Ba_{0.9}Co_{0.7}Fe_{0.2}Nb_{0.1}O_{3-\delta}$, etc..[98, 180] The Ba100CFZY and Ba95CFZY powders were thermal treated in 10% CO_2-containing air for 2 hours and characterized by XRD, which are shown in Figure 15. The secondary phase $BaCO_3$ was formed. Therefore, he performance degradation can be attributed to the formation of carbonate after CO_2 contamination, which block ORR active sites leading to the deterioration of surface catalytic property. As shown in Figure 5.14, R_p increase of Ba100CFZY cathode is greater than that of the Ba95CFZY cathode in various CO_2 concentration containing air. The relative peak intensity of BaCO3 of Ba100CFZY is stronger than that of Ba95CFZY as presented in Figure 5.15. This result suggests that A-site cation deficiency can alleviate the formation of secondary phase due to the decrease in the Ba concentration on the surface of the cathode, which is also seen in Sr containing materials.[132] In the open literature, the R_p of the state-of-the-art cathode BSCF may reach 27 times its initial value after being exposed to 5% CO_2-containing air for 15 min at 600 ^oC.[98] The R_p of Ba100CFZY and Ba95CFZY in this paper reached 2.55 times and 2.40 times, respectively, after being exposed to 1% CO_2-containing air for 3 hours follow by 5% CO_2-containing air for 3 hours, as shown in Figure 5.14b. This simple comparison indicates that Ba100CFZY and Ba95CFZY cathodes have better CO_2 tolerance than the widely studied BSCF cathode. Moreover, A-site cation deficiency may provide a possible strategy for optimization the CO_2 tolerance property.

5.4 Conclusion

A new series of A-site deficient $Ba_{1-x}Co_{0.6}Fe_{0.2}Zr_{0.1}Y_{0.1}O_{3-\delta}$ (x = 0, 0.05 and 0.10) has been synthesized and characterized as a cathode material for LT-SOFCs. The results

indicate Ba95CFZY is single phase while impurities are found in Ba90CFZY. The introduction of Ba deficiency induces the decrease of lattice parameters. The TEC of Ba95CFZY is lower than that of Ba100CFZY and make it more compatible with electrolyte. The Ba-deficient Ba95CFZY exhibits lower electrical conductivity which might be attributed to additional oxygen vacancies due to the charge neutrality from the introduction of Ba deficiency. However, Ba95CFZY show lower activation energy for electrical conducting. The decreasing A-site Coulomb-potential of Ba95CFZY leads to a more itinerant state hence the decrease of the activation energy for charge carriers conducting. The creation of additional oxygen vacancies and smaller average bonding energy also promotes the higher ORR activity. Polarization resistance values are 0.053, 0.106, 0.219, 0.546 Ω cm^2 for Ba95CFZY, and 0.090, 0.185, 0.425, 1.062 Ω cm^2 for Ba100CFZY at 650, 600, 550 and 500 ^oC, respectively. Charge transfer is the pronounced rate-limiting steps in the ORR for the Ba95CFZY cathode. Moreover, Ba95CFZY exhibits excellent structural stability. The CO_2 tolerance is also improved as a result of introducing the Ba deficiency. The results justify the potential of Ba95CFZY as cathode material for LT-SOFCs due to its high ORR activity and stability.

Table 5.1 Lattice parameters and R-factors for Ba100CFZY and Ba95CFZY derived from XRD Rietveld refinement.

	Ba100CFZY	Ba95CFZY
a (Å)	4.1273(9)	4.0986(8)
V(Å^3)	70.312	68.854
χ^2	1.60	2.78
R_{wp} (%)	2.713	4.509
$R_F{}^2$ (%)	2.454	4.438

Table 5.2 Linear TEC (10^{-6} K^{-1}) values of Ba100CFZY and Ba95CFZY calculated from the thermal expansion curves for different temperature ranges.

	25-500 °C	500-850 °C	25-850 °C
Ba100CFZY	26.05	22.99	24.54
Ba95CFZY	23.90	22.84	22.79

Table 5.3 bulk diffusion coefficient (D*) and surface exchange coefficient (k*) of Ba100CFZY and Ba95CFZY at different temperatures.

	Ba100CFZY		Ba95CFZY	
	D* (cm^2 s^{-1})	k* (cm s^{-1})	D* (cm^2 s^{-1})	k* (cm s^{-1})
500 °C	5.40×10^{-6}	1.68×10^{-4}	1.24×10^{-5}	2.39×10^{-4}
550 °C	7.47×10^{-6}	4.29×10^{-4}	1.84×10^{-5}	1.10×10^{-3}
600 °C	1.19×10^{-5}	7.78×10^{-4}	8.77×10^{-5}	2.53×10^{-3}

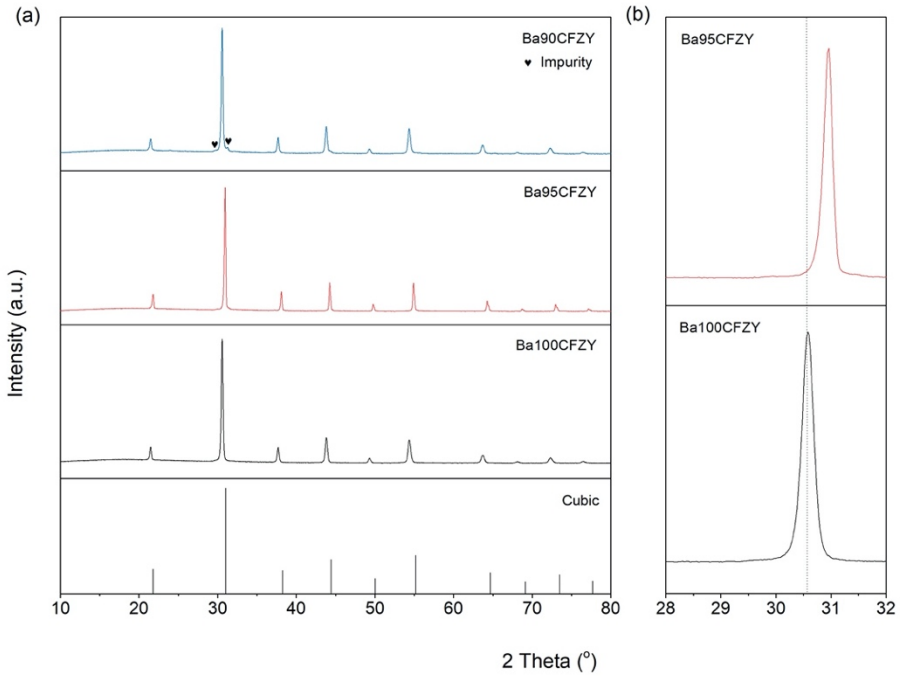

Figure 5.1 XRD patterns of $Ba_{1-x}Co_{0.6}Fe_{0.2}Zr_{0.1}Y_{0.1}O_{3-\delta}$ (x = 0, 0.05 and 0.10) powdered calcined at 1000 ºC in air for 6 h and peak positions of cubic structure $BaCoO_{2.23}$ (JCPDS 75-0227, Pm-3m) (a) and magnified XRD patterns of Ba100CFZY and Ba95CFZY in the range of of 2θ = 28-32º.

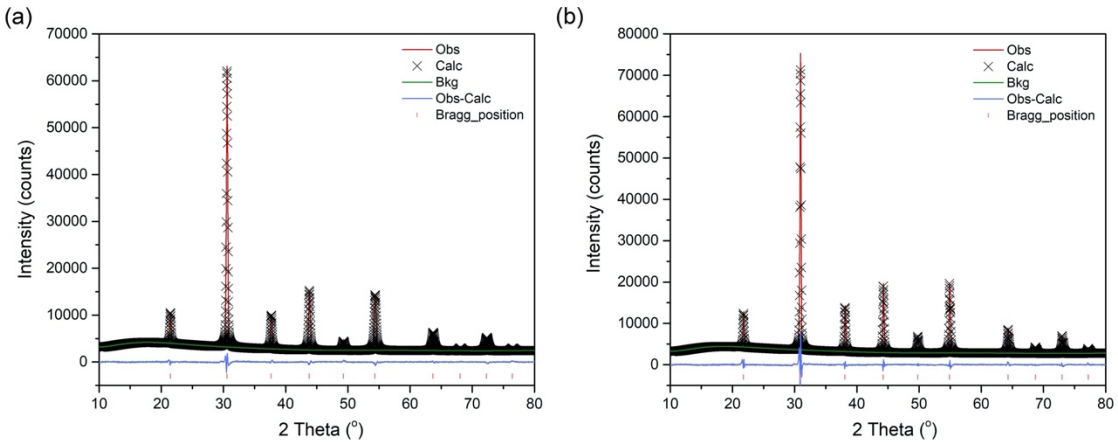

Figure 5.2 Rietveld refined diffraction patterns of Ba100CFZY (a) and Ba95CFZY (b).

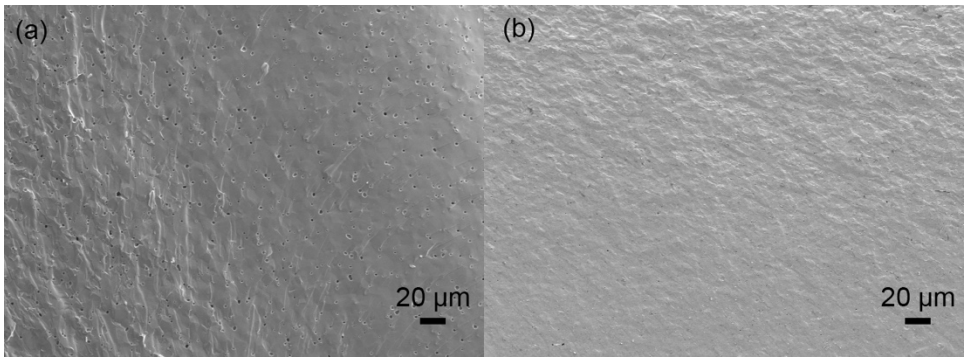

Figure 5.3 Cross-sectional SEM images of Ba100CFZY and Ba95CFZY bars after being sintered at 1150 ^{o}C for 10 h.

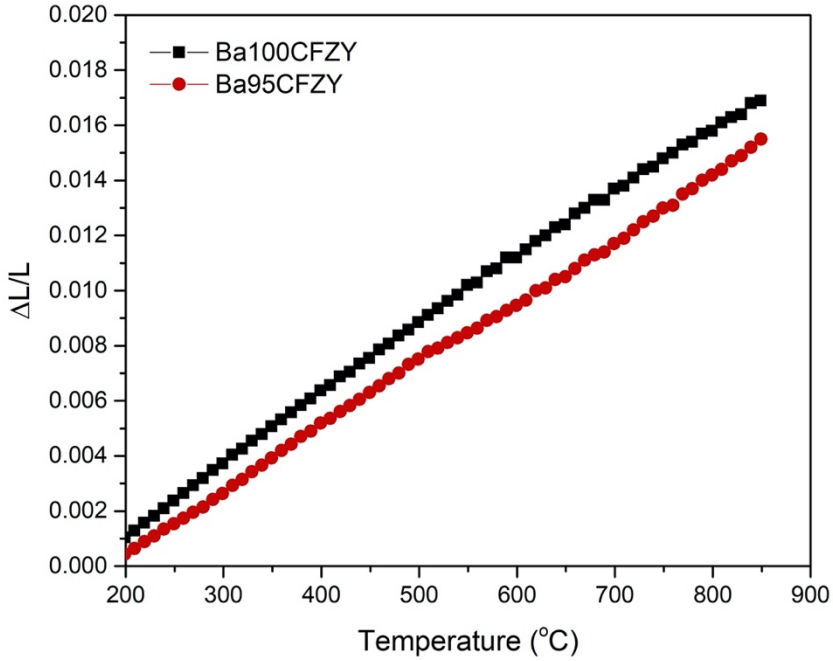

Figure 5.4 The Thermal expansion curves for Ba100CFZY and Ba95CFZY bulk samples.

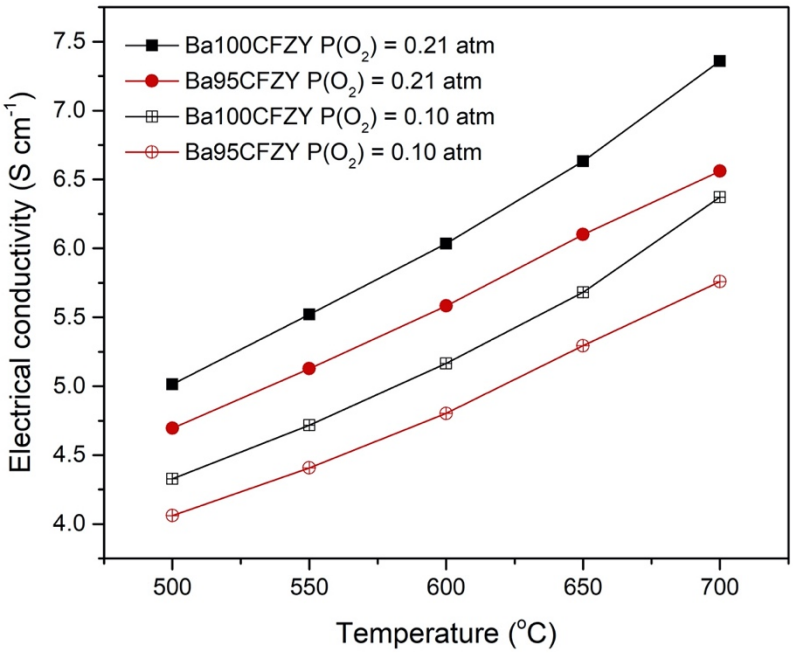

Figure 5.5 Temperature dependence of electrical conductivity of Ba100CFZY and Ba95CFZY at different oxygen partial pressure.

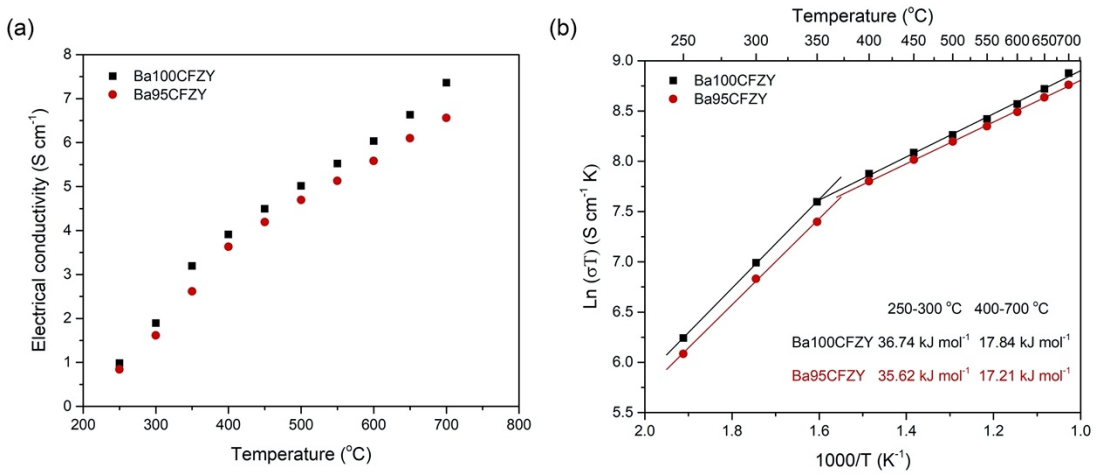

Figure 5.6 The electrical conductivity of Ba100CFZY and Ba95CFZY as a function of temperature (a) and the corresponding Arrhenius plots (b).

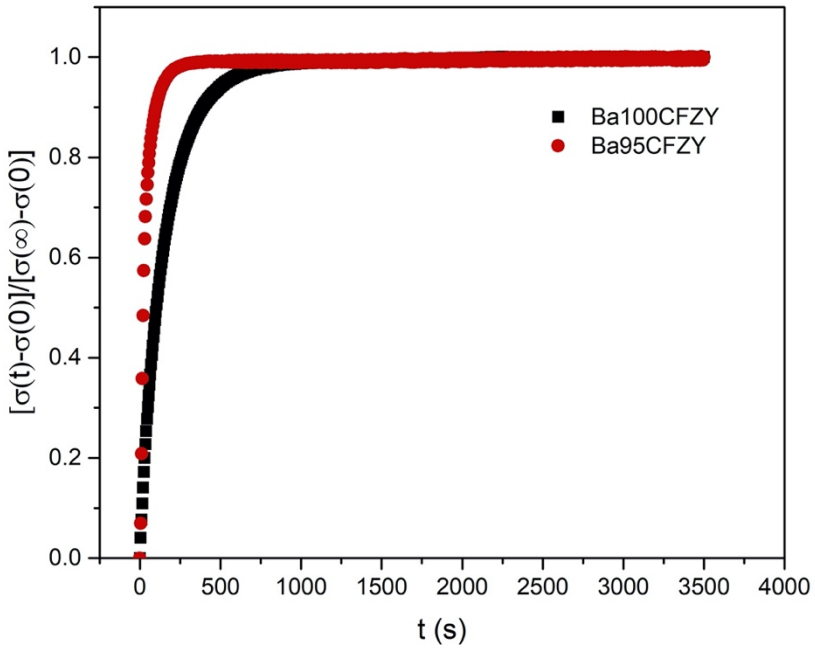

Figure 5.7 Normalized electrical conductivity curves of Ba100CFZY and Ba95CFZY as a functional of relaxing time at 600 ^{o}C with an abrupt change of oxygen partial pressure from 0.21 to 0.1 atm.

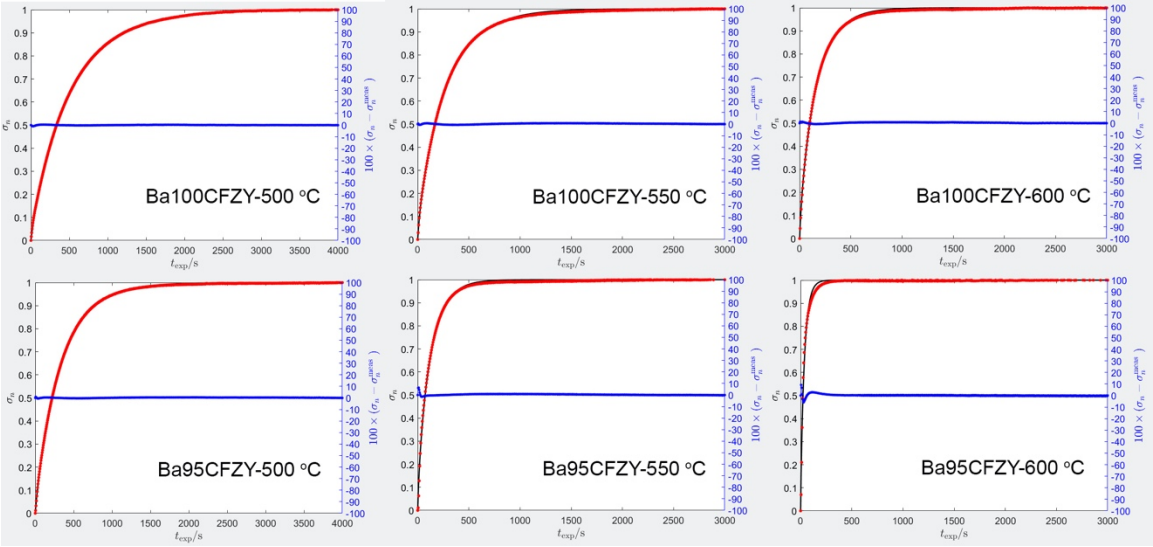

Figure 5.8 ECR experimental curves (red), fitting results (black) and deviations (blue) of Ba100CFZY and Ba95CFZYsamples with an abrupt change of oxygen partial pressure from 0.21 to 0.1 atm at 500, 550 and 600 °C, respectively.

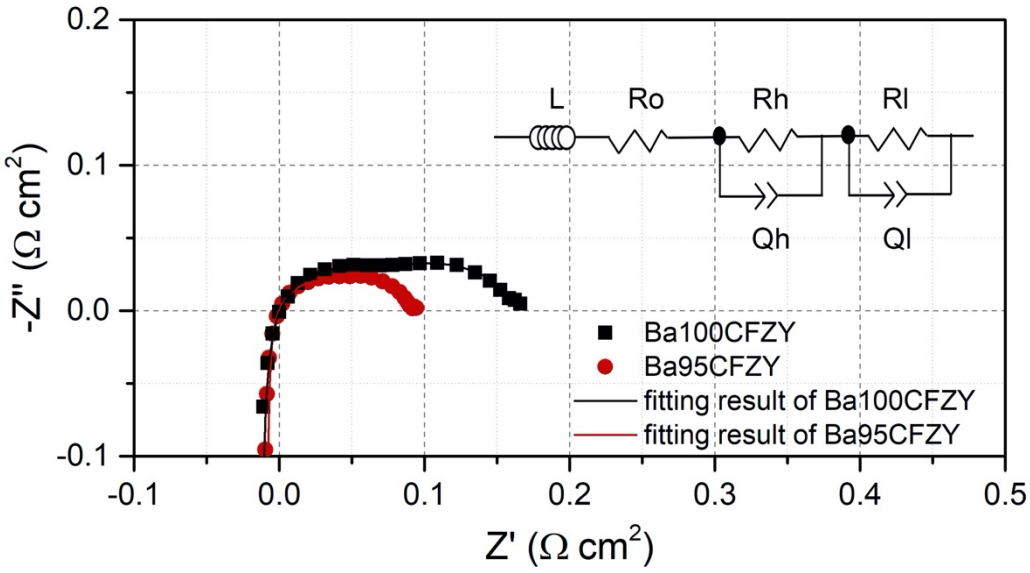

Figure 5.9 Typical Nyquist plots of symmetrical cells with Ba100CFZY and Ba95CFZY electrodes measured at 600 ºC in air. The equivalent circuit model used for curve fitting is inserted.

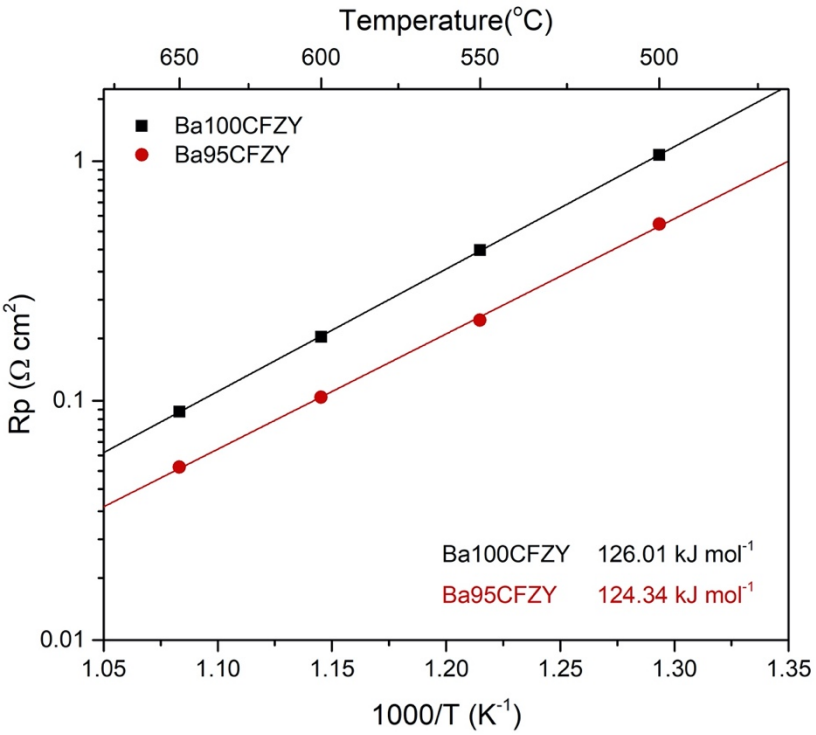

Figure 5.10 Polarization resistance vs. 1000/T of Ba100CFZY and Ba95CFZY electrodes measured in air from 650 to 500 °C.

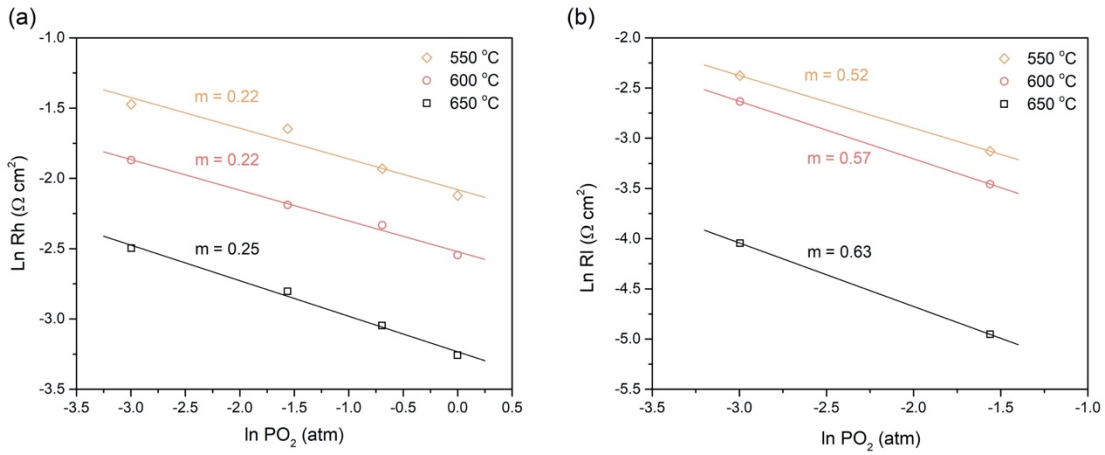

Figure 5.11 Polarization resistance of high frequency (a) and low frequency (b) under different oxygen partial pressures at different temperatures.

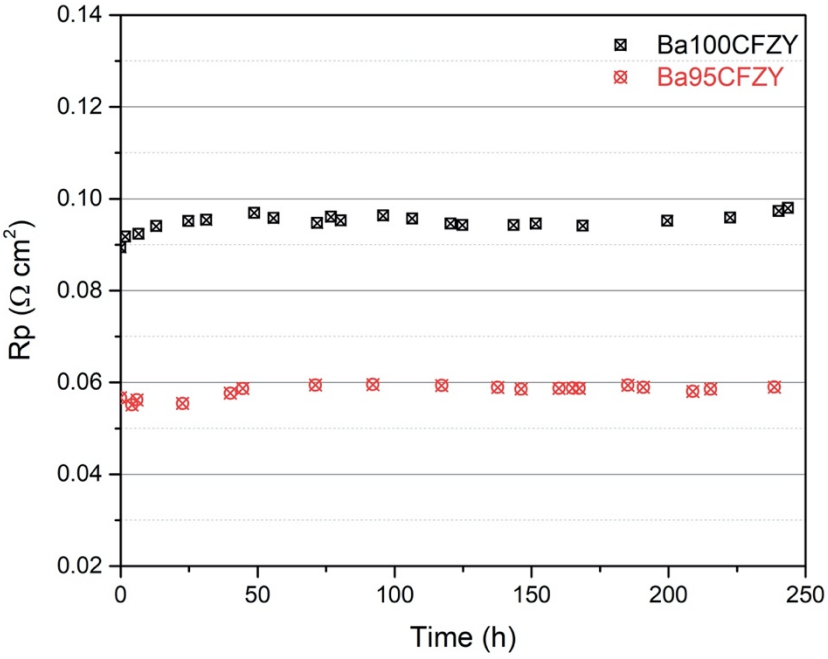

Figure 5.12 Time history of Rp values for Ba100CFZY and Ba95CFZY electrodes at 650 °C in air.

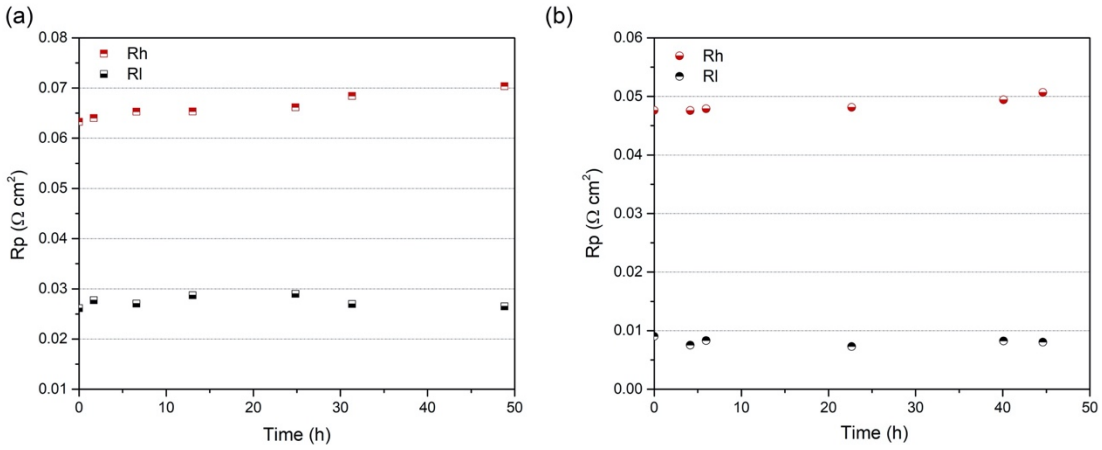

Figure 5.13 Time history of high frequency and low frequency polarization for Ba100CFZY (a) and Ba95CFZY (b) electrode at 650 ^{o}C in air.

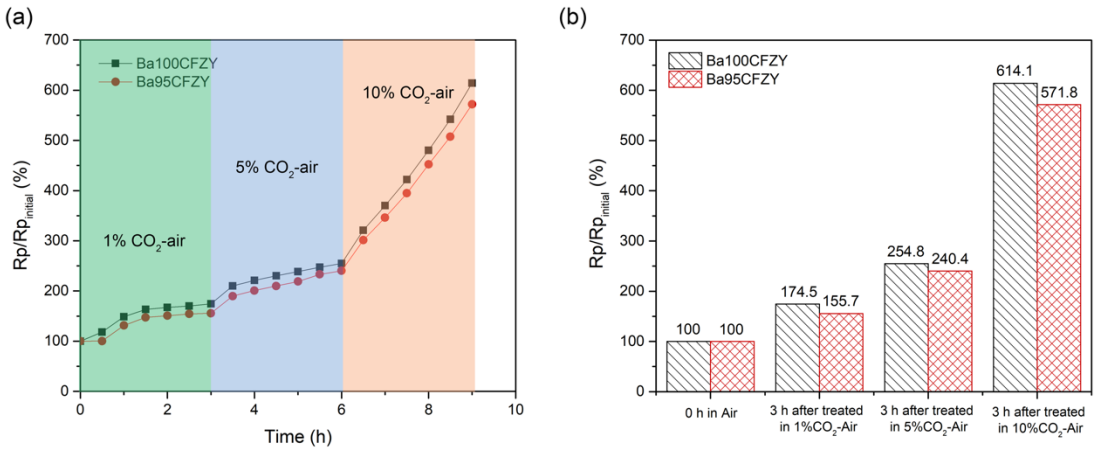

Figure 5.14 Ratio of polarization changes of Ba100CFZY and Ba95CFZY electrodes after introduction of various proportions of CO_2 in to air (a) and the polarization resistance change after treated in various CO_2 containing-air .

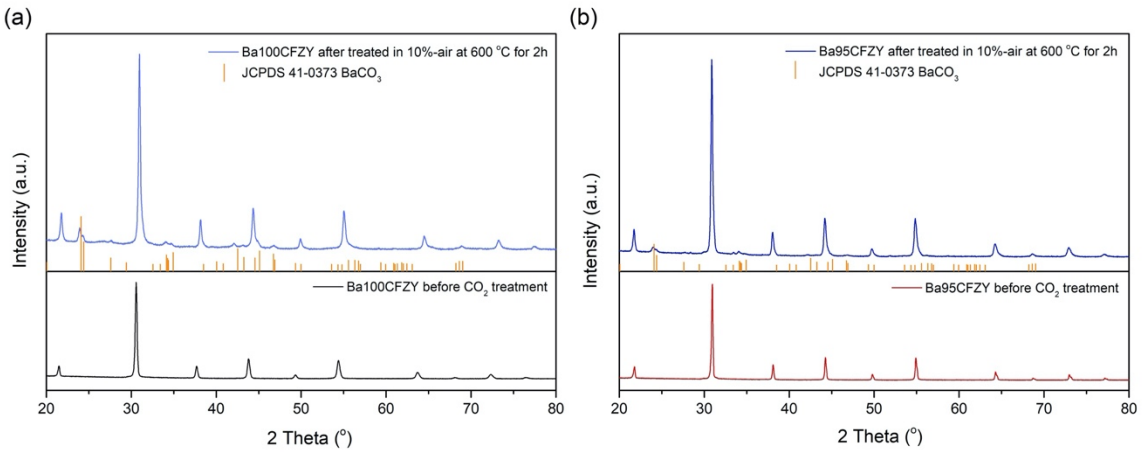

Figure 5.15 XRD patterns of Ba100CFZY (a) and Ba95CFZY (b) before and after treated at 600 °C in 10% CO_2-air for 2 h, respectively, followed by cooling down under the protection of nitrogen gas, and peak position of $BaCO_3$ (JCPDS 41-0373).

CHAPTER 6

SUMMARY

The development of efficient and clean energy is of practical significance as a result of energy supply structure adjustment. Solid oxide fuel cells have attracted considerable attention due to their high efficiency, low pollutant emission and fuel flexibility. However, SOFCs technology must mature further towards commercialization that limited by the high operating temperature (> 850 ^{o}C), which leads to high cost, poor long-term durability as well as the high reactivity between cell components. To further make SOFCs technology economically feasible, considerable progresses have been achieved in lowering the operating temperature from high temperature range to intermediate temperature range (IT, 650-800 ^{o}C) so that performance degradation could be mitigated. Moreover, reducing the operating temperature to low temperature range (LT, ≤ 650 ^{o}C) have the potential to further reduce cost due to wider material choices for interconnects, sealing materials and balance-of-plant, enable acceleration in cell start-up and shut-down. All these features could improve the adoption of SOFC technology in practical application. Nevertheless, with the reduction of operating temperature to low temperature range, insufficient cathodic performance becomes the major challenge because of the thermal activation nature of the processes in the cathode. More specifically, the oxygen reduction reaction (ORR) occurring in the cathode requires high activation energy. As such, looking for cathode materials or innovation cathode

microstructures with excellent kinetic property and stability that enable the operation of SOFCs at relatively low temperature is one of the essential requirements for SOFCs development.

Cobalt-based perovskite is one of the promising electrodes to achieve high catalytic activity at reduced temperatures due to the easily created high concentration oxygen vacancies. Fe partial substitution for Co on B-site may tradeoff stability-activity for $BaCoO_{3-\delta}$ perovskite. However, large radius mismatch between Ba and Co/Fe favors the formation of a low symmetric hexagonal phase $BaCo_{1-x}Fe_xO_{3-\delta}$, which may experience phase structural transitions with varying temperatures and could induce structural reliability issue of associated devices. The B-site doping with high valence elements may facilitate to form cubic $BaCo_{1-x}Fe_xO_{3-\delta}$ perovskite, it could also significantly deteriorate their catalytic property. The Yb^{3+} with ionic radius being larger than those of Co^{4+} and Fe^{4+} is used as B-site dopant to tune Goldschmidt tolerance factor of $BaCo_{1-x}Fe_xO_{3-\delta}$ to 1 and therefore successfully stabilize the cubic structure. Additionally, $BaCo_{0.7}Fe_{0.2}Yb_{0.1}O_{3-\delta}$ exhibits the highest electrical conductivity due to the competing effects on the migration of charge carriers between the low electronegativity of Yb and the hindrance of oxygen vacancies. Yb dopant plays a role of sintering inhibitor, therefore with increasing Yb content, the sintering temperature to densify the corresponding bulk was slightly increased. The $BaCo_{0.7}Fe_{0.2}Yb_{0.1}O_{3-\delta}$ cathode demonstrated the polarization resistances of 0.039, 0.074, 0.161, 0.568 Ω cm^2 at 750, 700, 650 and 600, respectively, the smallest among three Yb doping levels. Surface molecular oxygen dissociation and charge transfer reaction processes were two rate-limiting steps for ORRs associated with $BaCo_{0.7}Fe_{0.2}Yb_{0.1}O_{3-\delta}$ cathode. The $BaCo_{0.7}Fe_{0.2}Yb_{0.1}O_{3-\delta}$ as a

cathode material demonstrated very good stability of lattice structure in a short-term durability test. The peak power densities of the anode-supported microtubular cell NiO-SDC/SDC/$BaCo_{0.7}Fe_{0.2}Yb_{0.1}O_{3-\delta}$ reached 1107, 852 and 480 mW cm^{-2} at 700, 650 and 600 ^{o}C, respectively, suggesting that $BaCo_{0.7}Fe_{0.2}Yb_{0.1}O_{3-\delta}$ is a promising cathode material for IT-SOFCs.

Mixed ionic and electronic conducting (MIEC) perovskite $SrCoO_{3-\delta}$ is a widely studied (electro) catalyst for ORRs and possesses different crystal structures at different temperatures. These temperature dependent phase transitions significantly impact the ordering of oxygen vacancies and electrochemical kinetic properties as well as the reliability of related devices. Some of the crystal structures formed, e.g., hexagonal phases, turn out to be almost impermeable to oxygen gas. Therefore, it is important to stabilize the crystal structure of $SrCoO_{3-\delta}$ that favors ORRs over a wide temperature range. The partial substitution of the A-site Sr with Yb is systematically studied, The results indicate that $Sr_{0.90}Yb_{0.10}CoO_{3-\delta}$ is able to stabilize the tetragonal crystal structures with less ordered oxygen vacancies and leads to polarization resistances of 0.051, 0.115 and 0.272 Ω cm^2 at 750, 700 and 650 ^{o}C, respectively. $Sr_{0.90}Yb_{0.10}CoO_{3-\delta}$ demonstrates very stable surface oxygen vacancy distribution and electronic structure near oxygen vacancies but dissociation of adsorbed oxygen molecule into atom oxygen process is affected by surface Sr segregation, and polarization resistance degradation is mainly induced by surface Sr segregation. Furthermore, $Sr_{0.90}Yb_{0.10}CoO_{3-\delta}$ exhibits excellent thermal stability as well as excellent recovery stability and improved polarization performance after a few pure air/CO_2-containing air treatment cycles at 700 ^{o}C. However, a hysteresis behavior of polarization performance is observed at 650 ^{o}C during gas

cycling treatment, which may cause long-term degradation of $Sr_{0.90}Yb_{0.10}CoO_{3-\delta}$ electrode. The different polarization behaviors during gas cycling treatment are induced by different sensitivities of the formed surface strontium carbonate and chemisorbed surface oxo-carbonaceous species to different operating temperatures.

$Sm_xBa_{1-x}Co_{0.8}Fe_{0.2}O_{3-\delta}$ nanocomposites are developed as promising new cathodes for LT-SOFCs. The nanocomposite materials is formed through the thermally induced self-assembled process which could bring uniform distribution and intimate contacts between different phases. Among this series, $Sm_{0.90}Ba_{0.10}Co_{0.8}Fe_{0.2}O_{3-\delta}$ is consisted of a major cubic phase of B-site doped Ba deficient simple perovskite, and a layered perovskite with orthorhombic symmetry. The self-assembled process also induces nanoparticles decorated on the cathode surface. The combination of two ORR-favored lattice structures enables excellent bulk diffusion and surface exchange properties. Compared with other nanocomposites in the series, absence of the hexagonal phase which is less favored towards ORR and the affordable electrical conductivity induced by the layered perovskite promote the kinetic property. When $Sm_{0.90}Ba_{0.10}Co_{0.8}Fe_{0.2}O_{3-\delta}$ is used as the cathode in $Ce_{0.8}Sm_{0.2}O_{1.9}$ (SDC)-based SOFCs, it delivers a peak powder density of 1271 mW cm^{-2} at 650 ^oC with 300 hours stable performance. Therefore, combine the well-tailored components and nanoparticles on the surface in a simple one-step fabrication enables affordable conductivity, excellent ORR kinetic properties as well as excellent stability toward LT-SOFCs.

Introduction of A-site cation deficiency into perovskite oxides is an effective strategy to alter the physical and chemical properties as cathode for LT-SOFCs. We combine the introduction of cation deficiency in the A-site and doping strategy of Zr, Y

in the B-site to form a new series of cathode material $Ba_{1-x}Co_{0.6}Fe_{0.2}Zr_{0.1}Y_{0.1}O_{3-\delta}$ for LT-SOFCs. The creation of A-site cation non-stoichiometry increase the concentration of oxygen vacancy and decrease the average bonding energy, substantially promote catalytic activity for the oxygen reduction reaction. $BaCo_{0.6}Fe_{0.2}Zr_{0.1}Y_{0.1}O_{3-\delta}$ (Ba100CFZY) cathode shows a polarization resistance of 0.090 Ω cm^2 at 600 °C, while the polarization resistance is 0.053 Ω cm^2 for $Ba_{0.95}Co_{0.6}Fe_{0.2}Zr_{0.1}Y_{0.1}O_{3-\delta}$ (B95CFZY), which is just 59% of Ba100CFZY. It is also found that B95CFZY has a lower value of thermal expansion coefficient which make it more thermo-mechanically compatible with electrolyte. The Ba-deficient Ba95CFZY has lower electrical conductivity compared to Ba100CFZY, which could be attributed to additional oxygen vacancies that block the B-O-B bond. However, Ba95CFZY show lower activation energy for electrical conducting. The decreasing A-site Coulomb-potential of Ba95CFZY leads to a more itinerant state of B-O bond hence the decrease of activation energy for electrical conducting. The short-term stability of kinetic property is also enhanced by introducing 5% Ba deficiency, because A-site deficiency can suppress the corresponding Ba segregation. The CO_2 tolerance is also improved as a result of less Ba content by introducing the Ba deficiency. The results justify the potential of Ba95CFZY as cathode material for LT-SOFCs due to its high ORR activity and stability.

The research provides promising progresses in the development of cathode materials for IT-SOFCs and LT-SOFCs. Favorable electrochemical properties are achieved by applying various strategies. Doping cations into A or B site of perovskite can highly affect the crystal structure, oxygen vacancy distribuation, cation-oxygen bond energy, etc., consequently improves electrode performance. The nanocomposites with

different components performed different functionalities show beneficial effect towards ORR. The unique nanoparticles decorated cathode formed in the one-step fabrication process could also increase the number of ORR active sites; thus, an enhanced cathodic performance is expected. The introduction of A-site cation deficiency can also lead to a promising activity by creation additional oxygen vacancies and increasing oxygen mobility. Overall, this dissertation extends the knowledge on the development of active cathode materials for SOFCs operated in intermediate-to-low temperature range.

REFERENCES

[1] E. D. Wachsman and K. T. Lee, "Lowering the temperature of solid oxide fuel cells," *Science,* vol. 334, no. 6058, pp. 935-939, 2011.

[2] O. Z. Sharaf and M. F. Orhan, "An overview of fuel cell technology: Fundamentals and applications," *Renewable and Sustainable Energy Reviews,* vol. 32, pp. 810-853, 2014.

[3] R. O'hayre, S.-W. Cha, W. Colella, and F. B. Prinz, *Fuel cell fundamentals*. John Wiley & Sons, 2016.

[4] B. C. Steele and A. Heinzel, "Materials for fuel-cell technologies," in *Materials For Sustainable Energy: A Collection of Peer-Reviewed Research and Review Articles from Nature Publishing Group*: World Scientific, 2011, pp. 224-231.

[5] Y. Choi, D. S. Mebane, J.-H. Wang, and M. Liu, "Continuum and quantum-chemical modeling of oxygen reduction on the cathode in a solid oxide fuel cell," *Topics in Catalysis,* vol. 46, no. 3-4, pp. 386-401, 2007.

[6] M. Kleitz and F. Petitbon, "Optimized SOFC electrode microstructure," *Solid State Ionics,* vol. 92, no. 1-2, pp. 65-74, 1996.

[7] N. Mahato, A. Banerjee, A. Gupta, S. Omar, and K. Balani, "Progress in material selection for solid oxide fuel cell technology: A review," *Progress in Materials Science,* vol. 72, pp. 141-337, 2015.

[8] Z. Gao, L. V. Mogni, E. C. Miller, J. G. Railsback, and S. A. Barnett, "A perspective on low-temperature solid oxide fuel cells," *Energy & Environmental Science,* vol. 9, no. 5, pp. 1602-1644, 2016.

[9] M. Østergård and M. Mogensen, "ac Impedance study of the oxygen reduction mechanism on La1− xSrxMnO3 in solid oxide fuel cells," *Electrochimica acta,* vol. 38, no. 14, pp. 2015-2020, 1993.

[10] S. P. Jiang, "Development of lanthanum strontium manganite perovskite cathode materials of solid oxide fuel cells: a review," *Journal of Materials Science,* vol. 43, pp. 6799-6833, 2008.

[11] Y. Teraoka, T. Nobunaga, K. Okamoto, N. Miura, and N. Yamazoe, "Influence of constituent metal cations in substituted LaCoO3 on mixed conductivity and oxygen permeability," *Solid State Ionics,* vol. 48, no. 3-4, pp. 207-212, 1991.

[12] A. M. Ritzmann, A. B. Muñoz-García, M. Pavone, J. A. Keith, and E. A. Carter, "Ab Initio DFT+ U Analysis of Oxygen Vacancy Formation and Migration in La1-xSr x FeO3-δ (x= 0, 0.25, 0.50)," *Chemistry of Materials,* vol. 25, no. 15, pp. 3011-3019, 2013.

[13] T. Ishigaki, S. Yamauchi, K. Kishio, J. Mizusaki, and K. Fueki, "Diffusion of oxide ion vacancies in perovskite-type oxides," *Journal of Solid State Chemistry,* vol. 73, no. 1, pp. 179-187, 1988.

[14] A. Egger, E. Bucher, M. Yang, and W. Sitte, "Comparison of oxygen exchange kinetics of the IT-SOFC cathode materials La0. 5Sr0. 5CoO3− δ and La0. 6Sr0. 4CoO3− δ," *Solid State Ionics,* vol. 225, pp. 55-60, 2012.

[15] L. Van der Haar, M. Den Otter, M. Morskate, H. J. Bouwmeester, and H. Verweij, "Chemical Diffusion and Oxygen Surface Transfer of La1− x Sr x CoO3− δ Studied with Electrical Conductivity Relaxation," *Journal of The Electrochemical Society,* vol. 149, no. 3, pp. J41-J46, 2002.

[16] A. Petric, P. Huang, and F. Tietz, "Evaluation of La–Sr–Co–Fe–O perovskites for solid oxide fuel cells and gas separation membranes," *Solid State Ionics,* vol. 135, no. 1-4, pp. 719-725, 2000.

[17] L.-W. Tai, M. Nasrallah, H. Anderson, D. Sparlin, and S. Sehlin, "Structure and electrical properties of La1− xSrxCo1− yFeyO3. Part 1. The system La0. 8Sr0. 2Co1− yFeyO3," *Solid State Ionics,* vol. 76, no. 3-4, pp. 259-271, 1995.

[18] G. C. Kostogloudis and C. Ftikos, "Properties of A-site-deficient La0. 6Sr0. 4Co0. 2Fe0. 8O3− δ-based perovskite oxides," *Solid State Ionics,* vol. 126, no. 1-2, pp. 143-151, 1999.

[19] D. Marinha, L. Dessemond, J. S. Cronin, J. R. Wilson, S. A. Barnett, and E. Djurado, "Microstructural 3D reconstruction and performance evaluation of LSCF cathodes obtained by electrostatic spray deposition," *Chemistry of Materials,* vol. 23, no. 24, pp. 5340-5348, 2011.

[20] R. Merkle, Y. A. Mastrikov, E. A. Kotomin, M. M. Kuklja, and J. Maier, "First principles calculations of oxygen vacancy formation and migration in Ba1− xSrxCo1− yFeyO3− δ Perovskites," *Journal of The Electrochemical Society,* vol. 159, no. 2, p. B219, 2011.

[21] Z. Shao and S. M. Haile, "A high-performance cathode for the next generation of solid-oxide fuel cells," in *Materials for Sustainable Energy: A Collection of Peer-Reviewed Research and Review Articles from Nature Publishing Group*: World Scientific, 2011, pp. 255-258.

[22] D. N. Mueller, R. A. De Souza, T. E. Weirich, D. Roehrens, J. Mayer, and M. Martin, "A kinetic study of the decomposition of the cubic perovskite-type oxide

Ba x Sr 1− x Co 0.8 Fe 0.2 O 3− δ (BSCF)(x= 0.1 and 0.5)," *Physical Chemistry Chemical Physics,* vol. 12, no. 35, pp. 10320-10328, 2010.

[23] S. Švarcová, K. Wiik, J. Tolchard, H. J. Bouwmeester, and T. Grande, "Structural instability of cubic perovskite BaxSr1− xCo1− yFeyO3− δ," *Solid State Ionics,* vol. 178, no. 35-36, pp. 1787-1791, 2008.

[24] H. Fukunaga, M. Koyama, N. Takahashi, C. Wen, and K. Yamada, "Reaction model of dense Sm0. 5Sr0. 5CoO3 as SOFC cathode," *Solid State Ionics,* vol. 132, no. 3-4, pp. 279-285, 2000.

[25] K. Lee and A. Manthiram, "Comparison of Ln0. 6Sr0. 4CoO3− δ (Ln= La, Pr, Nd, Sm, and Gd) as cathode materials for intermediate temperature solid oxide fuel cells," *Journal of the Electrochemical Society,* vol. 153, no. 4, pp. A794-A798, 2006.

[26] S. Y. Istomin *et al.*, "Crystal structure of the novel complex cobalt oxide Sr0. 7Y0. 3CoO2. 62," *Chemistry of materials,* vol. 15, no. 21, pp. 4012-4020, 2003.

[27] T. Ishihara, M. Honda, T. Shibayama, H. Minami, H. Nishiguchi, and Y. Takita, "Intermediate Temperature Solid Oxide Fuel Cells Using a New LaGaO3 Based Oxide Ion Conductor: I. Doped as a New Cathode Material," *Journal of the Electrochemical Society,* vol. 145, no. 9, p. 3177, 1998.

[28] D. Chen, C. Chen, Y. Gao, Z. Zhang, Z. Shao, and F. Ciucci, "Evaluation of pulsed laser deposited SrNb0. 1Co0. 9O3− δ thin films as promising cathodes for intermediate-temperature solid oxide fuel cells," *Journal of Power Sources,* vol. 295, pp. 117-124, 2015.

[29] F. Wang, Q. Zhou, T. He, G. Li, and H. Ding, "Novel SrCo1− yNbyO3− δ cathodes for intermediate-temperature solid oxide fuel cells," *Journal of Power Sources,* vol. 195, no. 12, pp. 3772-3778, 2010.

[30] W. Zhou, J. Sunarso, M. Zhao, F. Liang, T. Klande, and A. Feldhoff, "A highly active perovskite electrode for the oxygen reduction reaction below 600 C," *Angew. Chem. Int. Ed.,* vol. 52, no. 52, pp. 14036-14040, 2013.

[31] Y. Shen, F. Wang, X. Ma, and T. He, "SrCo1− yTiyO3− δ as potential cathode materials for intermediate-temperature solid oxide fuel cells," *Journal of Power Sources,* vol. 196, no. 18, pp. 7420-7425, 2011.

[32] A. Aguadero, J. A. Alonso, D. Pérez-Coll, C. De La Calle, M. a. T. Fernández-Díaz, and J. B. Goodenough, "SrCo0. 95Sb0. 05O3− δ as cathode material for high power density solid oxide fuel cells," *Chemistry of Materials,* vol. 22, no. 3, pp. 789-798, 2010.

[33] A. Aguadero, D. Pérez-Coll, J. Alonso, S. Skinner, and J. Kilner, "A new family of Mo-doped SrCoO3− δ perovskites for application in reversible solid state electrochemical cells," *Chem. Mater.,* vol. 24, no. 14, pp. 2655-2663, 2012.

[34] M. Li, W. Zhou, V. K. Peterson, M. Zhao, and Z. Zhu, "A comparative study of SrCo 0.8 Nb 0.2 O 3− δ and SrCo 0.8 Ta 0.2 O 3− δ as low-temperature solid oxide fuel cell cathodes: effect of non-geometry factors on the oxygen reduction reaction," *Journal of Materials Chemistry A,* vol. 3, no. 47, pp. 24064-24070, 2015.

[35] X. Ding *et al.*, "Cation deficiency enabled fast oxygen reduction reaction for a novel SOFC cathode with promoted CO2 tolerance," *Applied Catalysis B: Environmental,* vol. 243, pp. 546-555, 2019.

[36] A. Taskin, A. Lavrov, and Y. Ando, "Achieving fast oxygen diffusion in perovskites by cation ordering," *Applied Physics Letters,* vol. 86, no. 9, p. 091910, 2005.

[37] A. Tarancón, D. Marrero-López, J. Peña-Martínez, J. Ruiz-Morales, and P. Núñez, "Effect of phase transition on high-temperature electrical properties of GdBaCo2O5+ x layered perovskite," *Solid State Ionics,* vol. 179, no. 17-18, pp. 611-618, 2008.

[38] Y.-C. Chen, M. Yashima, J. Peña-Martínez, and J. A. Kilner, "Experimental visualization of the diffusional pathway of oxide ions in a layered perovskite-type cobaltite PrBaCo2O5+ δ," *Chemistry of Materials,* vol. 25, no. 13, pp. 2638-2641, 2013.

[39] D. Garcés, C. F. Setevich, A. Caneiro, G. J. Cuello, and L. Mogni, "Effect of cationic order–disorder on the transport properties of LaBaCo2O6–δ and La0. 5Ba0. 5CoO3–δ perovskites," *Journal of Applied Crystallography,* vol. 47, no. 1, pp. 325-334, 2014.

[40] Y. Hu *et al.*, "Oxygen diffusion mechanism in the mixed ion-electron conductor NdBaCo 2 O 5+ x," *Journal of Materials Chemistry,* vol. 22, no. 36, pp. 18744-18747, 2012.

[41] K. Zhang, L. Ge, R. Ran, Z. Shao, and S. Liu, "Synthesis, characterization and evaluation of cation-ordered LnBaCo2O5+ δ as materials of oxygen permeation membranes and cathodes of SOFCs," *Acta Materialia,* vol. 56, no. 17, pp. 4876-4889, 2008.

[42] D. Chen, R. Ran, K. Zhang, J. Wang, and Z. Shao, "Intermediate-temperature electrochemical performance of a polycrystalline PrBaCo2O5+ δ cathode on samarium-doped ceria electrolyte," *Journal of Power Sources,* vol. 188, no. 1, pp. 96-105, 2009.

[43] Q. Zhou, T. He, and Y. Ji, "SmBaCo2O5+ x double-perovskite structure cathode material for intermediate-temperature solid-oxide fuel cells," *Journal of Power Sources,* vol. 185, no. 2, pp. 754-758, 2008.

[44] V. Kharton, A. Viskup, E. Naumovich, and F. B. Marques, "Oxygen ion transport in La 2 NiO 4-based ceramics," *Journal of Materials Chemistry,* vol. 9, no. 10, pp. 2623-2629, 1999.

[45] G. Amow and S. Skinner, "Recent developments in Ruddlesden–Popper nickelate systems for solid oxide fuel cell cathodes," *Journal of Solid State Electrochemistry,* vol. 10, no. 8, pp. 538-546, 2006.

[46] J. Xu, H. Thomas, R. W. Francis, K. R. Lum, J. Wang, and B. Liang, "A review of processes and technologies for the recycling of lithium-ion secondary batteries," *Journal of Power Sources,* vol. 177, no. 2, pp. 512-527, 2008.

[47] A. Demourgues *et al.*, "Transport and magnetic properties of La2NiO4+ δ (0≤ δ≤ 0.25)," *Journal of Solid State Chemistry,* vol. 124, no. 2, pp. 199-204, 1996.

[48] K. Ruck, G. Krabbes, and I. Vogel, "Structural and electrical properties of La2− xCaxNiO4+ δ (0≤ x< 0.4) with regard to the oxygen content δ," *Materials research bulletin,* vol. 34, no. 10-11, pp. 1689-1697, 1999.

[49] S. J. Skinner and J. A. Kilner, "Oxygen diffusion and surface exchange in La2− xSrxNiO4+ δ," *Solid State Ionics,* vol. 135, no. 1-4, pp. 709-712, 2000.

[50] A. Aguadero, J. Alonso, M. Escudero, and L. Daza, "Evaluation of the La2Ni1− xCuxO4+ δ system as SOFC cathode material with 8YSZ and LSGM as electrolytes," *Solid State Ionics,* vol. 179, no. 11-12, pp. 393-400, 2008.

[51] J. G. Railsback, Z. Gao, and S. A. Barnett, "Oxygen electrode characteristics of Pr2NiO4+ δ-infiltrated porous (La0. 9Sr0. 1)(Ga0. 8Mg0. 2) O3–δ," *Solid State Ionics,* vol. 274, pp. 134-139, 2015.

[52] X.-D. Zhou, J. W. Templeton, Z. Nie, H. Chen, J. W. Stevenson, and L. R. Pederson, "Electrochemical performance and stability of the cathode for solid oxide fuel cells: V. high performance and stable Pr2NiO4 as the cathode for solid oxide fuel cells," *Electrochimica Acta,* vol. 71, pp. 44-49, 2012.

[53] Z. Shao and S. M. Haile, "A high-performance cathode for the next generation of solid-oxide fuel cells," *Nature,* vol. 431, no. 7005, p. 170, 2004.

[54] W. Zhou, R. Ran, Z. Shao, W. Jin, and N. Xu, "Evaluation of A-site cation-deficient (Ba0. 5Sr0. 5) 1− xCo0. 8Fe0. 2O3− δ (x> 0) perovskite as a solid-oxide fuel cell cathode," *Journal of Power Sources,* vol. 182, no. 1, pp. 24-31, 2008.

[55] D. Marrero-López, R. Romero, F. Martín, and J. Ramos-Barrado, "Effect of the deposition temperature on the electrochemical properties of La0. 6Sr0. 4Co0.

8Fe0. 2O3− δ cathode prepared by conventional spray-pyrolysis," *J. Power Sources,* vol. 255, pp. 308-317, 2014.

[56] M. Yoshiya, C. Fisher, Y. Iwamoto, M. Asanuma, J. Ishii, and K. Yabuta, "Phase stability of BaCo1− yFeyO3− δ by first principles calculations," *Solid State Ionics,* vol. 172, no. 1-4, pp. 159-163, 2004.

[57] A. F. Sammells, R. L. Cook, J. H. White, J. J. Osborne, and R. C. MacDuff, "Rational selection of advanced solid electrolytes for intermediate temperature fuel cells," *Solid State Ionics,* vol. 52, no. 1-3, pp. 111-123, 1992.

[58] F. Dong, D. Chen, Y. Chen, Q. Zhao, and Z. Shao, "La-doped BaFeO 3− δ perovskite as a cobalt-free oxygen reduction electrode for solid oxide fuel cells with oxygen-ion conducting electrolyte," *J. Mater. Chem.,* vol. 22, no. 30, pp. 15071-15079, 2012.

[59] H. Zhao *et al.*, "Investigation of Mixed Conductor BaCo0. 7Fe0. 3− x Y x O3− δ with High Oxygen Permeability," *The Journal of Physical Chemistry C,* vol. 114, no. 41, pp. 17975-17981, 2010.

[60] C. Zhu *et al.*, "Novel BaCo0. 7Fe0. 3− yNbyO3− δ (y= 0–0.12) as a cathode for intermediate temperature solid oxide fuel cell," *Electrochem. Commun.,* vol. 11, no. 5, pp. 958-961, 2009.

[61] P. Shen, X. Liu, H. Wang, and W. Ding, "Niobium Doping Effects on Performance of BaCo0. 7Fe0. 3− x Nb x O3− δ Perovskite," *The Journal of Physical Chemistry C,* vol. 114, no. 50, pp. 22338-22345, 2010.

[62] J. Tong, W. Yang, B. Zhu, and R. Cai, "Investigation of ideal zirconium-doped perovskite-type ceramic membrane materials for oxygen separation," *J. Membr. Sci.,* vol. 203, no. 1-2, pp. 175-189, 2002.

[63] J. Tong, W. Yang, R. Cai, B. Zhu, G. Xiong, and L. Lin, "Investigation on the structure stability and oxygen permeability of titanium-doped perovskite-type oxides of BaTi0. 2CoxFe0. 8− xO3− δ (x= 0.2–0.6)," *Sep. Purif. Technol.,* vol. 32, no. 1-3, pp. 289-299, 2003.

[64] Z. Shao, G. Xiong, J. Tong, H. Dong, and W. Yang, "Ba effect in doped Sr (Co0. 8Fe0. 2) O3-δ on the phase structure and oxygen permeation properties of the dense ceramic membranes," *Sep. Purif. Technol.,* vol. 25, no. 1-3, pp. 419-429, 2001.

[65] C. Setevich, F. Prado, D. de Florio, and A. Caneiro, "Stabilization of the cubic perovskite in the system La1− xBaxCo1− yFeyO3− δ (0.7≤ x≤ 0.9) and its electrochemical performance as cathode materials for intermediate-temperature solid oxide fuel cells," *J. Power Sources,* vol. 247, pp. 264-272, 2014.

[66] W. He, X. Wu, G. Yang, H. Shi, F. Dong, and M. Ni, "BaCo0. 7Fe0. 22Y0. 08O3− δ as an active oxygen reduction electrocatalyst for low-temperature solid oxide fuel cells below 600° C," *ACS Energy Letters,* vol. 2, no. 2, pp. 301-305, 2017.

[67] C. Ren, Y. Gan, C. Yang, M. Lee, G. Dong, and X. Xue, "Fabrication and Characterization of High Performance Intermediate Temperature Alumina Substrate Supported Micro-Tubular SOFCs," *J. Electrochem. Soc.,* vol. 164, no. 7, pp. F722-F731, 2017.

[68] B. H. Toby and R. B. Von Dreele, "GSAS-II: the genesis of a modern open-source all purpose crystallography software package," *J. Appl. Crystallogr.,* vol. 46, no. 2, pp. 544-549, 2013.

[69] Y. Cheng, H. Zhao, D. Teng, F. Li, X. Lu, and W. Ding, "Investigation of Ba fully occupied A-site BaCo0. 7Fe0. 3− xNbxO3− δ perovskite stabilized by low concentration of Nb for oxygen permeation membrane," *J. Membr. Sci.,* vol. 322, no. 2, pp. 484-490, 2008.

[70] B. Qian, Y. Chen, M. O. Tade, and Z. Shao, "BaCo 0.6 Fe 0.3 Sn 0.1 O 3− δ perovskite as a new superior oxygen reduction electrode for intermediate-to-low temperature solid oxide fuel cells," *Journal of Materials Chemistry A,* vol. 2, no. 36, pp. 15078-15086, 2014.

[71] Z. Yang, C. Yang, B. Xiong, M. Han, and F. Chen, "BaCo0. 7Fe0. 2Nb0. 1O3− δ as cathode material for intermediate temperature solid oxide fuel cells," *J. Power Sources,* vol. 196, no. 22, pp. 9164-9168, 2011.

[72] A. Leonide, V. Sonn, A. Weber, and E. Ivers-Tiffée, "Evaluation and modeling of the cell resistance in anode-supported solid oxide fuel cells," *J. Electrochem. Soc.,* vol. 155, no. 1, pp. B36-B41, 2008.

[73] T. H. Wan, M. Saccoccio, C. Chen, and F. Ciucci, "Influence of the discretization methods on the distribution of relaxation times deconvolution: implementing radial basis functions with DRTtools," *Electrochim. Acta,* vol. 184, pp. 483-499, 2015.

[74] Y. Takeda, R. Kanno, M. Noda, Y. Tomida, and O. Yamamoto, "Cathodic polarization phenomena of perovskite oxide electrodes with stabilized zirconia," *J. Electrochem. Soc.,* vol. 134, no. 11, pp. 2656-2661, 1987.

[75] M. Escudero, A. Aguadero, J. Alonso, and L. Daza, "A kinetic study of oxygen reduction reaction on La2NiO4 cathodes by means of impedance spectroscopy," *J. Electroanal. Chem.,* vol. 611, no. 1-2, pp. 107-116, 2007.

[76] Z. Yang, C. Yang, C. Jin, M. Han, and F. Chen, "Ba0. 9Co0. 7Fe0. 2Nb0. 1O3− δ as cathode material for intermediate temperature solid oxide fuel cells," *Electrochem. Commun.,* vol. 13, no. 8, pp. 882-885, 2011.

[77] A. T. Duong and D. R. Mumm, "On the interaction of SSC and LSGM in composite SOFC electrodes," *J. Power Sources,* vol. 241, pp. 281-287, 2013.

[78] B. Philippeau, F. Mauvy, C. Mazataud, S. Fourcade, and J.-C. Grenier, "Comparative study of electrochemical properties of mixed conducting Ln2NiO4+ δ (Ln= La, Pr and Nd) and La0. 6Sr0. 4Fe0. 8Co0. 2O3− δ as SOFC cathodes associated to Ce0. 9Gd0. 1O2− δ, La0. 8Sr0. 2Ga0. 8Mg0. 2O3− δ and La9Sr1Si6O26. 5 electrolytes," *Solid State Ionics,* vol. 249, pp. 17-25, 2013.

[79] J. Zou, J. Park, B. Kwak, H. Yoon, and J. Chung, "Effect of Fe doping on PrBaCo2O5+ δ as cathode for intermediate-temperature solid oxide fuel cells," *Solid State Ionics,* vol. 206, pp. 112-119, 2012.

[80] J. H. Kim, Y. Kim, P. A. Connor, J. T. Irvine, J. Bae, and W. Zhou, "Structural, thermal and electrochemical properties of layered perovskite SmBaCo2O5+ d, a potential cathode material for intermediate-temperature solid oxide fuel cells," *J. Power Sources,* vol. 194, no. 2, pp. 704-711, 2009.

[81] D. J. Brett, A. Atkinson, N. P. Brandon, and S. J. Skinner, "Intermediate temperature solid oxide fuel cells," *Chem. Soc. Rev.,* vol. 37, no. 8, pp. 1568-1578, 2008.

[82] N. Q. Minh, "Ceramic fuel cells," *Journal of the American Ceramic Society,* vol. 76, no. 3, pp. 563-588, 1993.

[83] T. Komatsu, R. Chiba, H. Arai, and K. Sato, "Chemical compatibility and electrochemical property of intermediate-temperature SOFC cathodes under Cr poisoning condition," *J. Power Sources,* vol. 176, no. 1, pp. 132-137, 2008.

[84] J. Richter, P. Holtappels, T. Graule, T. Nakamura, and L. J. Gauckler, "Materials design for perovskite SOFC cathodes," *Monatshefte für Chemie-Chemical Monthly,* vol. 140, no. 9, pp. 985-999, 2009.

[85] D. Chen, C. Chen, Z. Zhang, Z. M. Baiyee, F. Ciucci, and Z. Shao, "Compositional engineering of perovskite oxides for highly efficient oxygen reduction reactions," *ACS Appl. Mater. Interfaces,* vol. 7, no. 16, pp. 8562-8571, 2015.

[86] C. De la Calle, A. Aguadero, J. Alonso, and M. Fernández-Díaz, "Correlation between reconstructive phase transitions and transport properties from SrCoO2. 5 brownmillerite: A neutron diffraction study," *Solid State Sci.,* vol. 10, no. 12, pp. 1924-1935, 2008.

[87] H. Kruidhof, H. J. Bouwmeester, R. v. Doorn, and A. Burggraaf, "Influence of order-disorder transitions on oxygen permeability through selected nonstoichiometric perovskite-type oxides," *Solid State Ionics,* vol. 63, pp. 816-822, 1993.

[88] W. Zhou, Z. Shao, R. Ran, and R. Cai, "Novel SrSc0. 2Co0. 8O3− δ as a cathode material for low temperature solid-oxide fuel cell," *Electrochem. Commun.,* vol. 10, no. 10, pp. 1647-1651, 2008.

[89] R. D. Shannon, "Revised effective ionic radii and systematic studies of interatomic distances in halides and chalcogenides," *Acta Crystallogr. A,* vol. 32, no. 5, pp. 751-767, 1976.

[90] A. Aguadero, J. A. Alonso, D. Pérez-Coll, C. de la Calle, M. a. T. Fernández-Díaz, and J. B. Goodenough, "SrCo0. 95Sb0. 05O3− δ as cathode material for high power density solid oxide fuel cells," *Chem. Mater.,* vol. 22, no. 3, pp. 789-798, 2009.

[91] G. López-Pacheco, R. López-Juárez, M. E. Villafuerte-Castrejón, C. Falcony, E. Barrera-Calva, and F. González, "Luminescence properties of Yb 3+-doped SrTiO 3: the significance of the oxygen–titanium charge transfer state on photon downshifting," *Dalton Trans.,* vol. 48, no. 31, pp. 11889-11896, 2019.

[92] Y. Wang, L. Li, J. Qi, and Z. Gui, "Ferroelectric characteristics of ytterbium-doped barium zirconium titanate ceramics," *Ceram. Int.,* vol. 28, no. 6, pp. 657-661, 2002.

[93] S. W. Park, B. K. Moon, S. H. Park, J. H. Jeong, H. Choi, and J. H. Kim, "The role of Yb 3+ concentrations on Er 3+ doped SrLaMgTaO 6 double perovskite phosphors," *RSC Advances,* vol. 7, no. 3, pp. 1464-1470, 2017.

[94] G. M. Rupp, A. K. Opitz, A. Nenning, A. Limbeck, and J. Fleig, "Real-time impedance monitoring of oxygen reduction during surface modification of thin film cathodes," *Nat. Mater.,* vol. 16, no. 6, p. 640, 2017.

[95] Y. Li *et al.*, "Controlling cation segregation in perovskite-based electrodes for high electro-catalytic activity and durability," *Chemical Society Reviews,* vol. 46, no. 20, pp. 6345-6378, 2017.

[96] H. Yokokawa, H. Tu, B. Iwanschitz, and A. Mai, "Fundamental mechanisms limiting solid oxide fuel cell durability," *J. Power Sources,* vol. 182, no. 2, pp. 400-412, 2008.

[97] M. Arnold, H. Wang, and A. Feldhoff, "Influence of CO2 on the oxygen permeation performance and the microstructure of perovskite-type (Ba0. 5Sr0. 5)(Co0. 8Fe0. 2) O3− δ membranes," *J. Membr. Sci.,* vol. 293, no. 1-2, pp. 44-52, 2007.

[98] Y. Zhang, G. Yang, G. Chen, R. Ran, W. Zhou, and Z. Shao, "Evaluation of the CO2 poisoning effect on a highly active cathode SrSc0. 175Nb0. 025Co0. 8O3-δ in the oxygen reduction reaction," *ACS applied materials & interfaces,* vol. 8, no. 5, pp. 3003-3011, 2016.

[99] W. Gordy and W. O. Thomas, "Electronegativities of the elements," *J. Chem. Phys.,* vol. 24, no. 2, pp. 439-444, 1956.

[100] R. Le Toquin, W. Paulus, A. Cousson, C. Prestipino, and C. Lamberti, "Time-resolved in situ studies of oxygen intercalation into SrCoO2. 5, performed by neutron diffraction and X-ray absorption spectroscopy," *J. Am. Chem. Soc.,* vol. 128, no. 40, pp. 13161-13174, 2006.

[101] Y. Ito, R. F. Klie, N. D. Browning, and T. J. Mazanec, "Atomic resolution analysis of the defect chemistry and microdomain structure of brownmillerite-type strontium cobaltite," *J. Am. Ceram. Soc.,* vol. 85, no. 4, pp. 969-976, 2002.

[102] R. E. Usiskin, T. C. Davenport, R. Y. Wang, W. Guan, and S. M. Haile, "Bulk properties of the oxygen reduction catalyst SrCo0. 9Nb0. 1O3− δ," *Chem. Mater.,* vol. 28, no. 8, pp. 2599-2608, 2016.

[103] W. T. Harrison, S. L. Hegwood, and A. J. Jacobson, "A powder neutron diffraction determination of the structure of Sr 6 Co 5 O 15, formerly described as the low-temperature hexagonal form of SrCoO 3–x," *J. Chem. Soc., Chem. Commun.,* no. 19, pp. 1953-1954, 1995.

[104] T. Nagai, W. Ito, and T. Sakon, "Relationship between cation substitution and stability of perovskite structure in SrCoO3–δ-based mixed conductors," *Solid State Ionics,* vol. 177, no. 39-40, pp. 3433-3444, 2007.

[105] M. James, D. Cassidy, D. Goossens, and R. Withers, "The phase diagram and tetragonal superstructures of the rare earth cobaltate phases Ln1− xSrxCoO3–δ (Ln= La3+, Pr3+, Nd3+, Sm3+, Gd3+, Y3+, Ho3+, Dy3+, Er3+, Tm3+ and Yb3+)," *J. Solid State Chem.,* vol. 177, no. 6, pp. 1886-1895, 2004.

[106] Y. Li *et al.*, "Oxygen-deficient perovskite Sr0. 7Y0. 3CoO2. 65− δ as a cathode for intermediate-temperature solid oxide fuel cells," *Chem. Mater.,* vol. 23, no. 22, pp. 5037-5044, 2011.

[107] L. Zhao, J. Drennan, C. Kong, and S. Amarasinghe, "Insight into surface segregation and chromium deposition on La 0.6 Sr 0.4 Co 0.2 Fe 0.8 O 3− δ cathodes of solid oxide fuel cells," *J. Mater. Chem. A,* vol. 2, no. 29, pp. 11114-11123, 2014.

[108] F. S. Baumann, J. Fleig, M. Konuma, U. Starke, H.-U. Habermeier, and J. Maier, "Strong performance improvement of La0. 6Sr0. 4Co0. 8Fe0. 2O3− δ SOFC cathodes by electrochemical activation," *J. Electrochem. Soc.,* vol. 152, no. 10, pp. A2074-A2079, 2005.

[109] M. Liu, D. Ding, K. Blinn, X. Li, L. Nie, and M. Liu, "Enhanced performance of LSCF cathode through surface modification," *Int. J. Hydrogen Energy,* vol. 37, no. 10, pp. 8613-8620, 2012.

[110] B. Koo, K. Kim, J. K. Kim, H. Kwon, J. W. Han, and W. Jung, "Sr segregation in perovskite oxides: why it happens and how it exists," *Joule,* vol. 2, no. 8, pp. 1476-1499, 2018.

[111] S. Chen *et al.*, "Highly Selective Carbon Dioxide Electroreduction on Structure-evolved Copper Perovskite Oxide toward Methane Production," *ACS Catal.,* vol. 10, no. 8, pp. 4640-4646, 2020.

[112] H. Zhang and W. Yang, "Highly efficient electrocatalysts for oxygen reduction reaction," *Chem. Commun. (Cambridge, U. K.),* no. 41, pp. 4215-4217, 2007.

[113] D. Chen, C. Huang, R. Ran, H. J. Park, C. Kwak, and Z. Shao, "New Ba0. 5Sr0. 5Co0. 8Fe0. 2O3− δ+ Co3O4 composite electrode for IT-SOFCs with improved electrical conductivity and catalytic activity," *Electrochem. Commun.,* vol. 13, no. 2, pp. 197-199, 2011.

[114] H. Ding, A. V. Virkar, M. Liu, and F. Liu, "Suppression of Sr surface segregation in La 1− x Sr x Co 1− y Fe y O 3− δ: a first principles study," *Phys. Chem. Chem. Phys.,* vol. 15, no. 2, pp. 489-496, 2013.

[115] J. Druce *et al.*, "Surface termination and subsurface restructuring of perovskite-based solid oxide electrode materials," *Energy Environ. Sci.,* vol. 7, no. 11, pp. 3593-3599, 2014.

[116] E. J. Crumlin *et al.*, "Surface strontium enrichment on highly active perovskites for oxygen electrocatalysis in solid oxide fuel cells," *Energy Environ. Sci.,* vol. 5, no. 3, pp. 6081-6088, 2012.

[117] E. Mutoro, E. J. Crumlin, M. D. Biegalski, H. M. Christen, and Y. Shao-Horn, "Enhanced oxygen reduction activity on surface-decorated perovskite thin films for solid oxide fuel cells," *Energy Environ. Sci.,* vol. 4, no. 9, pp. 3689-3696, 2011.

[118] Y.-L. Huang, C. Pellegrinelli, M. Sakbodin, and E. D. Wachsman, "Molecular Reactions of O2 and CO2 on Ionically Conducting Catalyst," *ACS Catal.,* vol. 8, no. 2, pp. 1231-1237, 2018.

[119] J. Hwang *et al.*, "CO2 Reactivity on Cobalt-Based Perovskites," *The Journal of Physical Chemistry C,* vol. 122, no. 35, pp. 20391-20401, 2018.

[120] J. M. Tascón and L. G. Tejuca, "Adsorption of CO 2 on the perovskite-type oxide LaCoO 3," *J. Chem. Soc. Faraday Trans. 1 Phys. Chem. Condens. Phases,* vol. 77, no. 3, pp. 591-602, 1981.

[121] K. Efimov, T. Klande, N. Juditzki, and A. Feldhoff, "Ca-containing CO2-tolerant perovskite materials for oxygen separation," *J. Membr. Sci.,* vol. 389, pp. 205-215, 2012.

[122] A. Yan *et al.*, "Investigation of a Ba0. 5Sr0. 5Co0. 8Fe0. 2O3− δ based cathode IT-SOFC: I. The effect of CO2 on the cell performance," *Applied Catalysis B: Environmental,* vol. 66, no. 1-2, pp. 64-71, 2006.

[123] Y. Zhu, J. Sunarso, W. Zhou, and Z. Shao, "Probing CO2 reaction mechanisms and effects on the SrNb0. 1Co0. 9− xFexO3− δ cathodes for solid oxide fuel cells," *Appl. Catal. B,* vol. 172, pp. 52-57, 2015.

[124] K. Nomura, Y. Ujihira, T. Hayakawa, and K. Takehira, "CO2 absorption properties and characterization of perovskite oxides,(Ba, Ca)(Co, Fe) O3− δ," *Appl. Catal. A,* vol. 137, no. 1, pp. 25-36, 1996.

[125] C. Graves, S. D. Ebbesen, S. H. Jensen, S. B. Simonsen, and M. B. Mogensen, "Eliminating degradation in solid oxide electrochemical cells by reversible operation," *Nature materials,* vol. 14, no. 2, pp. 239-244, 2015.

[126] Y. Zhang *et al.*, "Recent progress on advanced materials for solid-oxide fuel cells operating below 500° C," *Advanced Materials,* vol. 29, no. 48, p. 1700132, 2017.

[127] S. S. Shin *et al.*, "Multiscale structured low-temperature solid oxide fuel cells with 13 W power at 500° C," *Energy & Environmental Science,* 2020.

[128] Y.-L. Huang, A. M. Hussain, I. A. Robinson, and E. D. Wachsman, "Nanointegrated, high-performing cobalt-free bismuth-based composite cathode for low-temperature solid oxide fuel cells," *ACS applied materials & interfaces,* vol. 10, no. 34, pp. 28635-28643, 2018.

[129] B. Niu *et al.*, "In-situ growth of nanoparticles-decorated double perovskite electrode materials for symmetrical solid oxide cells," *Applied Catalysis B: Environmental,* p. 118842, 2020.

[130] J. Vieten *et al.*, "Materials design of perovskite solid solutions for thermochemical applications," *Energy & Environmental Science,* vol. 12, no. 4, pp. 1369-1384, 2019.

[131] C. M. Chanquia, L. Mogni, H. E. Troiani, and A. Caneiro, "Highly active La0. 4Sr0. 6Co0. 8Fe0. 2O3− δ nanocatalyst for oxygen reduction in intermediate temperature-solid oxide fuel cells," *Journal of Power Sources,* vol. 270, pp. 457-467, 2014.

[132] Y. Zhu, Z. G. Chen, W. Zhou, S. Jiang, J. Zou, and Z. Shao, "An A-site-deficient perovskite offers high activity and stability for low-temperature solid-oxide fuel cells," *ChemSusChem,* vol. 6, no. 12, pp. 2249-2254, 2013.

[133] S.-e. Hou, J. A. Alonso, and J. B. Goodenough, "Co-free, iron perovskites as cathode materials for intermediate-temperature solid oxide fuel cells," *Journal of Power Sources,* vol. 195, no. 1, pp. 280-284, 2010.

[134] L. Zhao, B. He, X. Zhang, R. Peng, G. Meng, and X. Liu, "Electrochemical performance of novel cobalt-free oxide Ba0. 5Sr0. 5Fe0. 8Cu0. 2O3− δ for solid oxide fuel cell cathode," *Journal of Power Sources,* vol. 195, no. 7, pp. 1859-1861, 2010.

[135] S. Jiang, W. Zhou, Y. Niu, Z. Zhu, and Z. Shao, "Phase Transition of a Cobalt-Free Perovskite as a High-Performance Cathode for Intermediate-Temperature Solid Oxide Fuel Cells," *ChemSusChem,* vol. 5, no. 10, pp. 2023-2031, 2012.

[136] Y. Song *et al.*, "A Cobalt-Free Multi-Phase Nanocomposite as Near-Ideal Cathode of Intermediate-Temperature Solid Oxide Fuel Cells Developed by Smart Self-Assembly," *Advanced Materials,* vol. 32, no. 8, p. 1906979, 2020.

[137] A. S. Painter, Y.-L. Huang, and E. D. Wachsman, "Durability of (La0. 8Sr0. 2) 0.95 MnO3-δ-(Er0. 2Bi0. 8) 2O3 composite cathodes for low temperature SOFCs," *Journal of Power Sources,* vol. 360, pp. 391-398, 2017.

[138] Y. Song *et al.*, "Self-assembled triple-conducting nanocomposite as a superior protonic ceramic fuel cell cathode," *Joule,* vol. 3, no. 11, pp. 2842-2853, 2019.

[139] D. Ding *et al.*, "Efficient electro-catalysts for enhancing surface activity and stability of SOFC cathodes," *Advanced Energy Materials,* vol. 3, no. 9, pp. 1149-1154, 2013.

[140] X. Zhang *et al.*, "Enhanced oxygen reduction activity and solid oxide fuel cell performance with a nanoparticles-loaded cathode," *Nano letters,* vol. 15, no. 3, pp. 1703-1709, 2015.

[141] Y. Zhu, W. Zhou, R. Ran, Y. Chen, Z. Shao, and M. Liu, "Promotion of oxygen reduction by exsolved silver nanoparticles on a perovskite scaffold for low-temperature solid oxide fuel cells," *Nano letters,* vol. 16, no. 1, pp. 512-518, 2016.

[142] K. Sasaki, J. Tamura, H. Hosoda, T. Lan, K. Yasumoto, and M. Dokiya, "Pt–perovskite cermet cathode for reduced-temperature SOFCs," *Solid state ionics,* vol. 148, no. 3-4, pp. 551-555, 2002.

[143] D. Ding, X. Li, S. Y. Lai, K. Gerdes, and M. Liu, "Enhancing SOFC cathode performance by surface modification through infiltration," *Energy & Environmental Science,* vol. 7, no. 2, pp. 552-575, 2014.

[144] X. Lou, S. Wang, Z. Liu, L. Yang, and M. Liu, "Improving La0. 6Sr0. 4Co0. 2Fe0. 8O3− δ cathode performance by infiltration of a Sm0. 5Sr0. 5CoO3− δ coating," *Solid State Ionics,* vol. 180, no. 23-25, pp. 1285-1289, 2009.

[145] G. Yang *et al.*, "Toward Reducing the Operation Temperature of Solid Oxide Fuel Cells: Our Past 15 Years of Efforts in Cathode Development," *Energy & Fuels,* 2020.

[146] F. Wang, D. Chen, and Z. Shao, "Composition and microstructure optimization and operation stability of barium deficient Ba1− xCo0. 7Fe0. 2Nb0. 1O3− δ perovskite oxide electrodes," *Electrochimica Acta,* vol. 103, pp. 23-31, 2013.

[147] X. Kuai *et al.*, "Boosting the Activity of BaCo0. 4Fe0. 4Zr0. 1Y0. 1O3− δ Perovskite for Oxygen Reduction Reactions at Low-to-Intermediate Temperatures through Tuning B-Site Cation Deficiency," *Advanced Energy Materials,* vol. 9, no. 38, p. 1902384, 2019.

[148] J.-H. Kim and A. Manthiram, "LnBaCo2O5+ δ oxides as cathodes for intermediate-temperature solid oxide fuel cells," *Journal of the Electrochemical Society,* vol. 155, no. 4, p. B385, 2008.

[149] A. Jun, J. Kim, J. Shin, and G. Kim, "Optimization of Sr content in layered SmBa1−xSrxCo2O5+ δ perovskite cathodes for intermediate-temperature solid oxide fuel cells," *International journal of hydrogen energy,* vol. 37, no. 23, pp. 18381-18388, 2012.

[150] F. Ciucci, "Electrical conductivity relaxation measurements: Statistical investigations using sensitivity analysis, optimal experimental design and ECRTOOLS," *Solid State Ionics,* vol. 239, pp. 28-40, 2013.

[151] B. Hua, M. Li, Y. F. Sun, J. H. Li, and J. L. Luo, "Enhancing perovskite electrocatalysis of solid oxide cells through controlled exsolution of nanoparticles," *ChemSusChem,* vol. 10, no. 17, pp. 3333-3341, 2017.

[152] F. Lu, T. Xia, Q. Li, J. Wang, L. Huo, and H. Zhao, "Heterostructured simple perovskite nanorod-decorated double perovskite cathode for solid oxide fuel cells: Highly catalytic activity, stability and CO2-durability for oxygen reduction reaction," *Applied Catalysis B: Environmental,* vol. 249, pp. 19-31, 2019.

[153] D. Chen and Z. Shao, "Surface exchange and bulk diffusion properties of Ba0. 5Sr0. 5Co0. 8Fe0. 2O3− δ mixed conductor," *international journal of hydrogen energy,* vol. 36, no. 11, pp. 6948-6956, 2011.

[154] M. Escudero, A. Aguadero, J. A. Alonso, and L. Daza, "A kinetic study of oxygen reduction reaction on La2NiO4 cathodes by means of impedance spectroscopy," *Journal of Electroanalytical Chemistry,* vol. 611, no. 1-2, pp. 107-116, 2007.

[155] S. Park, J. M. Vohs, and R. J. Gorte, "Direct oxidation of hydrocarbons in a solid-oxide fuel cell," *Nature,* vol. 404, no. 6775, pp. 265-267, 2000.

[156] A. J. Jacobson, "Materials for solid oxide fuel cells," *Chemistry of Materials,* vol. 22, no. 3, pp. 660-674, 2010.

[157] S. B. Adler, "Factors governing oxygen reduction in solid oxide fuel cell cathodes," *Chemical reviews,* vol. 104, no. 10, pp. 4791-4844, 2004.

[158] Y. Chen *et al.*, "Advances in cathode materials for solid oxide fuel cells: complex oxides without alkaline earth metal elements," *Advanced Energy Materials,* vol. 5, no. 18, p. 1500537, 2015.

[159] C. Duan, D. Hook, Y. Chen, J. Tong, and R. O'Hayre, "Zr and Y co-doped perovskite as a stable, high performance cathode for solid oxide fuel cells operating below 500 C," *Energy & Environmental Science,* vol. 10, no. 1, pp. 176-182, 2017.

[160] Y. Li *et al.*, "Systematic investigation on structure stability and oxygen permeability of Sr-doped BaCo0. 7Fe0. 2Nb0. 1O3− δ ceramic membranes," *Journal of Membrane Science,* vol. 362, no. 1-2, pp. 460-470, 2010.

[161] T. Striker, J. Ruud, Y. Gao, W. Heward, and C. Steinbruchel, "A-site deficiency, phase purity and crystal structure in lanthanum strontium ferrite powders," *Solid State Ionics,* vol. 178, no. 21-22, pp. 1326-1336, 2007.

[162] J. Sunarso, S. S. Hashim, N. Zhu, and W. Zhou, "Perovskite oxides applications in high temperature oxygen separation, solid oxide fuel cell and membrane reactor: A review," *Progress in Energy and Combustion Science,* vol. 61, pp. 57-77, 2017.

[163] S. Pang, X. Jiang, X. Li, Q. Wang, and Z. Su, "Characterization of Ba-deficient PrBa1− xCo2O5+ δ as cathode material for intermediate temperature solid oxide fuel cells," *Journal of power sources,* vol. 204, pp. 53-59, 2012.

[164] A. Donazzi *et al.*, "Evaluation of Ba deficient NdBaCo2O5+ δ oxide as cathode material for IT-SOFC," *Electrochimica acta,* vol. 182, pp. 573-587, 2015.

[165] W. Lee, J. W. Han, Y. Chen, Z. Cai, and B. Yildiz, "Cation size mismatch and charge interactions drive dopant segregation at the surfaces of manganite perovskites," *Journal of the American Chemical Society,* vol. 135, no. 21, pp. 7909-7925, 2013.

[166] J. Zhang, M. Gao, and J.-L. Luo, "In–situ Exsolved Metal Nanoparticles: A Smart Approach for Optimization of Catalysts," *Chemistry of Materials,* 2020.

[167] A. Mineshige *et al.*, "Introduction of A-site deficiency into La0. 6Sr0. 4Co0. 2Fe0. 8O3–δ and its effect on structure and conductivity," *Solid State Ionics,* vol. 176, no. 11-12, pp. 1145-1149, 2005.

[168] E. Y. Konysheva, X. Xu, and J. T. Irvine, "On the existence of A-site deficiency in perovskites and its relation to the electrochemical performance," *Advanced Materials,* vol. 24, no. 4, pp. 528-532, 2012.

[169] M. Mori and N. M. Sammes, "Sintering and thermal expansion characterization of Al-doped and Co-doped lanthanum strontium chromites synthesized by the Pechini method," *Solid state ionics,* vol. 146, no. 3-4, pp. 301-312, 2002.

[170] H. Ullmann, N. Trofimenko, F. Tietz, D. Stöver, and A. Ahmad-Khanlou, "Correlation between thermal expansion and oxide ion transport in mixed conducting perovskite-type oxides for SOFC cathodes," *Solid state ionics,* vol. 138, no. 1-2, pp. 79-90, 2000.

[171] K. Zhang, R. Ran, L. Ge, Z. Shao, W. Jin, and N. Xu, "Systematic investigation on new SrCo1− yNbyO3− δ ceramic membranes with high oxygen semi-permeability," *Journal of Membrane Science,* vol. 323, no. 2, pp. 436-443, 2008.

[172] J. Stevenson, T. Armstrong, R. Carneim, L. Pederson, and W. Weber, "Electrochemical properties of mixed conducting perovskites la1− x m x co1− y fe y o 3− δ (m= sr, ba, ca)," *Journal of the Electrochemical Society,* vol. 143, no. 9, p. 2722, 1996.

[173] V. M. Goldschmidt, "Die gesetze der krystallochemie," *Naturwissenschaften,* vol. 14, no. 21, pp. 477-485, 1926.

[174] R. Voorhoeve, J. Remeika, and L. Trimble, "Defect chemistry and catalysis in oxidation and reduction over perovskite-type oxides," *Annals of the New York Academy of Sciences,* vol. 272, no. 1, pp. 3-21, 1976.

[175] H. Téllez, J. Druce, J. A. Kilner, and T. Ishihara, "Relating surface chemistry and oxygen surface exchange in LnBaCo2O5+ δ air electrodes," *Faraday discussions,* vol. 182, pp. 145-157, 2015.

[176] D. Garcés *et al.*, "An insight into the electrochemical performance of La 0.5− x Pr x Ba 0.5 CoO 3− δ as cathodes for solid oxide fuel cells: study of the O 2-reduction reaction," *Journal of Materials Chemistry A,* vol. 6, no. 34, pp. 16699-16709, 2018.

[177] D. Neagu, G. Tsekouras, D. N. Miller, H. Ménard, and J. T. Irvine, "In situ growth of nanoparticles through control of non-stoichiometry," *Nature chemistry,* vol. 5, no. 11, pp. 916-923, 2013.

[178] G. Tsekouras, D. Neagu, and J. T. Irvine, "Step-change in high temperature steam electrolysis performance of perovskite oxide cathodes with exsolution of B-site dopants," *Energy & Environmental Science,* vol. 6, no. 1, pp. 256-266, 2013.

[179] J. Yi, M. Schroeder, T. Weirich, and J. Mayer, "Behavior of Ba (Co, Fe, Nb) O3-δ perovskite in CO2-containing atmospheres: degradation mechanism and materials design," *Chemistry of Materials,* vol. 22, no. 23, pp. 6246-6253, 2010.

[180] Z. Yang, Y. Liu, T. Zhu, Y. Chen, M. Han, and C. Jin, "Mechanism analysis of CO2 corrosion on Ba0. 9Co0. 7Fe0. 2Nb0. 1O3− δ cathode," *International Journal of Hydrogen Energy,* vol. 41, no. 3, pp. 1997-2001, 2016.